N73-18847

NASA TECHNICAL TRANSLATION

NASA TT F-729

NASA TT F-729

CASE FILE COPY

RADAR STUDIES OF THE MOON

by N. N. Krupenio

"Nauka" Press, Moscow, 1971

NATIONAL AERONAUTICS AND SPACE ADMINISTRATION • WASHINGTON, D. C. • FEBRUARY 1973

ANNOTATION

Radar methods of investigating the moon and planets by ground radar and radio equipment installed in space vehicles are reviewed. The terminology of the characteristics of reradiation from the surface layer of the moon and planets in the radio spectrum, the interconnection between them, the principal characteristics of reradiation necessary to calculate the energy parameters for the radio-frequency circuits for different locations of transmitter, illuminated surface, and receiver, and the results of radar observations of the moon from the earth, and from space vehicles, over a broad band of radio waves, are cited.

The book is written for specialists working in the fields of radioastronomy, radar astronomy, and lunar and planetary research. It will be of interest to students enrolled in the senior courses offered by the physics and radio engineering departments of higher institutions of learning, as well as to specialists engaged in the development and use of radar techniques for near-space application.

TABLE OF CONTENTS /3

Introduction 1

Chapter I.

A Short Survey of Data on the Moon, and on its Surface and Surface Layer, Obtained from Measurements Made from the Earth and from Space Vehicles 6

1. Motion, Dimensions, Mass, Density 6
2. Surface Macrorelief 7
3. Surface Microstructure 11
4. Physical and Chemical Characteristics of the Lunar Surface Layer 12
5. Thermal Properties of the Surface Layer of the Near Side of the Moon 14
6. Properties of the Surface Layer of the Near Side of the Moon in the Optical, Infrared, and Ultraviolet Regions 16
7. Electromagnetic Properties of the Lunar Surface Layer Material 20

Chapter II

Surface Layer Reflection and Scattering Characteristics . 24

1. Reflection and Scattering Characteristics, Terminology 24
2. Types of Reradiating Surface Layers 27
3. Energy Characteristics of Radio Links Using the Surface of a Planet as One of Their Elements 47
4. Interrelationship of Reradiation Characteristics . . . 55

Chapter III

Methods for Determining Reradiation Characteristics . . . 60

1. Comparative Evaluation of the Use of Radio Methods to Locate the Moon and the Planets from the Earth and from Spacecraft 60
2. The Use of Pulse Modulated Radar from the Earth . . . 63
3. Radar Detection from the Earth Using a Continuous Monochromatic Signal 72
4. Radar Detection from the Earth Using Pulse Modulation and Doppler Frequency Spectrum Analysis 77

5. Investigation of the Characteristics of Reradiation from the Surface with a Radio Altimeter or Radar Installed in a Spacecraft near the Lunar Surface . . 87

6. Radar Detection Using a System with a Synthesized Antenna Installed on a Spacecraft near the Lunar Surface 93

7. Pulse Modulation of the On-Board Transmitter of a Spacecraft near the Lunar Surface Receiving a Signal from the Earth 97

8. Monochromatic Radiation from the On-Board Transmitter of a Spacecraft near the Lunar Surface with Signal Reception on the Earth 102

Chapter IV

Results of Radar Investigations of the Characteristics of Reradiation from the Moon Using Ground Radars and Space Vehicles 108

1. Results of the Measurement of the Radar Cross Section of the Visible Part of the Lunar Surface from Ground Investigations 108

2. Results of Determining Backscattering Patterns for the Visible Part of the Lunar Surface from Ground Measurements 112

3. Results of the Determination of the Reflectivity for the Normal Incidence Case from Data from Ground Radar Measurements 116

4. Ground Polarization Measurements of an Echo from the Moon 118

5. Measurement of Reflectivity During the Landing of Luna 9 and Luna 13 on the Lunar Surface 121

6. Measurement of the Reflectivity of the Lunar Surface during the Landing of Surveyor 1, Surveyor 3, Surveyor 5, Surveyor 6, and Surveyor 7 128

7. Measurement of Integrated Reradiation Coefficient by Luna 11 and Luna 12 134

8. Measurement of Characteristics of Reradiation by Lunar Orbiter 1 and Explorer 35 137

9. Measurement of Characteristics of Reradiation by Luna 14 143

Chapter V

Interpretation of the Results of Radar Investigation of the Moon to Determine the Physical Characteristics of Its Surface Layer 147

1. Coefficient of Reflection for the Moon in the RF Band . . 147

2. Permittivity and Density of the Material Comprising the Moon's Upper Cover 160

3. Surface Slopes 164

4. Comparison of Results of Determining the Physical Characteristics of a Surface and a Surface Layer by Radar and Other Methods 172

Chapter VI

The Future of Radar Investigations of the Moon 182

Appendices 186

References 188

Introduction

Until recently, all investigations of near space, the moon, the planets in the solar system, and other celestial bodies, were made from the earth. The vast distances to these bodies, as well as the ionosphere and the earth's atmosphere, significantly limited the potentials for such investigations. Moreover, technical improvements in equipment did not always improve measurement results. Lunar surface resolution, for example, has the same value now, using the largest telescope at Mount Palomar Observatory, as it did using a telescope built at the end of the last century, the result of image "flickering" attributable to motion in the earth's atmosphere. The influence of the earth's atmosphere can be degraded somewhat by sending the instrumentation, installed in balloons, to maximum altitudes of 30 km. /5*

Rocket developments have eliminated the limitations inherent in observations made from the ground, and have resulted in a new, qualitative leap being made in investigations of the earth, near space, and celestial bodies. The great many high-altitude rockets and artificial earth satellites have contributed to expanding our knowledge of the earth and of near space extensively, have made it possible to discover the earth's radiation belts, to build television and telephone "radio bridges" between the continents on our planet, and to organize what is virtually a global weather service. Equipment installed in artificial earth satellites assists in investigating the earth's natural resources and other riches, in mapping the earth's surface, and, in the case of ships, in fixing their positions at sea. Flights of space vehicles to the Moon, Mars and Venus have added to our knowledge of these celestial bodies and their environments, as well as to the making of a unique re-evaluation of priorities. Conquering of remote space by space vehicles has changed the outlook of such sciences as astrophysics, radioastronomy, and of certain of the other sciences formerly thought of as "pure" sciences. Solar system researchers were faced with practical problems, answers to which resulted in optimum design solutions in building space vehicles. /6

---

*Numbers in the margin indicate pagination in the foreign test.

The flight of space vehicles to the moon, the landing of automatic stations on the lunar surface, putting automatic stations into the orbit of artificial lunar satellites, the flight of man to the moon and bringing him back to our planet, have required detailed information of every description on the nature of the lunar surface, and of its surface layer, as well as of circumlunar space. And these data were required for purposes of studying the "average" characteristics of the lunar surface, as well as for studying concrete portions of its surface measured in square kilometers as well as in hundreds, and tens, of square meters. No previously known method of observations from the earth could begin to provide so high a degree of resolution. This did not become possible until space vehicles were orbited in circumlunar space and were landed on the lunar surface to make observations. These provided valuable data on the nature of the lunar atmosphere, surface, and surface layer.

A great deal of information on the nature of the lunar surface, and of the surface layer, prior to the space age came from the many years of ground astronomical observations. Visual and photographic observations from the ground were the media for studying large formations on the near side of the lunar surface, and for establishing their location and size. This, in turn, led to an estimate of the steepness of the slopes of these formations from the shadow they cast.

Nevertheless, lunar surface resolution by this procedure was no better than 800-2000 meters in the center of the disk because of the fluctuation in the index of refraction for the earth's atmosphere. The lunar chart compiled from ground observations was scaled at $1 : 10^6$. Accuracy in determining surface slopes in the center of the lunar disk was no better than 30 percent on this chart when the base was longer than 1 km. In resolution, this was equivalent to a map scaled at $1 : 10^7$.

Recent photography of the lunar surface from space vehicles has resulted in the compilation of a complete lunar chart at a scale of $1 : 5 \cdot 10^6$, and the accuracy with which the slopes can be established is of this same order of magnitude, and surface resolution is under 500 meters. Individual portions of the lunar equatorial region were photographed at scales of $1 : 10^4 - 1 : 10^5$.

Panoramic photography, taken for the first time by Luna 9 and Luna 13, and the photography taken by the Surveyor missions, made it possible to research the microstructure of the lunar surface layer in the landing sites of these stations.

A great many rocks and blocks found on the lunar surface were fixed from the photographs made by the artificial lunar satellites and stations landed on the lunar surface. An approximate estimate of soil strength was based on /7
the tracks these latter left on the surface.

Photometric and spectroscopic observations in the optical spectrum from the earth resulted in determination of the albedo and scattering indicatrix for the whole of the lunar disk, as well as for individual surface formations, and this, in turn, provided the means for using modeling to select earth rocks with the same optical characteristics.

The work by N. P. Barabashov, and his coworkers, showed that the upper mantle of the moon most resembled a finely porous material, in which the material itself occupies ~10 percent of the total volume [9, 10, 75]. Measurements of the moon's photometric function revealed that its surface is quite rough, with the dimensions of the irregularities greatly in excess of the wavelength and that portion of the lunar surface shading itself [56, 67, 68].

Measurement of the moon's inherent radiation in the infrared and radio spectra made it possible to measure the brightness temperature of the entire lunar disk, as well as that of individual lunar formations, and the change in this temperature during lunation and eclipse. These measurements were made in the "window" of the earth's atmosphere in the 1.5-1.8, 2.0-2.5, 3-4, 4.5-5, and 8-13 micron limits of the infrared band and ~8 mm to 18 m in the radio frequency band.

This set of brightness temperature measurements provided the means for deriving the deep temperature cross-section of the lunar surface layer and the temporal change in the temperature at depths from a few millimeters to several meters. Study of the temporal change in brightness temperature derived the parameter of the thermal inertia, γ, for different depths of the surface layer. The parameter γ is the product of three magnitudes: thermal

conductivity, k; specific heat, c; and density ρ.

$$\gamma = (k\rho c)^{-\frac{1}{2}}.$$

This method derives γ for different wavelengths, but does not permit the calculation of the value of magnitudes k, ρ, and c. V. S. Troitskiy developed the method for establishing the physical and thermal properties of the material of the moon's upper mantle (k, ρ, c). Here, along with the results of the measurement of γ, obtained by using the formula given above Troitskiy used the values of the reflectivity of the material of the moon's surface layer, obtained after processing the data from radar and polarization radioastronomical measurements. Data on the magnitude of the heat flux from the lunar nucleus attributable to the moon's radioactivity [71] were used to determine the nature of the material at great depths (beginning at a few meters), where temperature is practically invariable.

Troitskiy's polarization coefficient/permittivity ratio and the distribution law for slopes of irregularities on the planet's surface can be used to process the radioastronomical polarization measurements. Analysis of these relationships for polarization coefficients in terms of angle of incidence derive the reflection factor, permittivity, and root-mean-square values for the slopes of the real surface to the ideal sphere [72]. This method now is widely used, is quite universal, and can be used in the course of ground observations, as well as when the measurements are made from space vehicles. /8

Radar investigations of the moon from the earth and from space vehicles simultaneously pursue a dual purpose. First of all, these investigations provide information on the characteristics of the reflection and scattering of radio waves in the medium for the entire moon, and for individual parts of its surface. Knowledge of these characteristics is necessary for the correct selection of the parameters of the electronic equipment for installation in the space vehicles sent into circumlunar space, and landed on its surface, as well as for that installed in ground stations controlling these space vehicles.

Second, the radar method of investigating the moon provides information on the physical characteristics of its surface and of its surface layer. It enables us to estimate such parameters of the material of the upper cover as the effective permittivity and the reflection factor, as well as change in

the properties of the material with depth, that is, to obtain materials for building a model of the planet's surface layer (using the frequency relationships of the parameters cited).

Radar methods of investigating from the earth, and from space vehicles, today are widely used, not only when investigating the moon, but also when investigating other planets in the solar system, primarily because they are highly informative.

This book summarizes the data on radar investigations of the moon made up to the end of 1968, from the earth, as well as from space vehicles.

The author wishes to take this occasion to express his deep appreciation to Professors V. I. Moroz, D. Ya. Martynov, V. S. Troitskiy, and Yu. K. Khodarev for their assistance in the work and for the joint discussion of the material contained in the book.

CHAPTER I

/9

A SHORT SURVEY OF DATA ON THE MOON, AND ON ITS SURFACE AND SURFACE LAYER, OBTAINED FROM MEASUREMENTS MADE FROM THE EARTH AND FROM SPACE VEHICLES

1. Motion, Dimensions, Mass, Density

The moon is a natural satellite of the earth. The moon's orbit around the earth can be described in approximation as an ellipse, the radius vector of which varies from 354,410 to 406,697 km. According to radar data, the mean distance from the earth to the moon is 384,402 ± 1.5 km, 60.267 times the equatorial radius of the earth. These distances correspond to an apparent angular diameter of the moon from the earth varying from 24'24" to 33'34", with a mean of 31'04".

E. Braun's calculations show that the eccentricity in the lunar orbit varies with a period of 8.85 years, from 0.0435 to 0.0715. The mean inclination of the plane of the lunar orbit to the plane of the ecliptic is 5°08'43.4", and varies between 4°59' and 5°18'. The inclination of the plane of the lunar equator to the plane of the ecliptic is 1°32.1'.

The period of the moon's revolution around the earth is 27.322 earth days. Lunar days last from 29.25 to 29.83 earth days. This corresponds to a mean angular rate of rotation of the moon about its axis of 33 minutes of arc per hour, a mean angular rate of motion of the moon in the celestial sphere of 30.7 minutes of arc per hour, and a mean rate of motion of the moon in orbit around the earth of 1.02 km/hr.

The moon rotates about its axis with a constant mean angular velocity and period equal to the period of its revolution around the earth. This is why the same side of the moon always is seen from the earth. However, because of the variation in the rate of revolution during its movement in the elliptical orbit, libration in longitude of ±7°54' occurs, and, because of inclination in the axis of rotation of the moon to the plane of its orbit around the earth, libration in latitude is ±6°50'. Libration results in 59 percent, rather than 50 percent, of the lunar surface being seen from the earth.

The moon is not a spheroid. Hypsometric measurements made by I. V. Gavrilov [19] have shown that the moon can be represented by a triaxial ellipsoid with its axes coinciding with the coordinate axes of the moon, assuming a uniform lunar structure. This being so, the lengths of the semiaxes of the ellipsoid can be expressed by the following magnitudes: /10

$a_x = 1738.30 \pm 0.07$ km (the x axis that of the Earth-Moon);

$a_y = 1735.80 \pm 0.12$ km (the y axis east);

$a_z = 1736.42 \pm 0.10$ km (z axis north).

The mean radius of the moon, at which the entire volume of the body of the moon will be contained within the spherical surface is $a_m = 1737.2 \pm 0.03$ km, according to hypsometric measurements. The true altitudes of points on the near and far sides of the moon are calculated from these measurements.

Visual and radar observations from the earth have provided the following value for the mean radius of the moon: $a_m = 1738 \pm 0.5$ km [38]. The mean radius of the moon used in calculations is $a_c = 1738$ km.

The moon's mass, determined by the gravity method, as well as by the motion of the center of gravity of the Earth-Moon system, is less than the earth's mass by a factor of 81.31, and equals $7.35 \cdot 10^{25}$ grams.

The moon's volume is $2.2 \cdot 10^{25}$ cm^3, less than the earth's volume by a factor of 48.4.

The mean density of lunar material, determined as the mass/volume ratio, equals 3.33 ± 0.012 grams/cm^3, not much more than the density of earth rocks (2.5-3 grams/cm^3), but less than the mean density of the earth by a factor of 1.65.

The acceleration of free fall at the lunar equator is $g = 1.62$ m/sec^2, less than that for the terrestrial equator by a factor of 6.05.

The lunar surface area is $3.79 \cdot 10^7$ km^2, less than the earth's surface area by a factor of 13.23.

2. Surface Macrorelief

The greater part of the lunar surface consists of lighter areas that have come to be called the continents. The continents comprise 70.2 percent

of the surface on the near side of the moon, and if the far side of the moon is considered, the continents comprise 83.9 percent of the lunar surface. The continental regions are higher than the maria regions, and the mean level of the continents is 1.41 km above the mean level of Oceanus Crocellarum [19, 61].

If one considers the distribution of mean altitudes for the entire lunar surface relative to zero altitude, which is at a distance a = 1738 km from the center of mass of the moon, 10 percent of the entire surface area will have altitudes of from +2 to +6 km, 20 percent of the entire area depressions from -2 to -7 km, and 70 percent of the entire surface area will have altitudes between -2 and +2 km. The mean level of the maria regions too is heterogeneous. The maximum spread between them is 3.3 km [19, 20].

The lunar surface is covered with a great many craters. The distribution of craters differs slightly from the normal distribution law with respect to size. The number of craters increases rapidly with decrease in size. Visual observations of the near side of the moon from the earth have found 5 craters with diameters larger than 200 km, 25 with diameters larger than 120 km, 170 with diameters larger than 50 km, and 30,000 with diameters larger than 1 km (the limit of the resolution of earth telescopes) [8, 13]. /11

Study of photography by artificial moon satellites and by space vehicles that have landed on its surface has found craters and depressions with diameters of less than 20 cm (in the mountain, as well as in the maria, regions of the moon). Study of the large craters (those with diameters > 10 km) on the near and far sides of the moon has provided a mean wall height of 0.5-1.5 km, with a maximum of 5 km. Crater depths range primarily from 0.5 to 4.5 km, with a maximum depth of 9 km [51]. The slope of the outer slopes of the craters is less than 10°, on the average, with the maximum slope 20° [34]. Slopes of the inner walls of the craters on the near side average 12°, with their maximum 35° [47]. The slopes of the inner walls of craters on the far side of the moon range from 5° to 10°, with the maximum 22° [8].

The highest mountain formations on the near side are 8 to 9 km. The surface of maria regions usually is quite flat. The root-mean-square value of the slopes for sections larger than 10 km in extent in these regions is a maximum of 3° [51]. /13

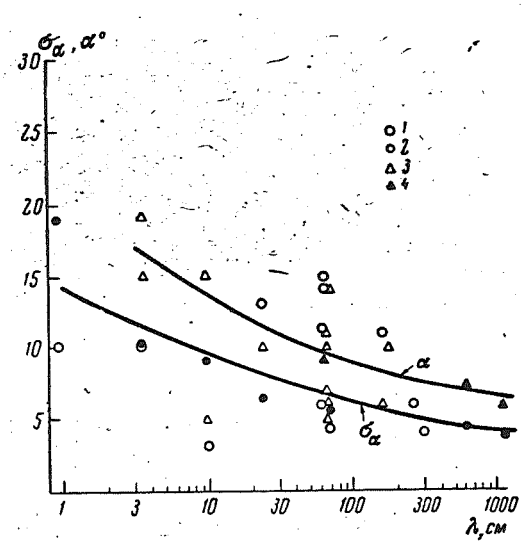

Figure 1.1. Mean α and root-mean-square σ_α values of gradients of the lunar surface in the central part of the disk (data from radar measurements, see #3, Chapter V).

1 - σ_α calculations (different authors);
2 - σ_α calculations (data in this work);
3 - α calculations (different authors);
4 - α calculations (data in this work).

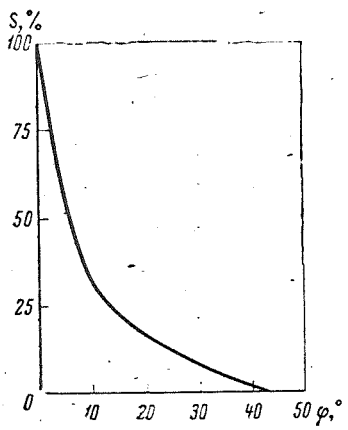

Figure 1.2. Distribution of gradients over the lunar disk for a base of approximately 10 km. S is the probability of finding gradients exceeding a given angle.

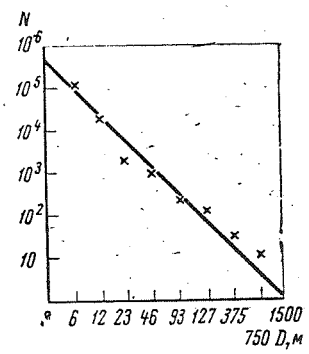

Figure 1.3. Distribution of small craters from interpretation of photography from the Ranger program. N is the number of craters. D is crater diameter.

/12

Radar measurements of the moon from the earth have made it possible to determine the mean gradients in the central part of the lunar disk. Figure 1.1 shows the gradients in terms of wavelength, obtained by processing radar measurements. The base for the determination of gradients equals 10 wavelengths. Interpretation of lunar photography, obtained by ground observatories, provided the distribution of surface gradients on the near side of the moon for a base of approximately 10 km. Figure 1.2 shows this distribution.

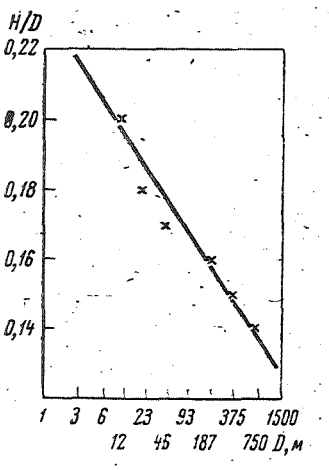

Figure 1.4. Relative depth, H, of small craters in terms of their diameter, D, from interpretation of photography from the Ranger program.

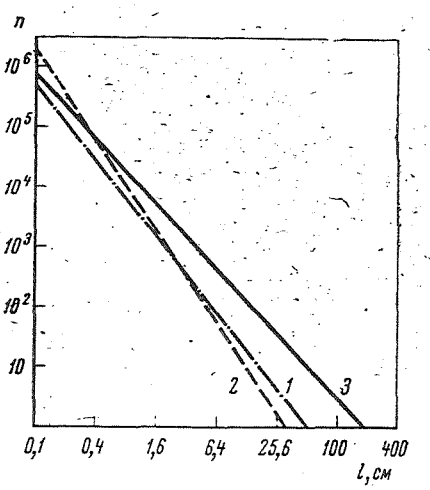

Figure 1.5. Distribution of rocks to 2 meters in size from interpretation of photography from the Surveyor spacecraft. n is the number of rocks per 100 m^2. l is the maximum size of the rock.

1 - Surveyor 1 2 - Surveyor 6
3 - Surveyor 7

Interpretation of the photography from the Ranger program provided the distribution of craters with diameters D of up to 1,500 meters in size (Figure 1.3, 1.4).

Lunar surface photography, obtained by orbiting space vehicles, and by space vehicles landed on the surface, shows a great many rocks measuring from 1 mm to several tens of meters on the lunar surface. Some of these rocks and blocks are on the surface, others are partially buried, and others are almost completely buried. Figure 1.5 shows the distribution of rocks measuring up

to 2 meters within a 100 m^2 area, obtained from interpretation of the photography from the Surveyor program [85]. The photography taken by Lunar Orbiter 4 and Lunar Orbiter 5 in the Schroter's Valley, Marius Hills, and Prinz Valley regions showed rilles over a hundred kilometers in length and several kilometers wide. H. C. Urey [172] suggests that they are the result of liquid flows.

3. Surface Microstructure

The overwhelming percentage of information on the microrelief of the lunar surface has been obtained from photography taken by space vehicles. Ground polarization and photometric measurements of the distribution of visible light over the disk indicate quite a rough surface on the wavelength scale [10, 11].

Investigation of the soil in the landing areas for Luna 9 and Luna 13, and for the Surveyor series, has shown that the soil in the maria and continent regions has a similar microstructure, consisting of stony and aggregate fractions.

The photography taken by the Surveyor and Luna 13 spacecraft showed lumps of a friable material consisting of finely dispersed bound particles. These lumps are right on the lunar surface, as well as on some rocks, and exhibit good cohesion.

The soil at the Luna and Surveyor landing sites is porous and crumply in structure. /14 There is a considerable variation in grain size. The grains have weak bonds at the points of contact. Grain size varies from 2 to 60 microns, with the mean about 10 microns [78, 85]. Unbound, structureless dust layers have not been observed at the landing sites of the first unmanned spacecraft, Luna 9, Luna 13, and Surveyor 1 [11]. Nor did the experiment using the jet stream of the Surveyor 5 thrusters to stir up the surface layer show an unbound, finely dispersed dust layer [134]. But individual, finely divided particles (dust) measuring less than 70 microns have been found on the surface, in crevices, on the sloping planes of individual rocks, as well as on the landing pads of Surveyor 5 [85]. The results of radio observations from the earth, as well as photometric measurements made by the Ranger series, revealed that there should be no appreciable dust layer on the moon.

4. Physical and Chemical Characteristics of the Lunar Surface Layer

The results of radar and radio observations from the earth show that the density of the surface layer material increases with depth. The dependence of density of the material on depth also was noted during the direct measurements made by the Surveyor spacecraft. V. S. Troitskiy's calculations [71, 72], made using data from radio observations and measurements in the infrared region, showed that the lunar surface layer can be represented by a four-layer model. The first, or upper layer, has a density of $\rho = 0.6\ ^{+0.2}_{-0.1}$ g/cm^3, and is 3 to 4 cm thick. Porosity of the material in this layer is 70 to 80 percent. The second layer extends to a depth of 4 ± 1 meter, and has a density of $0.9^{+0.3}_{-0.2}$ g/cm^3 and a porosity of 55 to 65 percent. The third layer is 2 to 5 meters thick, has a density of 1.1 to 1.2 g/cm^3 and a porosity of 10 to 30 percent. Dense rocks lie deeper than 6 to 10 meters.

Direct measurements at the Luna 13 landing site, made by a gamma densimeter, showed a maximum layer depth of 5 cm, $\rho = 0.8$ g/cm^3 [78]. Measurements made by the spacecraft in the Surveyor series showed that the density of the material at a depth of a few millimeters is ~ 1 g/cm^3, the porosity about 70 percent. The material at a depth of about 5 cm has a density per unit area of about 1.5 g/cm^3 and a porosity of 40 to 50 percent [85].

The depth of the layer consisting of the loosely bound particles varies from 1 to 20 meters in the maria areas investigated by the Surveyor spacecraft, based on estimates of the results of their measurements, and from 1 to 100 cm in the area where Surveyor 7 landed (the mountain region near the crater Tycho). L. D. Jaffe estimates that the depth of this layer can exceed 1 meter in other mountain regions. Below the layer consisting of the loosely bound particles (a continuously plowed layer) is a material with high density and greater cohesion [85]. The processed data from the Ranger series provide an estimate of the depth of this continuously plowed layer as 10 to 20 meters in the maria regions. The average bearing capacity of lunar soil is estimated to be a minimum of 0.4 kg/cm^2 for a depth of 5 cm [23]. Direct measurements made by Luna 13 show the bearing capacity of the upper layer of the soil, up to 5 cm in thickness, to be 0.68 kg/cm^2. Surveyor measurements have shown

/15

that the bearing capacity increases almost linearly with depth to 5 cm and a gradient of 0.1 kg/cm^3, 0.01 kg/cm^2 at a depth of 1 mm, and 0.5 kg/cm^2 at a depth of 5 cm. Surveyor 3 measurements showed an increase in the bearing capacity of the soil with depth to the maximum depth measured, 18 cm. Surveyor measurements further showed an increase in the cohesion of the particles in the surface layer material with depth. Cohesion was 0.0005 kg/cm^2 at a depth of 1 mm, reaching 0.005 kg/cm^2 at several centimeters, and there was a definite tendency to a further increase at even greater depths.

Rocks strewn about the lunar surface have a calculated density of about 3 g/cm^3. The density of the rocks, several centimeters in size, at the Surveyor 7 landing site was determined as 2.8-3.2 g/cm^3, with the most probable value between 2.8-2.9 g/cm^3. The pressure required to crush these rocks was 200 kg/cm^2 [85].

Chemical analysis of the material, based on measurement of the α-particle and proton scattering flux in the vicinities of the landing sites for Surveyor 5, Surveyor 6, and Surveyor 7 (see Table 1.1), revealed that the measured element composition can best correspond to earth silicates of the ironized basalt type [85, 169] with the following chemical composition: 5% MgO, 14% Al_2O_3, 50% SiO_2, 15% CaO, 16% FeO. The surface layer material in the mountainous region near the crater Tychos (Surveyor 7) contains less iron than does the material in the two maria regions investigated. A. Turkevich and L. D. Jaffe [85] suggest that this fact can be the reason for the different albedo in the optical region for maria and continent regions. They are of the opinion that differences found in the electromagnetic properties of the material in the maria and continent regions also would appear to explain this.

Earlier measurements by Luna 10 and Luna 13 revealed that the material /16
of the moon's upper mantle does not belong to acid rocks, but is an analog of basic earth rocks of the basalt type [18]. The lunar surface layer contains radioactive potassium, uranium, and thorium. A. P. Vinogradov, as well as others, estimate that the concentrations of these materials in the lunar surface layer is 1.5 to 2 times that of their concentrations for rocks comprising the earth's crust.

TABLE 1.1

Chemical element, % by no. of atoms	Surveyor 5	Surveyor 6	Surveyor 7
	mare regions		continent
	at a depth of several mm	on the surface	
C	< 3	< 2	< 3
O	57±5	57±5	58±5
Na	< 2	< 2	< 3
Mg	3±3	3±3	4±3
Al	6.5±2	6.5±2	9±3
Si	19±3	22±4	18±4
Ca group (atomic weight 30-47)	13±3	6±2	6±2
Fe, Co, Ni group (atomic weight 47-65)		5±2	2±1

5. Thermal Properties of the Surface Layer of the Near Side of the Moon

Thermal conditions in the surface layer are determined by the thermal properties of the material and by the radiation balance. Temperature drops on the lunar surface are very great, the result of the lack of atmosphere and the low thermal conductivity of the surface layer material. Measurements in the infrared region show 395°K for the subsolar, and 100°K for the antisolar, point on the surface [160]. The mean temperature of the lunar surface as a whole, in terms of time, is 212°K, and 230°K at the equator [71]. The surface temperature drops 190° in 1.5 hours during lunar eclipses. And the rate of change in temperature is 2.8 degrees/minute [11].

According to the calculations made by V. S. Troitskiy, the mean temperature in the upper part of the porous layer, in terms of surface and of time, increases exponentially to a depth of 8 to 10 cm, increasing 15 to 20°K. The temperature gradient at greater depths is 8 degrees/meter, approximately [73]. The temperature should be about 600°K at a depth of 40 kilometers, according to the calculation [71]. The depth to which temperature variations penetrate (the depth at which temperature variations decrease by a factor of /17

e as compared with temperature variations on the surface) during the time of a lunar day is 7 to 8 cm. The surface layer cools to a depth of 1 to 2 cm during the lunar eclipse, which lasts 4 to 5 hours. There are no temperature variations during the lunar day at a depth of 40 cm. The temperature is $225 \pm 5^{\circ}K$ at this depth at the lunar equator [71]. The thermal conductivity coefficient, equated to $300^{\circ}K$, is as follows for the 4-layer model of the lunar surface layer considered in the foregoing [71]: for the upper layer, 3-4 cm thick, $k_1 = (0.7 \pm 0.3) \cdot 10^{-5}$ cal$\cdot$cm$^{-1}\cdot$sec$^{-1}\cdot$deg^{-1}; for the second layer, extending to a depth of 4 ± 1m, $k_2 = (1 \pm 0.4) \cdot 10^{-5}$ cal$\cdot$cm$^{-1}\cdot$sec$^{-1}\cdot$deg^{-1}; for the third layer, 2-5 meters thick, $k_3 = 10^{-3}$ cal$\cdot$cm$^{-1}\cdot$sec$^{-1}\cdot$deg^{-1}. The thermal conductivity coefficient for rocks is $k_4 = 5 \cdot 10^{-3}$ cal$\cdot$cm$^{-1}\cdot$sec$^{-1}\cdot$deg^{-1}.

The parameters of the thermal inertia for this model, $\gamma = k\rho c^{-\frac{1}{2}}$, are as follows for the first and second layers of this model (in cal$^{-1}\cdot$cm$^{2}\cdot$sec$^{\frac{1}{2}}\cdot$deg):

at $0^{\circ}C$ $\gamma_1 = 1000$, $\gamma_2 = 800$;
at $300^{\circ}C$ $\gamma_1 = 800$, $\gamma_2 = 700$.

Over 400 points with increased temperature were found upon measuring the distribution of the lunar disk temperature brightness in the infrared region during eclipses. Some of these points have been identified from photography, or by craters with ray systems, or by lighter spots on the lunar surface. Resolution on the lunar surface was $\sim$ 20 km during these measurements. The largest thermal anomalies (30 to 40°) have been equated to craters with large ray systems. These anomalies can be explained by increased thermal fluxes, or by reduced thermal inertia, γ , in the particular lunar regions [58, 160]. If these anomalies can be explained by change in the magnitude of the thermal inertia parameter, the magnitude of the parameter γ (in cal$^{-1}\cdot$cm$^{2}\cdot$sec$^{\frac{1}{2}}\cdot$deg) will be as follows for certain craters: Kepler -γ = 580; Aristarchus - 315; Copernicus - 316; Tycho - 182.

Reduction in γ for these craters can be connected with the youth of these craters since they can have a thinner plower layer and, as a result, greater density than the surface surrounding them [58, 151]. The results of the photographic interpretation made by G. P. Kuiper [142] of Ranger 9 photography also is suggestive of the increased density of the walls of the crater Aristarchus.

Radio astronomical observations, made on wavelengths of 3, 4, 8, 8.6, and 16 mm, have yielded results to show that as a rule the maria are 3-6° warmer than the continents, indicative of their lower (4-20 percent) radiation capacity when compared with the continents [30, 50, 142, 163] ($\gamma_{maria} < \gamma_{continents}$).

Measurement of surface temperature in the landing areas used for the Surveyor series revealed taht the maximum value for the temperature for an area 10-20 meters on a side coincided with the results of temperature measurements in the infrared region of the same regions on the earth, but with a resolution of 18 km. However, the value of the thermal inertia parameter is somewhat less than that found by ground measurements, according to Surveyor data [85]. /18

6. Properties of the Surface Layer of the Near Side of the Moon in the Optical, Infrared, and Ultraviolet Regions

Measurement of the reflecting properties of the lunar surface in the optical region have revealed that the lunar surface is much darker than the terrestrial surface. A comparative evaluation reveals that the mean spherical albedo of the moon, $\bar{A}_s$, in the optical range is less than the terrestrial albedo ($A_{s☾} = 0.067$, $A_{s♁} = 0.36$) by a factor of 54 [36]. Measurements on the mean wavelength in the optical range ($\lambda = 0.55$ microns) provided the following results: $A_{s0.55☾} = 0.073$, $A_{s0.55♁} = 0.401$) [13].

The measurements revealed that the reflecting properties of the moon change with the wavelength. If, for example, the spherical albedo on $\lambda = 0.4$ micron is $A_{s0.4} = 0.05$, on $\lambda = 0.65$ micron the value of the spherical albedo increases to $A_{s0.65} = 0.085$. The lunar continents are brighter than the maria. The spherical albedo is $A_{s0.4} = 0.07$ on $\lambda = 0.4$ micron for the continents, and $A_{s0.4} = 0.03$ for the maria. The spherical albedos for continents and maria are, respectively, $A_{s0.65} = 0.116$ and 0.055 on $\lambda = 0.65$. However, the mean values for the spherical albedo in the optical region for the maria and continents are, respectively, $A_s = 0.088$ and 0.044 [53]. The continents, therefore, have an albedo that is higher by a factor of 2 than that possessed by the maria regions. Figure 1.6 shows the spherical albedo, A_s, in terms of the wavelength, λ, in the optical, infrared, and ultraviolet ranges.

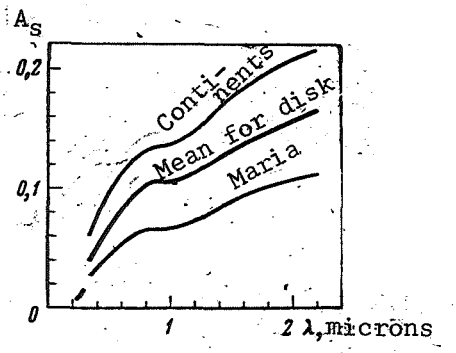

Figure 1.6. Spherical albedo, A_s, of the moon in terms of the wavelength, λ in the optical, infrared, and ultraviolet regions.

Measurement of values of the mean visual albedo for individual sections /19
of the lunar surface in the optical range has revealed that if its mean value for the disk at full moon is $\bar{A}_v = 0.098$ the lightest section of the lunar disk (the bottom of the crater Aristarchus) has $A_v = 0.176$, and the darkest section in the region of Oceanus Procellarum has $A_v = 0.051$. At the same time, the mountain regions, the ray systems of craters, and the walls rimming the craters, have the higher albedo values. A_v at full moon has the following values: for light rays 0.131; for dark craters 0.065; and for maria regions 0.065. The ratio of the spherical to the geometrical albedo (the phase integral) for the moon is $Q = 0.585$ [36].

Interpretation of photography obtained from spacecraft has revealed that the lunar surface layer is lighter than the underlying surface, but some of the rocks found on the lunar surface are lighter than the uppermost surface layer [161]. Photography of the lunar surface taken from the earth, as well as from spacecraft, through color filters has revealed that the color of the lunar surface generally is gray-brown, with some color differences in individual regions. Maria regions have a more reddish hue than do the continents. The Ranger 7 and Ranger 8 photography showed color differences in individual sections of maria regions. Noted as well was the fact that the lower, older lava flow was redder than the upper flow [164]. Photography of Surveyor series landing sites made by the spacecraft, showed that the color of surface and rocks was gray [85].

Lighting engineering calculations have shown that the illumination at the subsolar point on the lunar surface is equal to 135.10^3 luxes [51]. The maximum illumination $\pm 50^o$ from the center of the disk attains a magnitude of 12 luxes during the lunar night, the result of the scattering of the solar light by the earth during full earth. However, this magnitude can change by a factor of 2, approximately, because of change in the albedo of the terrestrial surface as the earth rotates, and because of the change in the earth's cloud cover. Figure 1.7 shows the mean illumination in terms of the phase of the earth, using data contained in reference [3]. For comparison, it should be noted that illumination on the surface of the earth at night at full moon and short zenith distances ($< 40^o$) equals 0.342 ± 0.11 lux, disregarding losses in the atmosphere.

The stellar magnitude of the full moon is $-12^m.76$, according to Ye. K. Nikonova's measurements [55].

Measurement of the moon's brightness during eclipses has revealed that the brightness is not a constant magnitude. It changes from eclipse to eclipse, and the overall change in the brightness is twofold. The brightness of lunar eclipses is less than the brightness of the full moon by a factor of $2 \cdot 10^5$, on the average.

The flux of ultraviolet radiation from the moon in the regions of the spectrum with a half-width of 150 Å centered relative to the wavelengths 0.29, 0.27, 0.25, and 0.24 microns, was measured during two flights of the high- /20
altitude rockets of the Aerobee type. It was found that the flux magnitude drops quickly with shortening of the wavelength. Caver and Norton [99] calculate the magnitudes of the spherical albedo to be $A_s = 0.01$ on $\lambda = 0.29$ micron, and $A_s = 0.007$ on $\lambda = 0.24$ micron.

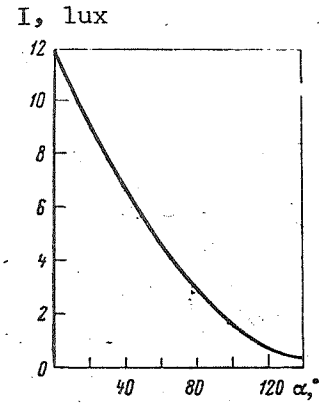

Figure 1.7. Mean illumination on the moon in terms of the phase of the earth.

The moon's albedo has been measured from the earth in the infrared region in the window on λ = 2 microns. According to the data in reference [53], the value of the spherical albedo for the entire disk is $A_{s2.0}$ = 0.155. The spherical albedo for the mountain regions is $A_{s2.0}$ = 0.106. In other words, the ratio of the albedos for maria and mountain regions is of the same order of magnitude in the infrared and in the visible regions of the spectrum.

Measurements of the infrared radiation spectrum between 3.5 and 3.9 microns by Zond 3 provided a mean value of the visible albedo for normal incidence of $A_{v3.6}$ = 0.75-0.85, according to the data provided by G. A. Leykin and T. Ye. Shvidkovskaya [48]. This photography, when processed photometrically, revealed that the deviation in the visible albedo for individual sections was a maximum 0.02.

N. S. Orlov [56] and V. A. Fedorets [75] measured the scattering indicatrix for the moon in the optical range and found that it was elongated in the direction of the incident flux, and that the degree of elongation increased with increase in the angle of incidence. The degree of elongation of the indicatrix is different for different structures of the lunar surface, being more elongated for rayed craters and bright craters than for the maria. Orlov, Fedorets, and N. P. Barabashov [88] all note that maximum brightness of individual sections of the lunar surface, when observed from the earth, occurs near full moon, and not at local noon. This can be explained by the large elongation in the scattering indicatrix for the moon in the direction of incident light, associated with the extremely rough surface and the shadows on sections of the surface cast by irregularities in the surface when angles of observation differ from the angles of incidence. /21

The question of illumination in the shade during the lunar day is a special one. The assumption, until recently, had been that because of the low value of the lunar surface albedo the magnitude of the flux of scattered light was very small, and that as a result the illumination in the shade was at best a few luxes. Barabashov and his group subsequently have taken photographic measurements that show illumination in the shade can be as high as 200 luxes.

7. Electromagnetic Properties of the Lunar Surface Layer Material

Radar and radioastronomy observations of the moon from the earth have confirmed the hypothesis concerning the considerable porosity of the moon's upper cover, and direct measurements, made by spacecraft landing on the lunar surface, too have shown this to be so. Radar and radioastronomy observations from the earth, and from spacecraft, have revealed that the material of the lunar surface layer is heterogeneous, and that its properties change with depth.

However, the radar and radioastronomy data, when used to calculate such characteristics as the permittivity and the density, yield different results. The effective permittivity obtained using radar measurements in the millimeter band, and in the lower part of the centimeter band, is higher than that obtained using the radioastronomy data by a factor of ~ 1.5. Nevertheless, when B. Ya. Losovskiy [49] processed his radioastronomy observations of the moon on a wavelength of 8 mm, it was found that consideration of the diffuse component of the moon's r-f thermal radiation on this wavelength results in coincidence in the results of the determination of the permittivity using radioastronomy and radar methods.

Chapter V contains the procedure used to calculate the reflectivity from the results of radar measurements, and makes the calculation for the reflectivity from the effective permittivity. Consideration, during radar measurements, of the diffuse component of the reradiated signal, and of reflections from large irregularities results in the calculation of the magnitude of the permittivity, ϵ , which proves to be very close to that determined by radio astronomy methods. Figure 1.8 shows these data. V. S. Troitskiy's data provide an effective permittivity for the four-layer model he worked with of $\epsilon = 1.7 \pm 0.2$ for the first layer, and 2.3 ± 0.2 for the second.

The artificial moon satellite, Explorer 35, was used for an experiment /22
designed to measure the lunar magnetic field, as well as that of the space about the moon. N. F. Ness et al. processed the results [152], finding that the strength of the moon's magnetic field equals $(8 \pm 0.3)\ \gamma$. The corresponding magnetic permeability of the lunar material is $\mu = 1.8\ \mu_0$, where μ_0 is

the permeability of space. Earlier measurements of the moon's magnetic field by Sh. Sh. Dolginov [24], using Luna 10 data, yielded a somewhat larger magnitude for the strength of that field.

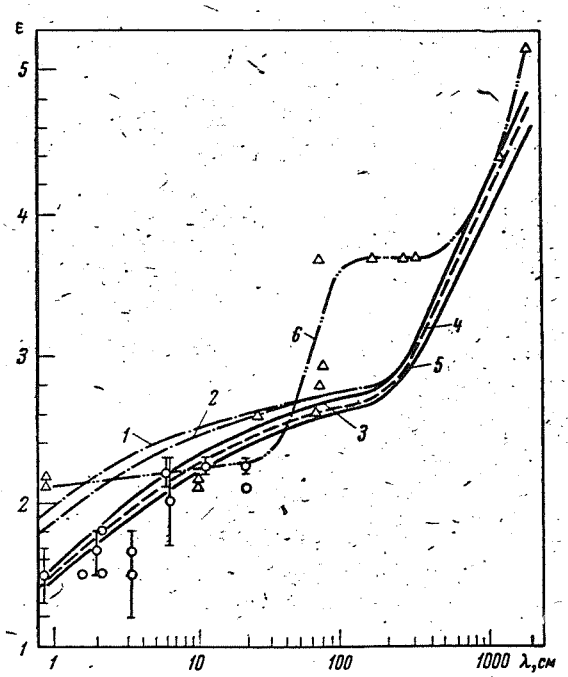

Figure 1.8. Effective permittivity, ε, of the material of the moon's upper cover in terms of wavelength λ. The circles are for the results of radioastronomy determination of ε. The triangles are the results of the calculations from data for determining ρ_{mN} from the radar measurements (see Table 5.2).

1 - the curve for $A_i = \rho_{mN}$, $g_m = 1$;

2 - for $A_i = \rho_{mN}$, $g \neq 1$;

3 - for $A_i = 0.07$, $g \neq 1$;

4 - for $A_i = 0.158$, $g \neq 1$;

5 - for $A_i = 0.379$ and 0.9, $g \neq 1$;

6 - curve corresponding to $\rho_{mN} = f(\lambda)$ depicted by curve 6 in Figure 5.1.

No direct measurements of the conductivity of the material of the moon's upper cover have yet been made. The results of modeling material similar to the material of the moon's upper cover, however, have put the conductivity of this material in the r-f region. The measurements by V. S. Troitskiy et

al. [71, 73] result in the following findings with respect to the tangent of the angle of lunite losses for the first and second layers of their proposed four-layer model: for the 1st layer tan $\Delta = (0.45\text{-}1)10^{-2}$; for the 2nd layer tan $\Delta = (0.55\text{-}1.2)10^{-2}$. /23

Measurement of the rate of flow of the magnetic field through the body of the moon, as compared with the solar wind convection rate, obtained by Explorer 35, resulted in a determination of the upper limit of the moon's conductivity for a constant current. Ness' calculations [54] revealed that, if the moon is represented in the form of a homogeneous sphere in which the currents flow along a normal to the surface, and if the moon does not have a magnetic field, the effective conductivity will be 10^{-5} mho/m; that is, the resistivity of the material will be 10^5 ohms-m, and this is the same as that of a dielectric with low conductivity.

Radio wave reflectivity for broadside incidence varies with the wavelength of the radiation, according to the results of radar observations of the moon from the earth. The calculations in Chapter V show that broadside incidence varies from 1 to 15 percent in the band of wavelengths from 0.86 cm to 20 m.

The moon's radar cross section, σ [m^2], equated to the area of its disk, varies from 0.06 to 0.16 [39, 109] in this same band of wavelengths, from 0.86 cm to 20 m (see #1, Chapter IV).

The width of the back scattering pattern decreases with increase in the wavelength. Calculations show that it varies from ±40 to ±2.5 at the 0.5 level for change in wavelength from 0.86 cm to 20 m [39] (see #2, Chapter IV).

The moon's smoothness factor, g_m, fro the r-f region varies from 1.3 to 1.06 for change in wavelength from 0.86 cm to 11.3 m (see #1, Chapter V).

According to the calculations, the moon's radar cross section per unit area intercepted by an antenna beam for broadside incidence (the mean cross section of 1 m^2 of the near side of the lunar surface for the case of broadside incidence) varies from 0.1 to 7 in the band of wavelengths from 0.86 cm to 3 m (see #3, Chapter IV). Measurements of the radar cross section per unit area for the surface layer, made by Luna 9, Luna 13, Surveyor 1, and Surveyor 3 in the maria regions of the moon failed to reveal any significant

difference between the measured value and the averaged value for the near side of the moon, although the magnitude of the radar cross section per unit area measured by Surveyor 7 in the vicinity of the crater Tycho was found to be twice that for the near side of the moon for the same wavelengths (see #5 and #6, Chapter IV).

The close concordance between the results of the measurement of the radar cross section per unit area in the maria regions and the averaged value for the lunar disk indicates but a slight difference between the electromagnetic properties of the material of the surface layer in the maria regions /24
investigated and the averaged electromagnetic properties of the material of the surface layer of the near side of the moon in the 2 and 3 centimeter bands. One reason for the higher value of the measured magnitude of the radar cross section per unit area in the vicinity of the crater Tycho (a young continental region) may be the increased density of the surface layer material in this particular region in terms of the mean density for the near side of the moon.

Measurements of the characteristics of reflection and scattering, made for local regions of the moon by T. W. Thompson and R. B. Dyce [167], and by G. H. Pettengill and T. W. Thompson [156], on 3.8 cm and 70 cm, revealed that certain sections of the surface reradiate in the backward direction with an intensity 3 to 6 times that of the surface around these sections. Sections such as these include the inner slopes of craters, concave floors of craters, and regions of younger lunar formations (the craters Tycho, Copernicus, and others); that is, those regions where the thickness of the ploughed layer apparently is less, but where the density of the surface layer is greater, than in geologically older regions.

CHAPTER II

SURFACE LAYER REFLECTION AND SCATTERING CHARACTERISTICS

1. Reflection and Scattering Characteristics. Terminology.

Scientific and technical literature devoted to investigating the reflection and scattering of radio waves by different surfaces and bodies does not, at present, use standardized terminology and units, and this greatly complicates an understanding of the materials discussed. Hence, the definitions of the terms used in this monograph, and some of their analogies, as they appear in the literature, are given below.

Scattering of radio waves by a surface is secondary radiation of radio waves by the surface layer of a planet in different directions. The frequency of the scattered signal is equal to the frequency of the illuminating signal.

Reflection of radio waves by a surface is secondary radiation of radio waves by the surface layer of a planet in a direction for which the angle of incidence is equal to the aspect angle. The frequency of the echo signal is equal to the frequency of the illuminating signal.

Reradiation of radio waves by a surface is secondary radiation of radio waves during which reflection, as well as scattering, of radio waves occurs. The frequency of the reradiated radio waves is equal to the frequency of the illuminating signal.

Radar cross section, σ, is the factor of proportionality for energy flux power reradiated by the target (by the planet), P_{re}, and the power per unit area in the incident wave, Π_{in}. The magnitude of σ is measured in square meters

$$P_{re} = \sigma \Pi_{in}. \tag{2.1}$$

The reflectivity, σ_0, is the radar cross section of 1 m^2 of the area of an extended observed target (that is, of a target, the angular size of which exceeds the width of the antenna pattern; see Figure 2.1). σ_0 is dimensionless.

If the properties of the reradiating surface do not depend on the location of the scatterer on the surface, /26

$$\sigma_0 = \sigma/S, \tag{2.2}$$

where

S is the magnitude of the illuminated surface.

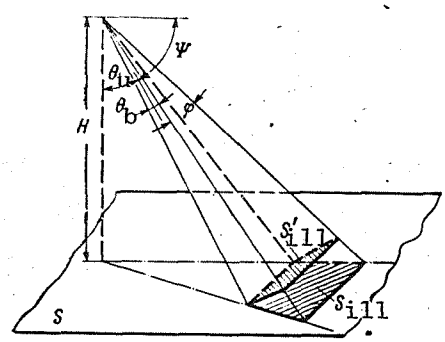

Figure 2.1. Extended observed target.

The reflectivity for broadside incidence is $\sigma_{ON} = \sigma_O(\theta)$ when $\theta = 0$, where θ is the angle of incidence.

The backscattering pattern, $B(\theta)$, is the ratio of reradiated power angular density, reradiated in the back direction at angle θ, to the flux power angular density, reradiated in the back direction for the case of broadside incidence

$$B(\theta) = \frac{p_{re}(\theta)}{p_{re}(0)} \tag{2.3}$$

It is obvious that $B(\theta)$ is dimensionless.

Reflectivity and the backscattering pattern sometimes are expressed in decibels, rather than in dimensionless units, and then $\sigma_0\,[\mathrm{dB}] = 10 \log \sigma_0$, and $B(\theta)\,[\mathrm{dB}] = 10 \log B(\theta)$.

The scattering indicatrix, $i(\theta, \varphi, \Phi)$, is the ratio of the reradiated power angular density to the magnitudes of the angles of incidence, θ, aspect Φ, and difference in the azimuths of incidence and aspect, φ, normalized with respect to its maximum

$$i(\theta, \varphi, \Phi) = \frac{P_{re}(\theta, \varphi, \Phi)}{[P_{re}(\theta, \varphi, \Phi)]_{max}}. \qquad (2.4)$$

The scattering indicatrix obviously is dimensionless, and will be the backscattering pattern when the incidence and aspect on azimuths coincide.

The flat surface albedo (the power reradiation coefficient), A, is the ratio of the power reradiated in all directions to the power incident at this surface /27

$$A = \frac{P_{re}}{P_{in}} \qquad (2.5)$$

The power reflection coefficient (the Fresnel coefficient), ρ_m, is the ratio of the power reradiated in the direction of the specular reflection to the power incident at this surface, provided the illuminated surface is both smooth and flat.

The illustrative albedo (after Sharonov), A_i, is the ratio of the flux power angular density reradiated back from a spherical body to the incident flux power angular density. Conventionally, the spherical body is sited at the planet; that is, it has the same mean radius as the planet under study, and completely scatters all the electromagnetic energy incident at it in accordance with Lambert's law.

The following synonyms of terms used in this book will be found in the literature on the reflection and scattering of radio waves by different surfaces.

Synonyms of "radar cross section" include "effective radiation area," "effective cross section of radar reflection," "effective scattering cross section," and "the cross section." There are many synonyms for the term "backscattering pattern," including "effective scattering area pattern," "reflection function," "reflection characteristic," "backscattering indicatrix," "the scattering law," "the angular scattering law," and "the angular dependence of backscattering."

Found in the literature in place of the term "albedo" are such terms as the "energy coefficient of reflection," "power reflection factor," "reflectivity," and others, and this often results in errors in determining the physical properties of a surface because the albedo and the reflectivity

are different concepts. They are related in different ways to the physical properties of a surface and of a surface layer.

2. Types of Reradiating Surface Layers

Illumination of a planetary surface by electromagnetic energy creates a field in the surface layer which, in turn, creates a flux of electromagnetic energy, part of which is reradiated to the planetary atmosphere. The remainder is absorbed in the surface layer.

The electromagnetic field in the surface layer attenuates with depth, /28
and the degree of that attenuation (the attenuation decrement) depends on the electromagnetic characteristics of the surface layer; on the conductivity σ_c on the permittivity ε, on the permeability μ, and on their change with depth. The electromagnetic characteristics of the surface layer depend on the chemical property, density, and certain other characteristics of the material making up this layer. The above-indicated electromagnetic characteristics also can depend on the wavelength.

The concept of depth of penetration, that is, the depth at which the electromagnetic field is attenuated by a factor of e with respect to the field at the surface, is introduced into the consideration of the electromagnetic field in the surface layer.

The depth of penetration can be found by using the expression [37] that follows when the surface is homogeneous

$$l_e = \frac{\lambda}{2\pi \operatorname{tg} \Delta \sqrt{\varepsilon}} [\text{m}], \tag{2.6}$$

where

Δ is the loss angle;

λ is the wavelength (in meters).

The flux energy incident at the surface in unit time, P_{in}, henceforth will be called the incident power. It is equal to (see Figure 2.2)

$$P_{in} = P_{ab} + P_{re}, \tag{2.7}$$

where

P_{ab} is absorbed power;

P_{re} is reradiated power.

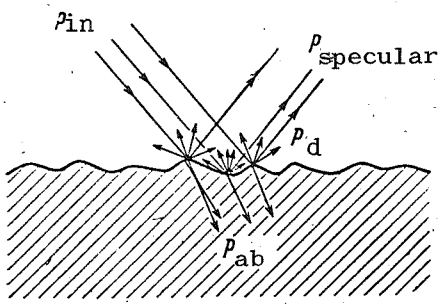

Figure 2.2. Reradiation of electromagnetic energy by the surface layer.

The magnitude of the reradiated power depends on the electromagnetic characteristics of the surface layer, on the nature of the irregularity of the reradiating surface, which is determined by the ratio of the size of the irregularity to the wavelength, and on the angle of incidence.

Many authors simplify the calculations and interpretation of the results by introducing a conventional separation of the power of the reradiated flux into two components. The power near the direction of the specular reflection /29 ($\Phi = -\theta$, $\varphi = 0$) is called the reflected power, P_r, or the quasispecular component of the reradiated power. The remainder of the reradiated flux power is called the scattered power, P_s, or the diffuse component.

Surfaces are classified by degree of unevenness in the optical and r-f regions as follows: smooth, uneven, or rough, and ideally rough. The roughness criteria were developed some time ago for the visible light region, and they were used in the r-f band of the spectrum as well. They are based on a comparison of the size of the roughness and the wavelength.

Smooth Surface

Let us apply the Rayleigh criterion to rough surfaces, for it includes the ratio of the roughness, h, to the wavelength, λ, as well as the angle of incidence θ. According to this criterion the difference in the phases of the two waves reflected from the peak and the valley of the depression must be less than $\pi/4$ to satisfy the reflection condition. The surface therefore will be smooth when

$$h \cos \theta < \lambda/16. \qquad (2.8)$$

A smooth surface can be defined as one with an unbroken structure for which the root-mean-square change in the relief is much less than the wavelength.

A smooth surface is quasispecular-reflecting. The less the height of the irregularity, the greater the reradiated flux power angular density in the direction of the specular reflection ($\Phi = -\theta$, $\varphi = 0$), and the narrower the scattering indicatrix, which has a maximum in the direction of the specular reflection. The surface can be uneven (greater than h), but the reradiation from it when the angle of incidence is large will be much closer to the specular reflection. Smooth surfaces have little back reradiation when the angle of incidence is different from zero.

The return signal strength when the axis of the antennas is tilted 45° to the vertical when flying over the ocean, and as measured by a Doppler speedometer, decreases 40 dB when the ocean is dead calm, for example, when compared with the same signal strength when the sea state is force 1-2.

The reflectivity, σ_0, of an isotropic scattering surface satisfying Eq. (2.8) can be calculated, theoretically, in terms of the angle of incidence, the nature of the irregularity, and the electrical properties of the surface layer [65]. According to this reference, σ_0 is equal to the following, disregarding the shading of part of the surface by irregularities when the angles of incidence are large.

$$\sigma_0 = 8 \cos^3 \theta T \overline{h}^2 k^4 \int_0^\infty \rho(r) I_0(2kr \sin \theta) r dr, \qquad (2.9)$$

/30

where

$k = \frac{2\pi}{\lambda}$ is the wave number;

$\overline{h^2}$ is the root-mean-square of the surface irregularity,

found from

$$\overline{h}^2 = \lim_{L \to \infty} \frac{1}{L^2} \int_{-L/2}^{L/2} \int_{-L/2}^{L/2} f^2(x, y) dx dy. \qquad (2.10)$$

Here f(x, y) is the height of the surface, measured with respect to the mean level at a point with coordinates x, y. $\rho(r)$ is the autocorrelation function for the surface under consideration, and L is the size of the area.

$$\rho(r) = \rho(\sqrt{x^2+y^2}) = \lim \frac{1}{L^2} \int_{-L/2}^{L/2} \int_{-L/2}^{L/2} \frac{f(\xi, \eta) f(\xi + x, \eta + y)}{h^2} d\xi d\eta; \qquad (2.11)$$

and $I_0(X)$ is a Bessel function of zero order.

T includes the ratio of the power reradiated rearward to the polarization of the incident flux and to the electrical properties of the surface layer. T, for horizontal polarization, equals

$$T_h = \left\{ \frac{\varepsilon - 1}{[\cos\theta + (\varepsilon - \sin^2\theta)^{1/2}]^2} \right\}^2. \qquad (2.12)$$

T, for vertical polarization, equals

$$T_v = \left\{ \frac{(\varepsilon - 1)[\varepsilon(1 + \sin^2\theta) - \sin^2\theta]}{[\varepsilon\cos\theta + (\varepsilon - \sin^2\theta)^{1/2}]^2} \right\}^2. \qquad (2.13)$$

The assumption, in the derivation of these coefficients, was that the magnetic permeability, μ, of the surface layer was the same as the permeability of space, $\mu_0 = 1$. If not, Eqs. (2.12) and (2.13) would be much more complicated.

The electromagnetic energy power reflection coefficient when the surface is smooth and flat, and incidence is normal, can be found from [109]

$$\rho_{SN} = \left(\frac{1 - \sqrt{\frac{\mu_a}{\mu}\frac{\varepsilon}{\varepsilon_a}}}{1 + \sqrt{\frac{\mu_a}{\mu}\frac{\varepsilon}{\varepsilon_a}}} \right)^2, \qquad (2.14)$$

where

μ_a is the magnetic permeability of the atmosphere;

μ is the magnetic permeability of the surface layer; /31

$\varepsilon_a = \varepsilon'_a - j2\sigma_a/f_0$ is the complex permittivity of the atmosphere;

$\varepsilon = \varepsilon' - j2\sigma_c/f_0$ is the complex permittivity of the surface layer;

σ_a is the conductivity of the atmosphere;

σ_c is the conductivity of the surface layer;

f_0 is the working frequency.

It has been found that $\mu = \mu_a$ for the majority of the rocks comprising the terrestrial surface layer. But the preliminary estimates make it appear that this is correct for the moon, and for the other planets in the solar system, as well [53]. The reflection coefficient in the case of an illuminating flux incident at a flat, smooth surface will depend on the angle of incidence, as well as on the polarization of that flux. The power reflection coefficient for horizontal polarization is [4]

$$\rho_{sh}(\theta) = \left(\frac{\cos\theta - \sqrt{\varepsilon - \sin^2\theta}}{\cos\theta + \sqrt{\varepsilon - \sin^2\theta}}\right)^2. \tag{2.15}$$

and for vertical polarization it is

$$\rho_{sv}(\theta) = \left(\frac{\varepsilon\cos\theta - \sqrt{\varepsilon - \sin^2\theta}}{\varepsilon\cos\theta + \sqrt{\varepsilon - \sin^2\theta}}\right)^2. \tag{2.16}$$

The derivation of Eqs. (2.15) and (2.16) assumed

$$\mu = \mu_a, \quad \sigma_a = 0.$$

The magnitudes represented by Eqs. (2.14), (2.15), and (2.16) are called the Fresnel coefficients in electrodynamics: R_N, R_h, and R_v.

Accordingly, $\rho_{sN} = R_N^2$; $\rho_h = R_h^2$; and $\rho_v = R_v^2$.

Consideration of the echo phenomenon should keep in mind the fact that in the case of finite distances from the target to the receiver, or transmitter, the whole of the area upon which the flux of electromagnetic energy is incident does not participate in the formation of the echo to the identical degree. The areas closer to the points of specular reflection have a greater influence. Here the interference phenomenon at the point of reception of signals reflected from the different sections of the surface form so-called Fresnel regions, the field intensity in which attenuates with increase in the number of regions.

The dimensions of the semiaxes of Fresnel region ellipses are determined by the expressions

along the x axis
$$a_m = \frac{1}{\cos\theta}\sqrt{\frac{m\pi}{k}\frac{R_1R_2}{R_1+R_2}}, \tag{2.17}$$

along the y axis
$$b_m = \sqrt{\frac{m\pi}{k}\frac{R_1R_2}{R_1+R_2}}. \tag{2.18}$$

Should $R_2 \gg R_1$, or $R_1 \gg R_2$, Eqs. (2.17) and (2.18) will become /32

$$a_m = \frac{1}{\cos\theta}\sqrt{\frac{m\pi}{k}R_{1,2}}, \tag{2.19}$$

$$b_m = \sqrt{\frac{m\pi}{k}R_{1,2}}, \tag{2.20}$$

where

$k = \frac{2\pi}{\lambda}\sqrt{\epsilon}$ is the wave number;

m is the number of Fresnel regions;

$R_{1,2}$ is the least distance between R_1 and R_2 when $R_1 \gg R_2$ or $R_2 \gg R_1$;

R_1 is the distance from the transmitting antenna to the target;

R_2 is the distance from the target to the receiving antenna.

The ratio of the power reflected from the regions containing all Fresnel zones with numbers from 0 to m to the total power reflected from a small area of infinite dimensions can be calculated by using [4]

$$A = \left(1 - \frac{1}{\pi}\sqrt{\frac{2}{m}}\right). \tag{2.21}$$

Eq. (2.21) means that the region delimited by the eight Fresnel zones participates in the formation of 84 percent of the power reflected by a small area with infinite dimensions, and that the region delimited by the first zone participates in the formation of 55 percent of this power.

The power density at the point of reception will be less when reflection is from a smooth spherical surface than it will be when reflection is from a smooth flat surface with the same angle of incidence and the same distances from the point of specular reflection (0) to the receiving and transmitting antennas (points A and B, respectively in Figure 2.3). This brings into play the spherical divergence factor, α, in the case of the smooth spherical surface, indicating the factor by which the "reflection coefficient" for a smooth spherical surface is reduced relative to a smooth flat surface for the same angles of incidence. Accordingly,

$$\rho_s(\theta)_{sp} = \rho_s(\theta)_f \alpha. \tag{2.22}$$

The spherical divergence factor can be found by (see Figure 2.3) [4]

$$\alpha = \frac{(R_1 + R_2)\, a \cos\theta}{R_1 R_2 + a\,(R_1 + R_2)\cos\theta}, \qquad (2.23)$$

where

a is the radius of the sphere.

The spherical divergence factor depends solely on the geometry, and not on the electromagnetic properties of the surface layer. /33

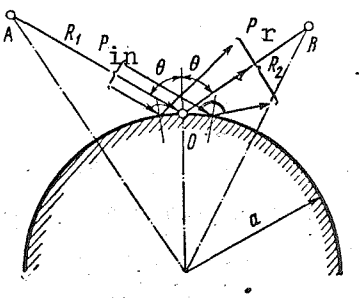

Figure 2.3. Reflection of radio waves from a spherical surface.

The magnitude of the echo signal resulting from the illumination of a smooth sphere by a plane-parallel ray definitely depends on the ratio of sphere radius to wavelength. The relationship between radar cross section and wavelength is proportional to λ^{-4} in the region where the dimensions of the sphere are substantially shorter than the wavelengths (the Rayleigh region). The radar cross section does not depend on the wavelength in the other limiting region where the wavelength is substantially shorter than the radius of the sphere.

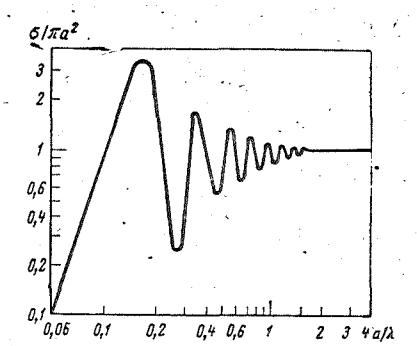

Figure 2.4. Smooth and perfectly conducting sphere radar cross section in terms of the ratio of the sphere diameter to the wavelength.

Figure 2.4 shows the sphere cross section in terms of the ratio of sphere diameter to wavelength for perfect conductivity of its surface layer. A planet usually is found to have a ratio of $a/\lambda \gg 1$, so far as radar is

concerned. The case of $a/\lambda \ll 1$ corresponds to the echoes from such formations as dust, raindrops, fog, hail. So, for the perfectly conducting smooth sphere, when $a/\lambda \gg 1$

$$\sigma_s = \pi a^2. \tag{2.24}$$

If the smooth sphere is not perfectly conducting [109], and this includes one made of a dielectric [153], when $a/\lambda \gg 1$

$$\sigma_s = \rho_{sN} \pi a^2, \tag{2.25}$$

where

ρ_{sN} can be found by using Eq. (2.14).

There is a class of spherical bodies that have a smooth, wavy, surface. /34
These bodies, made of a dielectric, or of a conducting material, have the properties of specular reflection when the sizes of the irregularities, h, and the radii of their curvature, r, are greatly in excess of the wavelength. The magnitude of the echo signal from a sphere such as this exceeds the magnitude of the echo from a perfectly smooth sphere made of the same material, and is a "wavy" sphere with radius a equal to the mean radius of the "wavy sphere."

Hagfors found the value of the cross section for this sphere [121] to be

$$\sigma = g_s \rho_{sN} \pi a^2, \tag{2.26}$$

where

g_s is the factor of directivity for the wavy sphere, equal to

$$g_s = 1 + \alpha^2. \tag{2.27}$$

The value α^2 in Eq. (2.27) is equal to the root-mean-square slope of the "wavy" surface; that is, the root-mean-square angle of inclination of the surface σ_α will be equal to

$$\sigma_\alpha = \arctan \alpha^2 \tag{2.28}$$

Irregular Surfaces

According to accepted classification, all surfaces with irregularities ranging from fractions of a wavelength ($\sim 1/8\ \lambda$) to several wavelengths ($\sim 10\ \lambda$) are included in the class designated as irregular surfaces. The nature of

the echo from these surfaces is quite complex because it depends on the magnitude of the irregularity, as well as on the angles of inclination of the irregularities to the direction of the incident ray.

A good many papers have been devoted to study of this echo. These papers have studied echoes from the following types of irregular surfaces:

1. periodic surfaces, in one, or in two, directions;

2. statistically rough surfaces with one-dimensional distribution in one, or in two, dimensions;

3. statistically rough surfaces with imposition (superposition) of several types of surfaces.

L. M. Brekhovskikh studied surfaces of the first type [14-16], M. L. Antokol'skiy [6], and M. A. Isakovich [27], studied those of the second type, and P. Beckmann [89-93] studied those of the third type.

Theoretical and experimental study of the Moon, Earth, and Venus [93, 107, 114, 139] has revealed that the nature of the return of radio waves by the surface layers of these celestial bodies most nearly resembles that from /35 the surface model built by Beckmann. What Beckmann did was to take a surface $\xi(x, y)$, represented by the set of independent stationary random functions $\xi_1(x, y)$, $\xi_2(x, y)$, ..., taking, respectively, the random values h_1, h_2, ..., h_i, each of which has a normal distribution law with different characteristics. It also was assumed that this set has autocorrelation coefficients $C_i(\tau)$ of the type

$$C_{i_1}(\tau) = \exp\left(-\frac{\tau^2}{T_i^2}\right) \tag{2.29}$$

or

$$C_{i_2}(\tau) = \exp\left(-\frac{|\tau|}{T_i}\right), \tag{2.30}$$

where

T_i is the radius of correlation;

τ is the distance on the surface between two points with coordinates (x, y and x^1, y^1).

A surface with a reradiation factor of one is illuminated at angle θ by a vertically polarized plane wave with a field strength equal to unity. Repeated, mutual reradiation from individual sections of the surface is disregarded. The mean square amplitude of the reradiated field (EE*), measured at some distance, R_2, from the illuminated small area, S, is found for these two types of correlation functions. It equals

1. $$(EE^*)_1 = \frac{2\pi E_0^2}{S} F^2 \frac{1}{\sum_i g_i |C_i''(0)|} \exp\left(-\frac{V_{xy}^2}{2} \sum g_i |C_i''(0)|\right), \qquad (2.31)$$

2. $$(EE^*)_2 = \frac{2\pi E_0^2}{S} F^2 \frac{\sum_i g_i/T_i}{\left(\sum_i g_i/T_i + V_{xy}^2\right)^{3/2}}. \qquad (2.32)$$

Here, and in what follows, the symbol $\sum_i$ will designate summing with respect to i.

It has been assumed for Eqs. (2.31) and (2.32) that the asterisk denotes a complex conjugate magnitude

$$\bar{E}_0 = \frac{2\pi S}{\lambda \pi R_2}, \qquad (2.33)$$

the amplitude of the intensity of the field reradiated by a perfectly smooth, flat surface S, normal incidence, at distance R_2 from this surface

$$F = \frac{1 + \cos\theta\cos\Phi - \sin\theta\sin\Phi\cos\varphi}{\cos\theta + \cos\Phi}. \qquad (2.34)$$

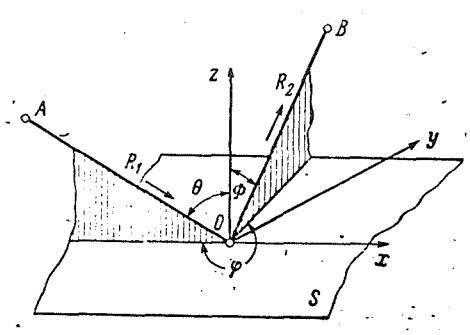

Figure 2.5. Surface illumination diagram. A - radiation source; B - target.

Figure 2.5 is a diagram of the angles of incidence and aspect.

$$V_{xy} = \sqrt{V_x^2 + V_y^2}, \tag{2.35}$$

$$V_x = \frac{2\pi}{\lambda}(\sin\theta - \sin\Phi\cos\varphi), \tag{2.36}$$

$$V_y = \frac{2\pi}{\lambda}(\kappa\sin\Phi\sin\varphi), \tag{2.37}$$

$$V_z = \frac{2\pi}{\lambda}(\cos\theta + \cos\Phi). \tag{2.38}$$

V_x, V_y, V_z are the projections of the radius vector on the coordinate axes, expressed in wave numbers $k = 2\pi/\lambda$;

$$g_i = V_z\sigma_i^2; \tag{2.39}$$

$C_i''(0)$ is the second derivative of the autocorrelation coefficient when $\tau = 0$; σ_i is the root-mean-square deviation (the magnitude of the irregularity) for the function $\xi_i(x, y)$.

$$g_i C_i''(0) = s_i, \tag{2.40}$$

where

s_i is the mean square slope of the function $\xi_i(x, y)$.

We have, for the surface $\xi(x, y)$

$$\sigma^2 = \Sigma\sigma_i^2, \tag{2.41}$$

$$g = \Sigma g_i = V_z^2\Sigma\sigma_i^2 = 4\pi\frac{\sigma^2}{\lambda^2}(\cos\theta + \cos\Phi)^2, \tag{2.42}$$

$$\Sigma g_i|C_i''(0)| = \frac{\sigma^2}{T}, \tag{2.43}$$

$h_i = \frac{\sigma_i}{\lambda}$, $h = \frac{\sigma}{\lambda}$ are the dimensions of the irregularities of surfaces ξ_i, and ξ for the particular wavelength. /37

The root-mean-square slopes of the function ξ_i for autocorrelation coefficients of Eqs. (2.29) and (2.30) are, respectively,

$$s_{i_1} = \frac{\sqrt{2}\,\sigma_i}{T_i}, \tag{2.44}$$

$$s_{i_2} = \frac{\sigma_i}{T_i}. \tag{2.45}$$

Eqs. (2.31) and (2.32) take the following form for the direction of the specular reflection

$$(EE^*)_1 = \frac{E_0^2\lambda}{4\pi S}\frac{1}{\sum\limits_i s_i^2}, \tag{2.46}$$

$$(EE^*)_2 = \frac{E_0^2\lambda^2}{128\pi^3 S\cos^2\theta}\frac{1}{(\sum\limits_i h_i s_i)^2}. \tag{2.47}$$

Eqs. (2.31) and (2.32) take the following form for the backscattering

$$(EE^*)_1 = \frac{E_0^2\lambda}{8\pi S\cos^4\theta}\frac{1}{\sum\limits_i s_i^2}\exp\left(-\frac{\operatorname{tg}^2\theta}{2\sum\limits_i s_i^2}\right), \tag{2.48}$$

$$(EE^*)_2 = \frac{E_0^2\lambda}{128\pi^3 S}\frac{1}{(\sum\limits_i h_i s_i)^2\{\cos^4\theta + [\sin\theta/4\pi(\sum\limits_i h_i s_i)]^2\}^{3/2}}. \tag{2.49}$$

Beckmann, by introducing the dimensionless parameters K and C, derived analytical formulas for the backscattering pattern for the two types of autocorrelation coefficients of Eqs. (2.29) and (2.30) in the form

$$(EE^*)_1 = P_{01}\cos^{-4}\theta\exp(-K^2\operatorname{tg}^2\theta), \tag{2.50}$$

$$(EE^*)_2 = \frac{P_{02}}{(\cos^4\theta + C\sin^2\theta)^{3/2}}, \tag{2.51}$$

where

$$K^2 = \frac{1}{2\sum\limits_i s_i^2}, \tag{2.52}$$

$$C = \frac{1}{(4\pi\sum\limits_i h_i s_i)^2}, \tag{2.53}$$

$$P_{01} = \frac{E_0\lambda^2 K^2}{4\pi\eta S}, \tag{2.54}$$

$$P_{02} = \frac{E_0\lambda^2 C}{8\pi\eta S}. \tag{2.55}$$

Here η is the characteristic impedance of the surface medium; P_{01} and P_{02} are the mean powers of the return for normal wave incidence. /38

Eq. (2.51) was used to calculate the backscattering pattern for the surface of the Moon and Venus. It did not, however, include shading of individual sections by other sections of the surface for large angles of incidence, and this resulted in an increase in the energy reradiated from the edge of the planetary disk. Beckmann, in order to include this phenomenon, introduced the so-called shading function, $S(\theta)$, which, in the case of a surface with a normal irregularity distribution law, has the form [90]

$$S(\theta) = \exp\left[-\frac{1}{4}\operatorname{tg}\theta\operatorname{erfc}(K\operatorname{ctg}\theta)\right], \tag{2.56}$$

where

$$\operatorname{erfc}(x) = 1 - \operatorname{erf}(x) = \frac{2}{\sqrt{\pi}} \int_x^\infty e^{-t^2} dt. \tag{2.57}$$

With this in mind, the expression for the backscattering pattern becomes

$$B(\theta) = \frac{P(\theta)}{P_{02}} = B^*(\theta) S(\theta) \approx \frac{1}{(\cos^4\theta + C\sin^2\theta)^{3/2}} \times \\ \times \exp\left[-\frac{1}{4} \operatorname{tg}\theta \operatorname{erfc}(K \operatorname{ctg}\theta)\right]. \tag{2.58}$$

Eqs. (2.31) and (2.32), describing the scattering indicatrix, Eqs. (2.48) and (2.49), describing the backscattering pattern, and Eqs. (2.46) and (2.47), describing the reradiation in the direction of the specular reflection, show that the magnitudes of the surface irregularity, h, and the root-mean-square slope of the irregularity, s, equated to the wavelength, λ, have a definite effect on the nature of the reradiation.

Beckmann compared [93] experimental backscattering diagrams for the moon at wavelengths of 0.86, 3.6, and 68 cm, and 6 m, and for Venus at wavelengths of 23, 43, and 70 cm with the backscattering patterns obtained using Eq. (2.58), to find that they coincided within ±1 dB for change in the angle of incidence from 0 to 90°. This accuracy is adequate for any practical engineering calculations. Figure 2.6 shows C and K values for different wavelengths applicable to the lunar surface [93], and Figures 2.7, 2.8, and 2.9 show $B^*(\theta)$ and $S(\theta)$ for different C and K values.

The theoretical work done by Isakovich and Beckmann makes it possible to find the value of the root-mean-square slopes of a planetary surface for a specific wavelength.

Of great interest when working a planet with radar is the reradiation /40
of radio waves by an uneven spherical surface with limited conductivity of the surface layer. The calculation for a model of this type is very difficult because there still is no procedure for making the engineering calculation of the energy characteristics of its reradiation. Hence, available experimental data are all that can be used to find the cross section for any celestial body.

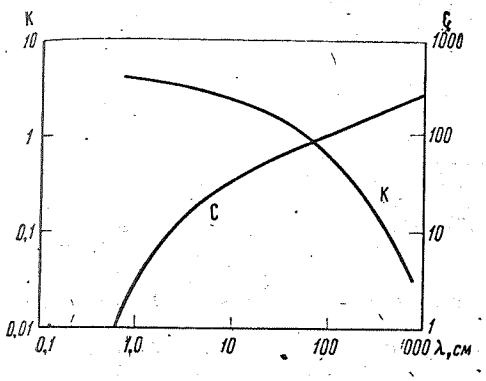

Figure 2.6. K and C, in Beckmann's Eq. (2.58), in terms of the wavelength.

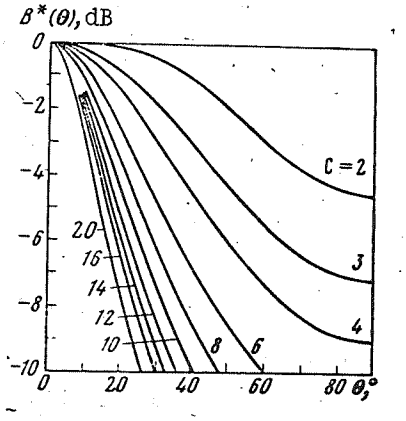

Figure 2.7. Calculated backscattering patterns. Shading for different C values not considered.

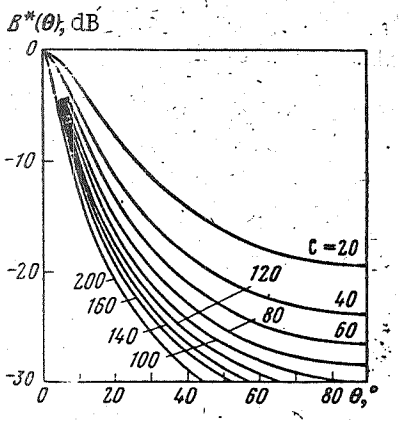

Figure 2.8. Calculated backscattering patterns. Shading for different C values not considered.

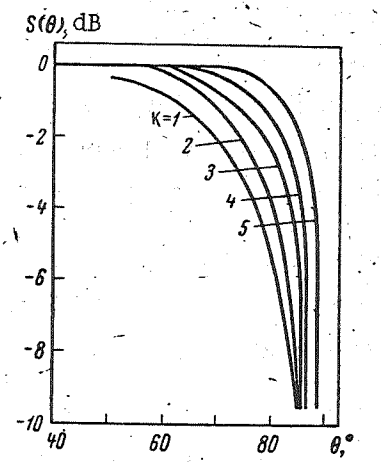

Figure 2.9. The shading function for different K values.

The lunar cross section, or that of a planet, by analogy with the model of a spherical surface, the shape of the surface of which deviates from the perfect sphere in accordance with a random law, can be represented in the form

$$\sigma = g_m \bar{A} \pi a^2, \tag{2.59}$$

where

$\bar{A}$ is the albedo, averaged for all angles of incidence;

g_m is the directivity, indicating the extent to which the ideal planetary cross section differs from the perfectly smooth sphere cross section with the same dimensions and the same energy characteristics of the surface layer, ϵ, σ_s, and μ, as the real planet.

The magnitude g_m also can be determined by the ratio of the intensity of the backward reradiated flux power angular density to the average flux power density reradiated in all directions.

References [107, 109] show g_m equal to [1]

$$g_m = \frac{4\pi \int_0^{\pi/2} \sigma_0(\theta) \sin\theta d\theta}{\int_0^{\pi/2} d\theta \int_0^{\pi/2} d\Phi \int_0^{2\pi} \sigma_0(\theta, \Phi, \varphi) \sin\theta \sin\Phi \, d\varphi}. \tag{2.60}$$

Expressing the reflectivity in terms of its value for normal incidence

$$g_m = \frac{4\pi \int_0^{\pi/2} B(\theta) \sin\theta d\theta}{\int_0^{\pi/2} \int_0^{\pi/2} \int_0^{2\pi} i(\theta, \Phi, \varphi) \sin\theta \sin\Phi \, d\theta \, d\Phi \, d\varphi}. \tag{2.61}$$

The magnitude g_m cannot be obtained directly from radar observations from the earth because these observations do not permit the determination of the scattering indicatrix, $i(\theta, \Phi, \varphi)$ but it can be found by using Eq. (2.59) for known σ and calculated $\bar{A}$. /41

Perfectly Rough Surfaces

The perfectly rough surface, by analogy with optics, is one with a structure, the root-mean-square changes in the irregularities of which are greatly in excess of the wavelength. This surface sometimes is called a frosted surface in optics.

---

1. Eq. (2.60) is correct only when coherence between echoes from different surface elements is lacking. This condition is satisfied for the lunar surface, as reference [107] shows.

Perfectly rough surfaces, as distinguished from smooth surfaces, reradiate electromagnetic energy in all directions, including that of the specular reflection. The return from perfectly rough surface behaves in accordance with the Lambert law, so that, when $\varphi = 0$, the scattering indicatrix has the form [5]

$$i_{\text{L}} = \cos\theta\cos\Phi. \tag{2.62}$$

The backscattering pattern will have the following form for a surface reradiating in accordance with the Lambert law

$$B(\theta)_{\text{L}} = \cos^2\theta. \tag{2.63}$$

The albedo can be found by using the formula

$$A = \frac{P_{\text{re}}}{P_{\text{in}}}. \tag{2.64}$$

Let us determine the magnitudes included in this formula. The total power per unit area in the incident wave will equal

$$P_{\text{in}} = \Pi_{\text{in}}\cos\theta dS. \tag{2.65}$$

when energy with density Π_{in} is incident at a small area at angle θ.

It can be shown that the strength (angular density) of the echo signal can be found by using the formula

$$p_{\text{re}} = A_1 P_{\text{in}}\cos\Phi, \tag{2.66}$$

where A_1 equals

$$A_1 = \frac{\sigma_{0N}}{4\pi}. \tag{2.67}$$

The total echo signal strength can be found by integrating Eq. (2.66) with respect to the hemisphere surrounding the small area dS. After integration and transformations we obtain

/42

$$P_{\text{re}} = \frac{\sigma_{0N}}{4}\Pi_{\text{in}}\cos\theta\, dS. \tag{2.68}$$

The albedo will equal the following when Eqs. (2.65) and (2.68) are taken into consideration

$$A_{\text{L}} = \frac{P_{\text{re}}}{P_{\text{in}}} = \frac{\sigma_{0N}}{4}. \tag{2.69}$$

The magnitude of the albedo does not depend on the angle of incidence when the surface reradiates in accordance with the Lambert law, as we see from Eq. (2.69).

The Lommel-Seelinger law, rather than the Lambert law, is used for practical calculations involving rough surfaces, because the latter is valid only for perfectly rough surfaces. The formula for the scattering indicatrix derived by Lommel and Seelinger is based on the phenomenon of the internal diffusion of light. Their model has it that it is not the surface, but rather the elements of the material of which the surface layer is formed, that are the sources of the reradiated light. It is assumed that each element of the material scatters light uniformly in all directions, and that repeated reradiation of light by neighboring elements does not occur. A model of the scattering of electromagnetic energy such as this can be used in the r-f region in some cases.

The characteristics of reradiation from a surface, as described by the Lommel-Seelinger law, are reviewed in what follows.

The indicatrix of scattering for the surface, when reradiation is in accordance with this law, has the form [5]

$$i_{\text{Л-З}}(\theta, \Phi) = \frac{\cos\theta \cos\Phi}{\cos\theta + a\cos\Phi}, \qquad (2.70)$$

where

$a = k_1/k_2$ is the ratio of the coefficients of attenuation for the reradiated and incident fluxes on the path from the surface to the particles of the reradiating material. Ordinarily, $a = 1$.

Eq. (2.70) was derived for the condition that the different in incident and aspect azimuths is $\varphi = 0$.

If θ is set equal to Φ in Eq. (2.70), we obtain the expression

$$B(\theta) = \cos\theta. \qquad (2.71)$$

for the backscattering pattern for this surface.

Now let us find the albedo when there is a constant flux of electromagnetic energy incident at the surface at angle θ [see Eq. (2.65)]. The echo strength will equal

$$P_{re} = A_2 \Pi_{in} \cos\theta \frac{\cos\Phi}{\cos\theta + a\cos\Phi} dS, \qquad (2.72)$$

where the coefficient A_2 is found from the given equation when $\theta = \Phi = 0$ /43

$$A_2 = \frac{\sigma_{0N}}{4\pi}(1 + a). \qquad (2.73)$$

Total signal strength can be found by integrating Eq. (2.72) with respect to the hemisphere surrounding the small area dS

$$P_{re} = 2\pi A_2 \Pi_{in} \cos\theta\, dS \int \frac{\cos\Phi \sin\Phi}{\cos\theta + a\cos\Phi} d\Phi. \qquad (2.74)$$

After solving for the integral, Eq. (2.74) becomes

$$P_{re} = 2\pi A_2 \Pi_{in} \cos\theta\, dS \left[\frac{1}{a} - \frac{\cos\theta}{a^2} \ln\left(\frac{\cos\theta + a}{\cos\theta}\right)\right]. \qquad (2.75)$$

The albedo thus can be determined from the relationship

$$A_{L\text{-}S} = \frac{\sigma_{0N}}{2}(1 + a)\left[\frac{1}{a} - \frac{\cos\theta}{a^2} \ln\left(\frac{\cos\theta + a}{\cos\theta}\right)\right]. \qquad (2.76)$$

The albedo will equal

$$A_{N\ L\text{-}S} = \frac{\sigma_{0N}}{3.25}. \qquad (2.77)$$

for normal incidence and a = 1.

Let us now consider the case when the planet is illuminated by a parallel flux of electromagnetic energy with uniform density and the receiving antenna pattern has a width exceeding the angular size of the planet. The following process will take place if the angle between the directions of incidence and aspect is changed at this point. The observable hemisphere of the planet will be "illuminated" by the source if these directions coincide (angle $\varphi = 0$, see Figure 2.10). One half of the observed hemisphere of the planet will be illuminated, the other will be in the shadow, when the directions of incidence and aspect are orthogonal (angle $\varphi = 90^\circ$). When $\varphi = 180^\circ$ the whole of the observed hemisphere will be in the shadow. Angle φ (the central angle between the directions of incidence and aspect) is called the phase angle in astronomy.

Consideration of this type of shadowing for the perfectly rough spherical surface reradiating in accordance with the Lambert law, according to reference [5], will yield the following relationship between the magnitude of the echo and the phase angle φ

$$F(\varphi) = \frac{\sin\varphi + (\pi - \varphi)\cos\varphi}{\pi}. \qquad (2.78)$$

The literature refers to this expression as the Schoeneberg function [63].

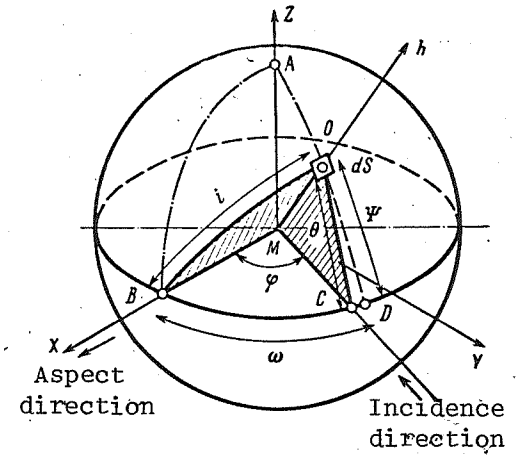

Figure 2.10. Geometry of reradiation from a spherical surface.

/44

The indicatrix of scattering of a spherical surface can be represented in the following form when Eq. (2.78) is included

$$i(\theta, \Phi, \varphi) = \frac{i(\theta, \Phi)}{i(\theta, \Phi)_L} F(\varphi)\cos\theta. \qquad (2.79)$$

The indicatrix of scattering will have the following form when the surface is spherical, subordinate to the Lommel-Seelinger law, and a = 1

$$i(\theta, \Phi, \varphi)_{L\text{-}S} = \frac{\cos\theta}{\cos\theta + \cos\Phi} \frac{\sin\varphi + (\pi - \varphi)\cos\varphi}{\pi}. \qquad (2.80)$$

Eqs. (2.78), (2.79), and (2.80) permit determination of the indicatrix of scattering for a planet for two types of perfectly rough surfaces, at a time when an engineering method for calculating the indicatrix of scattering has not yet been developed for real, existing, rough surfaces of planets.

Hapke [125, 126] made a study of the law of reradiation of light by the near side of the lunar surface and found that the indicatrix of scattering approximates quite well the functions of the type

$$i(\theta, \Phi, \varphi) = \frac{2}{3\pi} \frac{\cos\theta}{\cos\theta + \cos\Phi} \frac{\sin\varphi + (\pi - \varphi)\cos\varphi}{\pi} B(\varphi, q). \qquad (2.81)$$

Note that the indicatrix of scattering for the near side of the moon is the product of three functions: the Lommel-Seelinger law of diffuse scattering, with coefficient a = 1; the Schoeneberg function; and the so-called reproductive function B (φ, q), where q is the packing factor for the moon's upper layer.

The function B (φ, q) helps approximate the narrow peak of the indicatrix of scattering in directions close to the backward. /45

The solution of the Maxwell equations provided the theoretical perfectly rough sphere cross section when $a/\lambda \gg 1$, as well as the perfectly smooth sphere cross section. The results of these solutions for the perfectly rough sphere reradiating in accordance with the Lambert law provided [119]

$$\sigma_L = 2.67\bar{A}\pi a^2, \tag{2.82}$$

where

$\bar{A}$ is the albedo, averaged over the hemisphere.

The magnitude $\bar{A}$ can be found by applying the formula

$$\bar{A} = \int_0^{\pi/2} A(\theta) \sin\theta \, d\theta. \tag{2.83}$$

As will be seen from Eqs. (2.69) and (2.83), $\bar{A}_L = A_L = A_{N\,L}$ for a surface reradiating in accordance with the Lambert law.

The cross section in the case of a sphere reradiating in accordance with the Lommel-Seelinger law is [138]

$$\sigma_{L\text{-}S} = 5.7\bar{A}\pi a^2. \tag{2.84}$$

The mean value of the albedo for angles of incidence $\theta = 0 - 90^\circ$ when reradiation is in accordance with the Lommel-Seelinger law and a = 1 [see Eq. (2.70)], according to Eq. (2.83) and including Eqs. (2.76) and (2.77) equals

$$\bar{A}_{L\text{-}S} = 1.63A_{N\,L\text{-}S} = \frac{\sigma_{0N}}{2}. \tag{2.85}$$

The coefficients 2.67 and 5.7 in Eqs. (2.82) and (2.84) determine the "directivity" of the echo from the sphere relative to the isotropic reradiation.

This coefficient has a number of designations in the literature: d, g, q.

We shall adopt g for the designation of this coefficient, whereupon we obtain a general formula for the sphere cross section in the form

$$\sigma = g\bar{A}\pi a^2. \qquad (2.86)$$

In the case of a sphere reradiating in accordance with the Lambert law, g = 2.67, and $\bar{A} = A$. For a sphere reradiating in accordance with the Lommel-Seelinger law, g = 5.7 and $\bar{A}_{L\text{-}S} = 1.63A_{N\ L\text{-}S}$. Note that the magnitude of g depends on the roughness of the surface.

The set of formulas used in this section thus will enable us to calculate all of the principal characteristics of the reradiation from a perfectly rough surface.

3. Energy Characteristics of Radio Links Using the Surface of a Planet as One of Their Elements

/46

All radio engineering systems and instruments, including those operating near the surface of a planet, can be broken down into three groups: instruments using active radar principles; instruments using semiactive radar principles; and direct data transmission systems.

Systems and instruments using active radar principles have the receiver and transmitter located at the same point in space. The equipment utilizes the echo from the surface of the planet for its operation. These instruments include height-finding radars, surface search radars, Doppler radar flight speed meters, and a host of other devices.

Systems and instruments using semiactive radar principles have the receiver and transmitter located at different points in space.

An echo from the surface of the planet is required for the operation of the radio links. Semiactive homing systems, bistatic radars, and other devices are included in this group.

The third group of systems and instruments have the receiver and transmitter located at different points in space, with direct radio communication between them. The echo from the surface of the planet, passing through the receivers in these installations, is noise.

These installations include the different systems used for exercising radio control and for transmitting data, including radio links for transmitting

commands, those for transmitting telemetry data, television and phototelevision information, radars with active response, radio systems for outer trajectory measurements, and others. These types of systems can be called information radio links.

One of the most important characteristics of any radio link is the signal/noise (S/N) ratio. Space noise and set noise are the main types of noise in the first and second types of systems.

The magnitude of the S/N ratio determines such characteristics of the electronic installations as the discernibility of the signal from the target in the case of operator-manned radars, the probability of undistorted transmission of information over command radio links, and over links transmitting telemetry data, the maximum number of gradations of brightness that can be transmitted over a television channel, errors in measuring altitude by height-finding radars, and others.

Radar formulas are used to calculate the S/N ratio realizable on a radio link [25]. The coefficients contained in these formulas will differ for each concrete instrument because they depend on the characteristics of the modulation, transmission, and processing of the signal on the link. /47

The real S/N ratio on a link, naturally, depends on the true transceiver parameters, determined by the power of the link, as well as on conditions for the propagation of radio waves over the path, and on the real characteristics of the reradiation of radio waves from the planet's surface layer.

Radar theory and practice customarily consider two basic types of targets: point, and distributed. Point targets are broken down into single and group, distributed into volume-distributed and surface-distributed. The latter often are referred to as extended targets. This classification can be narrowed down, so far as planetary study is concerned.

Ordinarily, the surface of a planet can be considered a point target, or an extended (surface-distributed) target. A planet is said to be a point target when its angular size, that is, the angles at which it is seen from the point of observation. There also is the intermediate case, when the planet's angular size compares with the antenna beam width.

The range formulas for each type of system, and the characteristics of reradiation from the surface layer of a planet needed to calculate the energy characteristics of the corresponding radio link, follow.

Active Radar

The following formula [25] will provide the signal-to-noise power ratio for a "point target" in the case of the active radar

$$m = \frac{P_s}{P_n} = \frac{P_t G_t(\alpha) G_r(\alpha) \lambda^2 \eta_p \eta_{tr} \sigma(\theta)}{(4\pi)^3 R^4 k T N \Delta f}, \qquad (2.87)$$

where

P_t is the power radiated by the transmitter, including losses in the transmitting antenna-feeder path, in watts;

$G_t(\alpha) = D_t(\alpha)\eta_t$ is the transmitting antenna gain in the direction to the illuminated surface;

$G_r(\alpha) = D_r(\alpha)\eta_r$ is the receiving antenna gain in the direction to the illuminated surface;

$D_r(\alpha)$, $D_t(\alpha)$ are the respective antenna directivities in the direction to the illuminated surface;

α is the angle between the direction to the illuminated surface and the direction of maximum antenna radiation; /48

η_t and η_r are the respective antenna efficiencies;

η_p is line loss resulting from change in polarization of the incoming signal with respect to that of the radiated power;

η_{tr} is signal attenuation during propagation from the transmitting antenna to the surface and from the surface to the receiving antenna;

k is the Boltzmann constant;

T is the absolute temperature;

N is the equivalent input noise level;

Δf is the receiver bandwidth, in Hz.

The range formula, as will be seen, includes the surface cross section, which determines the reradiating properties of the surface in the direction to the receiving antenna. The magnitude $\sigma(\theta)$ is a generalized parameter of the reradiation from the surface and, as will be pointed out in what follows, depends on surface, and surface layer, properties, as well as on certain installation parameters.

If the angular size of the illuminated surface is considerably smaller than the antenna system beamwidth,[2] the cross section will not depend on the shape of the beam generated by the installation. In this case, the electromagnetic energy illuminating the surface of the planet will be constant in magnitude.

Primarily energy reradiated in a direction opposite to that of the incidence arrives at the receiver input in the case of active radar, and this direction has been designated the "back" direction.

The surface cross section can be represented in the following form for purposes of evaluating the relationship between the backward reradiated power and the angle of incidence

$$\sigma(\theta) = \sigma_N B(\theta), \tag{2.88}$$

where

σ_N is the surface cross section for normal incidence;

$B(\theta)$ is the backscattering pattern for the whole of the illuminated surface;

$\sigma(\theta)$ is the surface cross section for angle of incidence θ.

The shape of the radar antenna pattern must be taken into consideration when calculating the S/N ratio when the planet is illuminated by a radar with a broad beam pattern compared with the angular size of the illuminated surface. It can be shown that in this case Eq. (2.87) becomes

/49

$$m = \frac{P_s}{P_n} = \frac{P_t G_{t\,max} G_{r\,max} \lambda^2 \eta_p \eta_{tr}}{(4\pi)^3 R^4 k T N \Delta f} \times \\ \times \sigma_N \int_{-\frac{\theta_p}{2}}^{\frac{\theta_p}{2}} F_1(\alpha) F_2(\alpha) B(\theta) 2\pi \sin\theta \, d\theta, \tag{2.89}$$

where

θ_p is the angular diameter of the planet

$F_1(\alpha)$, $F_2(\alpha)$ are the normalized receiving and transmitting antenna power patterns;

$G_{t\,max}$, $G_{r\,max}$ are gains, equated to the direction of maximum radiation.

2. Here, and in what follows, the radar installation antenna system beanwidth, or pattern, will be understood to be the product of receiving and transmitting antenna beamwidths, if not otherwise stipulated.

In the case of the surface-distributed target, it is more convenient to express the reradiating properties of the surface in terms of the cross section per unit area intercepted by the radar beam

$$\sigma(\theta) = S\sigma_0(\theta). \tag{2.90}$$

The introduction of $\sigma_0(\theta)$ takes into consideration the scattering properties of the surface, regardless of the beam shape of a specific radar. The magnitude $\sigma_0(\theta)$ therefore becomes a universal characteristic of backscattering for the specified wavelength and angle of incidence.

The backscattering pattern per unit area, $B_0(\theta)$, is introduced for purposes of evaluating the reradiated power in terms of the unit area in the back direction, and makes it possible to represent the cross section per unit by analogy with the radar cross section in the form

$$\sigma_0(\theta) = B_0(\theta)\,\sigma_{0N}. \tag{2.91}$$

The calculation of the S/N ratio for an extended target must be made using Eq. (2.87), with Eqs. (2.90) and (2.91) taken into account.

Because the reradiating surface usually is not isotropic, the backscattering patterns, $B(\theta)$, for the entire surface, and $B_0(\theta)$ for unit surface, will not coincide. Consequently, the following characteristics of the reradiation from the surface layer must be available in order to calculate the radar energy parameters in the case of the active radar:

1. the planetary surface radar cross section, σ;
2. the planetary surface backscattering pattern, $B(\theta)$;
3. the radar cross section per unit area intercepted by the antenna beam at normal incidence $\sigma_{0\,N}$;
4. the backscattering pattern for a unit area, $B_0(\theta)$.

When the planet is a point target, the first characteristic is used for energy potential calculations, the third and fourth are used when the target is extended, and the first and second are used when the case is intermediate. /50

Semiactive Radar

The semiactive radar differs from the active in that the incidence direction of the beam illuminating the surface, and the direction from which the

echo is received (the aspect direction) do not coincide because the receiver and transmitter are located at different points in space.

The foreign literature refers to this method of radar detection for planetary study as bistatic radar. By definition, the radar cross section of the surface is the ratio of the power reflected toward the source to the incident power density. Accordingly, in the case of the semiactive radar, the range formula retains the form for the active radar, but the absolute magnitude of the radar cross section will be different because of the different aspect directions.

The radar cross section of the surface is in the form

$$\sigma(\theta, \Phi, \varphi) = \sigma_N i(\theta, \Phi, \varphi). \tag{2.92}$$

for purposes of evaluating the power reflected toward the source in terms of the incidence and aspect angles.

It can be shown that by including Eq. (2.92) the basic radar equation, Eq. (2.87), will take the form as follows for a "point target"

$$m = \frac{P_s}{P_n} = \frac{P_t G_t(\theta, \varphi) G_t(\Phi, \varphi) \lambda^2 \eta_p \eta_{tr}}{(4\pi)^3 R_1^2 R_2^2 kTN\Delta f} \sigma_N i(\theta, \Phi, \varphi). \tag{2.93}$$

The energy characteristics of the radar must be taken into consideration in terms of the characteristics of reradiation from an extended (surface-distributed) target for an area of unit size.

In this case

$$\sigma(\theta, \Phi, \varphi) = S\sigma_0(\theta, \Phi, \varphi), \tag{2.94}$$

$$\sigma_0(\theta, \Phi, \varphi) = \sigma_{0N} i_1(\theta, \Phi, \varphi), \tag{2.95}$$

where

$i_1(\theta, \Phi, \varphi)$ is the indicatrix of scattering for an area of unit size.

Accordingly, in the case of the semiactive radar, the energy characteristics of the communication link are determined by the following characteristics of the reradiation from the planet's surface layer: σ, $i(\theta, \Phi, \varphi)$, σ_{oN} and $i_1(\theta, \Phi, \varphi)$.

A special case of passive radar is the reception of echoes in the specular reflection direction ($\varphi = 0$, $\Phi = -\theta$). The formulas used to calculate the /51

Fresnel coefficients, Eqs. (2.15) and (2.16), are used in the case of a smooth surface to determine the magnitude of the power reflected toward the source.

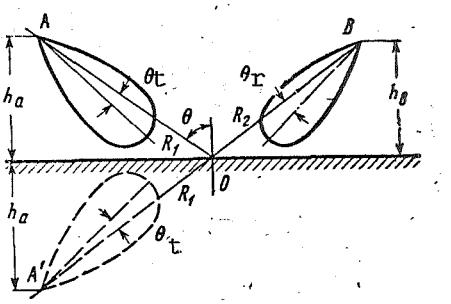

Figure 2.11. Reflection diagram.

If we use the approach taken in optics, that of replacing the real source by its mirror image (points A and A' in Figure 2.11), we see that in the case of specular reflection the case of the semiactive radar can, for a smooth surface, be reduced to the diagram of a radio link, the receiver and transmitter of which are at a distance equal to $R_1 + R_2$. But additional losses in the transmission line, determined by the magnitude of the reflection coefficient, ρ_s, must be included. Then the reradiated power density in the direction of the specular reflection on a smooth surface will be

$$\Pi_{re} = \rho_s \Pi_{in}. \tag{2.96}$$

Thus, Eq. (2.93) for the case of specular reflection will be in the form

$$m = \frac{P_s}{P_n} = \frac{P_t G_t(\theta_t) G_r(\theta_r) \lambda^2 \eta_p \eta_{tr}}{(4\pi)^2 (R_1 + R_2)^2 k T N \Delta f} \rho_s(\theta). \tag{2.97}$$

Information Radio Link

Operation of the information radio link results in a signal reradiated by the planet's surface layer appearing at the receiver input along with the direct signal. The reradiated signal distorts the direct signal because information, "shifted" with respect to time, is applied to the receiver input from the direct and reradiated directions at any particular time. The degree of distortion of the transmitted information is determined by the relationship between the two signal strengths at the input. Let us consider the strengths of these signals individually.

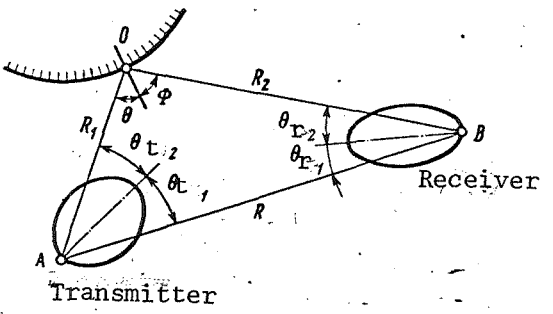

Figure 2.12. Information radio link diagram.

The strength of the direct signal at the receiver input is

$$P_r = \frac{P_t G_t(\theta_{t_1}) G_r(\theta_{r_1}) \lambda^2 \eta_{p_1} \eta_{tr_1}}{(4\pi)^2 R_{tar}^2} \qquad (2.98)$$

Figure 2.12 is the diagram of the radio link, and shows the angle designations.

The strength of the reradiated signal at the receiver input is

$$P_{re} = \frac{P_t \lambda^2 \eta_{p_2} \eta_{tr_2} \sigma_N}{(4\pi)^3} \int_{\theta} \frac{G_t(\theta_t) G_r(\theta_r)}{R_1^2 R_2^2} i(\theta, \Phi)\, d\theta. \qquad (2.99)$$

Eq. (2.99) can be simplified in the case of specular reflection and will be in the form

$$P_s = \frac{P_t G_t(\theta_{t_2}) G_r(\theta_{r_2}) \lambda^2 \eta_{p_2} \eta_{tr_2} \rho_s}{(4\pi)^2 (R_1 + R_2)^2}. \qquad (2.100)$$

The direct and reradiated signal strength ratio follows. This expression is the S/N ratio of the reradiated signal to set noise is large enough

$$\frac{P_d}{P_{re}} = \frac{G_t(\theta_{t_1}) G_r(\theta_{r_1}) 4\pi}{R_{tar}^2 \sigma_N \int_{\theta} \frac{G_t(\theta_t) G_r(\theta_r)}{R_1^2 R_2^2} i(\theta, \Phi)\, d\theta} \frac{\eta_{p_1}}{\eta_{p_2}} \frac{\eta_{tr_1}}{\eta_{tr_2}} \qquad (2.101)$$

Eq. (2.101) will have the following form for the specular reflection case

$$\frac{P_d}{P_s} = \frac{G_t(\theta_{t_1})}{G_t(\theta_{t_2})} \frac{G_r(\theta_{r_1})}{G_r(\theta_{r_2})} \left(\frac{R_1 + R_2}{R_{tar}}\right)^2 \frac{1}{\rho_s} \frac{\eta_{p_1}}{\eta_{p_2}} \frac{\eta_{tr_1}}{\eta_{tr_2}} \qquad (2.102)$$

If the receiver, or the transmitter, in the radio link is moved, the Doppler shift in the spectra must be taken into consideration in the calculation of the ratio of the direct to reradiated signal strengths. This change will differ for the direct and reradiated signals because of the different angles between the direction of the speed vector for the moving part of the radio link and the direction of propagation of the corresponding signal. In this case, Eqs. (2.101) and (2.102) become much more complex because of the distortion in the signal spectra in the receiving path as a result of the nonuniformity in its amplitude-frequency curve. /53

4. Interrelationship of Reradiation Characteristics

The calculation of the energy parameters of a communication link, instrument-surface-instrument, requires the use of different surface reradiation characteristics, depending on the relationship between the angular size of the target and the radar antenna beamwidth. Too, the measured echo characteristics often are inadequate for making the necessary calculations at the specified wavelength. This gives rise to the need to find simple relationships for converting one echo characteristic into another. Let us consider some of them.

The Relationship Between the Radar Cross Section per Unit Area for Normal Incidence, $\sigma_{0\,N}$, and the Radar Cross Section per Unit Area Intercepted by the Antenna Beam, σ_0

The backscattering diagram can be determined from a relationship of the type

$$B(\theta) = p_{re}(\theta)/p_{re}(0). \tag{2.103}$$

Since, by definition, the radar cross section of the isotropic equivalent is equal to

$$\sigma = P_{re}/\Pi_{in} \tag{2.104}$$

and the reradiated power is equal to

$$p_{re} = P_{re}/4\pi, \tag{2.105}$$

using these expressions, Eq. (2.103) becomes

$$B(\theta) = \sigma(\theta)\,\Pi_{in}(\theta)/\sigma(0)\,\Pi_{in}(0). \tag{2.106}$$

The incident flux has a uniform density, so the power density incident at a small area does not depend on the angle of incidence

$$\Pi_{in}(\theta) = \Pi_{in}(0) = \text{const.} \tag{2.107}$$

Including this expression, Eq. (2.106) becomes

$$B(\theta) = \sigma(\theta)/\sigma(0). \tag{2.108}$$

Converting from the total reradiation area to one square meter of area, we have /54

$$B_0(\theta) = \sigma_0(\theta)/\sigma_0(0); \tag{2.109}$$

Considering that $\sigma_0(0) = \sigma_{0N}$,

$$B_0(\theta) = \sigma_0(\theta)/\sigma_{0N}. \tag{2.110}$$

Radar Cross Section of a Sphere and its Radar Cross Section per Unit Area

When a sphere is illuminated by a plane-parallel wave, the conditions under which reradiation from different points on its surface take place will differ. But if the sphere's surface properties are similar at all points, there will be that set of geometric points on its surface, reradiation conditions in the back direction for which, will be identical. This condition will be met by spherical ring surfaces infinitely small in width, for which the angle of incidence of the flux will be constant. The width of a ring such as this (see Figure 2.13) will equal

$$S_{ring} = 2\pi a \sin\theta d\theta. \tag{2.111}$$

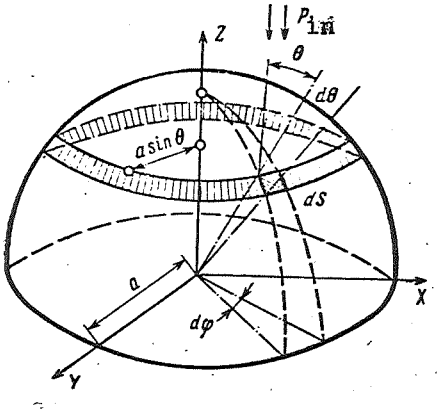

Figure 2.13. Coordinate system.

The radar cross section of this ring can be given from Eq. (2.2) as

$$\sigma_{\text{ring}} = \sigma_0 S_{\text{ring}}. \tag{2.112}$$

The radar cross section of the surface will equal the sum of the radar cross section of the individual parts when repeated mutual reradiation from one surface to another does not occur, and when coherency between signals reradiated by the different surface elements is lacking. Now [see the footnote to Eq. (2.60)] /55

$$\sigma = \sum_S \sigma_{\text{ring}} \tag{2.113}$$

Replacing the surface sum by integration with respect to the angle of incidence, θ, we obtain

$$\sigma = 2\pi a^2 \int_0^{\pi/2} \sigma_0 \sin\theta d\theta. \tag{2.114}$$

Using Eq. (2.110), we obtain

$$\sigma = 2\pi a^2 \sigma_{0N} \int_0^{\pi/2} B(\theta) \sin\theta \, d\theta. \tag{2.115}$$

Recognizing that

$$S_{\text{disk}} = \pi a^2, \tag{2.116}$$

Eq. (2.115) will take the form

$$\sigma = 2S_{\text{disk}} \sigma_{0N} \int_0^{\pi/2} B(\theta) \sin\theta \, d\theta. \tag{2.117}$$

Albedo and Indicatrix of Scattering

When the wave is normal to the surface ($\theta = 0$), the maximum for the reradiated signal strength will coincide with the strength in a direction normal to the surface

$$p_{\text{re}}(\Phi)_{\max} = p_{\text{re}}(0). \tag{2.118}$$

Assuming that the indicatrix of scattering is symmetrical with respect to the axis coinciding with the normal to the surface, we obtain

$$i(\theta, \Phi, \varphi) = i(\Phi). \tag{2.119}$$

The radar cross section of small area ΔS for the case of normal incidence will be in the form

$$\sigma_{\Delta S} = \frac{P_{re}(\theta)}{\Pi_{in}(\theta)_{when\ \theta=0}} = \frac{P_{re}(\theta)\,\Delta S}{P_{in}(0)} \quad \text{when } \theta=0 \tag{2.120}$$

The radar cross section per unit area therefore will equal

$$\sigma_0 = \sigma_{\Delta S}/\Delta S = P_{re}(\theta)/P_{in}(0). \tag{2.121}$$

According to Eq. (2.103), the reradiated signal strength for normal incidence will equal

$$p_{re}(0) = P_{re}(0)/4\pi. \tag{2.122}$$

/56

Limiting the upper half-plane, which includes the area ΔS, the hemisphere S, and the radius r, let us calculate the magnitude of the power reradiated from surface S passing through the hemisphere

$$P_{re\ \Sigma} = \int_S p_{re}(\Phi, \varphi)\, dS, \tag{2.123}$$

where Σ is the sum in all directions within the limits of the upper hemisphere.

Replacing integration with respect to the surface by integration with respect to angles Φ and φ, and performing the necessary transformations, we obtain

$$P_{re\ \Sigma} = \int_{\varphi=0}^{2\pi}\int_{\Phi=0}^{\pi/2} p_{re}(0)\, i(\Phi)\sin\Phi\, d\Phi\, d\varphi = \\ = 2\pi p_{re}(0)\int_0^{\pi/2} i(\Phi)\sin\Phi d\Phi. \tag{2.124}$$

The albedo, therefore, will equal

$$A_N = \frac{P_{re\ \Sigma}}{P_{in}} = \frac{2\pi p_{re}(0)\int_0^{\pi/2} i(\Phi)\sin\Phi\, d\Phi}{P_{in}} \tag{2.125}$$

for the normal incidence case.

Substituting the value $p_{re}(0)$ from Eq. (2.122) into Eq. (2.125), including Eq. (2.121), and making the necessary cancellations, we obtain the expression for the albedo used in the calculations

$$A_N = \frac{\sigma_{0N}}{2}\int_0^{\pi/2} i(\Phi)\sin\Phi\, d\Phi. \tag{2.126}$$

The albedo can be determined by the above procedure for an arbitrary direction of incidence ($\theta \neq 0$) and for the condition that the indicatrix of scattering does not depend on the azimuth angle φ.

Completing the calculations

$$A(\theta) = \frac{\dot{\sigma}_{0N}}{2\cos\theta} \int_0^{\pi/2} i(\theta, \Phi) \sin\Phi \, d\Phi, \qquad (2.127)$$

where $i(\theta,\Phi) \approx i(\Phi)/B(\theta)$. This formula makes it possible to find the albedo for a known indicatrix of scattering.

CHAPTER III

/57

METHODS FOR DETERMINING RERADIATION CHARACTERISTICS

1. Comparative Evaluation of the Use of Radio Methods to Locate the Moon and the Planets from the Earth and from Spacecraft

All active radio engineering methods for investigating the characteristics of reradiation from planets now in use, and proposed use in the future, can be broken down into three groups.

The first group uses a measuring complex comprising ground receivers and transmitters. This complex is called a "planetary radar."

The second group for radiating, receiving, and processing signals uses radio engineering equipment installed on board spacecraft operating near the surface of the planet under study. The spacecraft performs primary processing of echoes from the planet's surface layer. Telemetry information on transmitter parameters, the results of primary processing of the echo, and data on the position of the spacecraft relative to the surface under study, are transmitted to the ground station.

The third group used on-board, as well as ground, radio engineering equipment. The transmitter usually is installed in the spacecraft, but the receiver and the echo processing equipment are installed in the ground station.

The first group has definite, inherent, shortcomings, the result of the long distances, in the millions of kilometers, to the target.

1. The transceiver system must have a tremendous energy potential if the required dependability of measurements is to be obtained. This requires building powerful transmitters, huge, unique, antenna systems, cooled parametric amplifiers, and a complicated data processing system, capable of separating the useful signal with the required degree of dependability when the S/N ratio at its input is low. Table 3.1 lists some of the characteristics of the planets in the solar system, and some of the excess radar energy /58
potentials needed to study these planets, as compared with the potential required for a radar designed for studying the moon. It is understood that the

characteristics of the echoes from the planets are similar to those from the moon, and that the same S/N ratio is maintained during the study of all the planets.

TABLE 3.1

Planets	Minimum distance from earth, 10^6 km	Radius of planet 10^3 km	Maximum angular diameter of planet from earth, seconds of arc	Necessary excess potential as compared with moon, dB
Mercury	80	2.5	12.9	89
Venus	40	6.051	63.8	59
Moon	0.356	1.738	2020	0
Mars	56	3.39	25.2	80
Jupiter	600	71.4	48.8	92
Saturn	1270	60.3	19.6	109
Uranus	3100	24.8	3.6	133
Neptune	4300	24.5	2.1	139.5
Pluto	5700	< 2.9	0.24	155.5

2. Study of the echoing properties of small, local, areas on the surface of a planet is difficult when ground radar is used. This is so because it is impossible to design antenna systems with a sufficiently narrow beam, calculated in fractions of a second of arc, in the radio frequency range. Most of the radar measurements made of the moon to date have averaged reradiation characteristics for the whole of the near side of the lunar surface in order to determine those characteristics. As a result, the measurement of characteristics and properties of specific local regions of the surfaces of the moon, and of planets, is indeed necessary, for doing so will aid in ensuring reliable landing of automatic, and manned, spacecraft on these planets. Recent radar study of the moon by powerful planetary radars has made it possible to determine the characteristics of the reradiation from certain local areas, and to construct radar charts of these regions.

3. It is obvious that these methods do not determine the characteristics of the reradiation on the far side of the lunar surface, an area comprising 41 percent of the total lunar surface.

4. The indicatrix of scattering, a highly important parameter in the operation of a radio link for transmitting data from the earth to an artificial planetary satellite and back, cannot be measured. /59

5. Difficulties in determining the dimensions of the echoing area near the limb make the reliability of the measurements made at the edge of the disk low, compared with those made at the center of the lunar disk.

6. The terrestrial atmosphere and the ionosphere restrict the measurements of echo characteristics by radar to a limited band of wavelengths (~ 1 cm to 20 meters).

Launching an artificial earth satellite with a known radar cross section (a sphere with a diameter of 1 m, for example), into circumterrestrial space at an altitude of more than 1,000 km can solve the problem of calibrating the radar, and determine losses in the terrestrial atmosphere for its operating frequency. However, substantial increase in losses in the terrestrial atmosphere in the millimeter and submillimeter bands means the energy potential of the planetary radar must be increased. Table 3.2 lists the principal characteristics of the largest of the foreign ground radar systems used for radar study of the moon and the planets.

Despite the above-indicated shortcomings of ground radar methods, they do have definite advantages as compared with the methods employed when the radar is installed in spacecraft.

Radar investigations of the lunar surface from the ground can last longer, and the measurements can be more accurate, than those made from circumlunar space because of the large weight and power of the ground stations as compared with those installed in spacecraft, as well as because of better knowledge of current space characteristics of the antenna systems (of the actual patterns and their orientation in space).

Further, measurement of the characteristics of reradiation from the moon, and from the planets, from spacecraft near these planets must solve many significant problems, despite the many advantages this approach has over radar investigation from the earth.

For example, the on-board antenna beams must be quite narrow, and the systems for orienting the antennas with respect to the surface of the planet

must be complex, in order to provide the necessary planetary surface resolution. Broader beams, while simplifying the spacecraft's orientation system, make for poorer resolution, but it still is necessary to determine the instantaneous position of the spacecraft in a planetocentric system of coordinates with the necessary accuracy. The required accuracy is associated with the permissible error in the measurements, beamwidth of the on-board antennas, and the rate of change in the angular position of the spacecraft relative to the surface of the planet.

The limitations on measuring the characteristics of reradiation from a planet's surface from its near space are the time the spacecraft will be active, the capacity of the channel used to transmit data from the spacecraft to earth, and the complexity of building small, light, devices for compressing and converting the data obtained by the spacecraft into a form convenient for radioing to earth. /62

Radar has been used to investigate the moon from the earth for over 20 years, but spacecraft-borne electronic equipment for investigating the characteristics of lunar reradiation is relatively new, and still not perfected. Nevertheless, the results are highly important. Measurements have been made by a number of Soviet spacecraft in the Luna series, as well as by American spacecraft in the Surveyor series, by Lunar Orbiter 1, and by Explorer 35.

There is no doubt that as investigation of the moon, and of the planets in the solar system, continues, methods for measuring the characteristics of reradiation in the r-f band from planets will be perfected, and that the number of experiments carried out will increase.

2. The Use of Pulse-Modulated Radar from the Earth

When the surface of a planet is illuminated by a short pulse, the echo will exist for the time required to propagate to the limb of the planet. The first echo will appear from the point on the planetary surface closest to the ground station, from the "subradar point," or from the "tip" of the planet. The final echo will arrive from scatterers on the limb of the planet. The width of the echo pulse (the radar extent of the planet) is

$$t_p = 2a/c, \quad (3.1)$$

TABLE 3.2

	Observatory	Belonging to	Location	Operating Mode	P_{pulse}, 10^6
1.	Arecibo Ionospheric Observatory (AIO)	Cornell University, USA	Arecibo, Puerto Rico	CW pulse pulse	- 2.5 2.5
2.	Jet Propulsion Laboratory Observatory (JPL)	California Institute of Technology, USA	Goldstone, California, USA	CW pulse CW	- 1 -
3.	Millstone Hill	Lincoln Laboratory, Massachusetts Institute of Technology (MIT), USA	Westford, Massachusetts, USA	pulse pulse	5 2.5
4.	Westford Hill	same	same	CW	-
5.	Haystack Hill	same	same	CW	-
6.	El Campo	same	El Campo, Texas, USA	CW	-
7.	Yakamarka	Boulder Laboratory of the National Bureau of Standards (NBS), USA	Lima, Peru	pulse	5
8.	Stanford Radioastronomy Institute	Stanford University, USA	Palo Alto, California, USA	CW CW CW	- - -
9.	Jodrell Bank	University of Manchester, England	Macclesfield, Cheshire County, England	CW pulse	- 10^{-2}
10.	Royal Radar Establishment	Royal Radar Research Administration	Malvern, England	pulse	2.0
11.	Maryland Point Observatory	Naval Research Laboratory (NRL), USA	Riverside, Maryland, USA	CW	-
12.	-	same	Washington, DC, USA	pulse	2.0
13.	Spooncast Observatory	Lincoln Laboratory, Massachusetts Institute of Technology (MIT), USA	New England, Canada [sic]	pulse	$20 \cdot 10^{-6}$
14.	First radio investigation of the moon		Hungary	pulse	$3 \cdot 10^{-3}$

TABLE 3.2 (cont)

	$P_{m,\ max}$, 10^3 W	A_{eff}, m^2	τ_{pulse}, μsec	$T_{n\Sigma}$, °K	λ, cm	Antennas, Dimension, m	Coverage
1.	150	$36 \cdot 10^3$	-	200	69.8	Spherical, 305	$\theta = 20°$
	150	$36 \cdot 10^3$	0.1-4	200	69.8		$\varphi = 360°$
	100	$25.4 \cdot 10^3$	0.1-2.5	-	750		
2.	100	$1.6 \cdot 10^3$	-	27	12.5	Parabolic, 64	360°
	100	260	1.4	35	12.5	Parabolic, 26	360°
	100	330	-	30	12.5	Parabolic, 29.5	360°
3.	120	260	0.01-4	100	23	Parabolic, 25.6	360°
	120	250	0.002-0.5	100	68		
4.	40	140	-	69	3.6	Parabolic, 18	360°
5.	100	550	-	30	3.8	Parabolic, 36.6	360°
6.	500	$9.8 \cdot 10^3$	-	$1.2 \cdot 10^4$	784	Broadside array, 8 x 127 dipoles	Meridional 2θ parallels ±3.5°
7.	240	$46 \cdot 10^3$	0.1-3	$6 \cdot 10^3$	600	Broadside array, 100 x 100 dipoles	
8.	300	6880	-	$3 \cdot 10^5$	1250	Broadside array reception: interferometer length 3 km	
	300	920	-	$3 \cdot 10^3$	600	Broadside array	
	30	920	-	100	72	Broadside array	
9.	10	$2.5 \cdot 10^3$	-	1100	73	Parabolic, 75 (Mark 1)	360°
	0.18	170	0.02	950	250	Parabolic, 18	360°
10.	2.6	75	0.005	$1.7 \cdot 10^3$	10	Parabolic, 13.7	360°
11.	20	92	-	145	3.6	Parabolic, 15	360°
12.	12.5	90	0.002-0.005	600	10	Parabolic, 15	360°
13.	$8 \cdot 10^{-3}$	100	$2 \cdot 10^3$	450	0.86	Parabolic, 18.6	360°
14.	0.55	30	60	$1.8 \cdot 10^3$	250	Broadside array 36 dipoles	

where

a is the radius of the planet, km;

c is the speed of light, km/sec.

for the moon, t_p = 11.6 milliseconds.

Figure 3.1 is a schematic presentation of the temporal stretching of the pulse during reradiation of the energy by the surface of the planet.

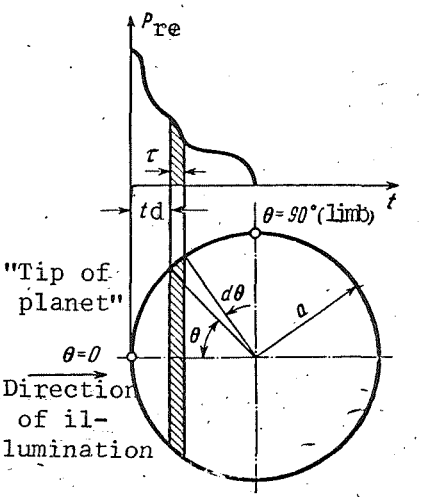

Figure 3.1. Reradiation of a pulse signal by a spherical surface.

/63

When the surface of a planet is illuminated by pulses with length τ, the annular zone of the planetary surface concentric with the earth-planet direction (that is, with the direction of propagation of the electromagnetic energy) reradiates at all moments in time.

The planetocentric angle of this annular zone will equal

$$\Delta\theta = \frac{c\tau}{2a\sin\theta} \quad \text{when} \quad \tau \ll \frac{a}{c}. \tag{3.2}$$

The delay in the leading edge of this echo relative to the tip of the planet (henceforth called simply delay) is associated with the angle of incidence of the illuminating energy at the spherical surface by

$$t = \frac{2a}{c}(1 - \cos\theta). \tag{3.3}$$

Keep in mind that the areas of all these instantaneously illuminated annular zones will be identical for a spherical surface, and will equal

$$\bar{S}_\tau = \pi ac\tau \quad \text{when} \quad \tau \ll a/c. \tag{3.4}$$

A train of pulse signals will appear at the ground receiver input during the experiment. The distribution of pulse amplitudes in terms of width (that is, in terms of delay, t) will depend on the θ of the annular scatterer on the planetary surface illuminated at the specific time. Eq. (3.3) now can be used to convert the reradiated power in terms of delay, $P_{re}(t)$, into $P_{re}(\theta)$. Readily apparent is the fact that normalization of this latter relative to its maximum, obtained when $\theta = 0$ will, in the case of a uniform illuminating flux power angular density at the lunar disk, yield the backscattering pattern

$$B(\theta) = P_{re}(\theta)/P_{re}(0). \tag{3.5}$$

An angular correction that takes into account ground receiving and transmitting antenna patterns, equal to the angular size of the planet, is introduced when the illuminating flux angular density is not uniform. /64

The level of signals reradiated by the center of the planet, and by regions close to the limb, can differ by tens of decibels, and this is considerably greater than the range of change in power over the linear part of the receiver's characteristic curve. The range of the linear part of the amplitude characteristic curve for a receiver usually is a maximum of 15 dB. Therefore, in order to measure $P_{re}(t)$, one uses step attenuation of the echo, with the number of steps exceeding the ratio of the dynamic range of the echo to the range of the linear part of the amplitude characteristic curve for the receiver, or a multichannel receiver with a different sensitivity in each channel.

A signal, reradiated by the annular zone, the extent of which is determined by the transmitted pulse width, will appear at the receiver input at each moment in time. The echo thus will be power averaged in the ranges of angles of incidence from θ to $\theta + \Delta\theta$.

Because echo strength definitely depends on the angle of incidence, the backscattering pattern obtained will be distorted when pulse modulation is used and the pulses are sufficiently long. Evans and Pettengill verified this experimentally at 68 cm [109]. Because the backscattering pattern is degraded on longer wavelengths, the result of its proximity to the mirror image, naturally enough the use of long transmitted pulses in this region will

result in a larger error in measurement of the backscattering pattern than is the case in the shortwave region.

Pulse widths from 2 μsec at λ = 10 cm [136] to 500 μsec at λ = 68 cm [155] have been used for pulse radars investigating the moon. This corresponds to resolution, in terms of angle of incidence, from 40" to 2.5°. Calculations have shown that, in order to keep the error within ±1 dB when determining the backscattering pattern in terms of the transmitted pulse width, its magnitude should not exceed 2.2 milliseconds at 3.6 cm, 1.35 milliseconds at 68 cm, and 0.75 millisecond at 600 cm (the experimental backscattering patterns were taken from reference [110]).

The ground radar's repetition rate should not exceed 38 Hz for the moon in order to obtain unambiguous results. The repetition rate ordinarily is about 30 Hz.

Illumination conditions change somewhat each time the surface of the planet is illuminated. This is the result of the movements of the ground radar antenna and illuminated surface with respect to each other because of the moon's libration, and because of change in the direction of the axis of the antenna as a result of all sorts of deformations (temperature changes, wind, mechanical load), as well as because of irregularity and errors as the antenna tracks the selected point on the lunar surface. These variations are associated with change in the position of the illuminated area, as well as /65 with change in the angle of incidence, causing a redistribution of the instantaneous centers of reradiation on the illuminated surface (so-called "bright spots"). These variations, moreover, can be associated with change in the properties of the earth's atmosphere and ionosphere during the transmitted pulse repetition period, but these usually are slight.

The result will be that the reradiated pulses will differ from each other at the receiver input at different repetition periods. This picture is aggravated by set noise.

Statistical methods are used to process the incoming signal because the phenomena that determine how signals fluctuate at the receiver input are random and independent. This accumulation of signals serves a dual purpose with respect to receiver output. First of all, it increases the S/N ratio,

providing greater accuracy in measuring reradiation characteristics averaged for the lunar disk, and, second, it reduces incoming signal fluctuations.

Noted in the course of measuring the characteristics of reradiation from the moon at 1.85 meters [21] and 2.5 meters [65] was the fact that the amplitude distribution law for the reradiated signals was close to Rayleigh, that the duration of fluctuations in the reradiated signals, because of the moon's libration, was several seconds and that depth of fluctuation was 15 to 20 dB [106, 136, 138, 165].

Integration time, in the majority of radar observations, was a few repetition periods. Fluctuations were greatly reduced.

The ionosphere surrounding the earth influences the propagation of ground radar signals traveling to the moon and back when radar measurements are made on wavelengths longer than 20 cm. The earth's magnetic field, in conjunction with ionized particles, causes the plane of polarization of the electromagnetic oscillations to rotate (the Faraday effect). The Faraday effect is proportional to the square of the wavelength, and can be characterized by temporal variations occasioned by variations in the earth's magnetic field, and by fluctuations in the electron density of the ionosphere. The angle of rotation of the plane of polarization, Ω, when radio waves are propagated in one direction, can be found from [95]

$$\Omega = 1{,}57 \cdot 10^{-4} \lambda^2 \int_0^h N_0 H \cos \xi \sec \chi \, dh, \qquad (3.6)$$

where

N_0 is the number of electrons per cubic centimeter;

H is magnetic field strength, oersteds;

ξ is the angle between the direction of propagation of the electromagnetic waves and the magnetic field vector;

χ is the angle between the direction of propagation and the zenith, degrees; /66

h is the height of the ionosphere, kilometers;

dh is an element of the height of the layer of the ionosphere along the path of propagation.

The process of change in the position of the plane of polarization occurs

primarily as a result of change in the concentration of charged particles in the ionosphere and does so quite slowly, varying in time from minutes to tens of minutes.

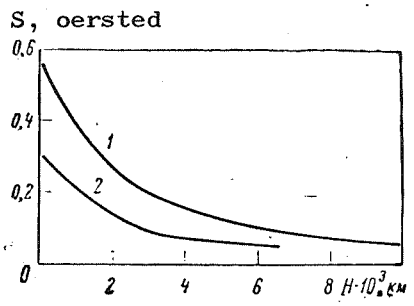

Figure 3.2. Strength of the earth's magnetic field in terms of height.
1 - in the region of the geomagnetic pole;
2 - at the geomagnetic equator.

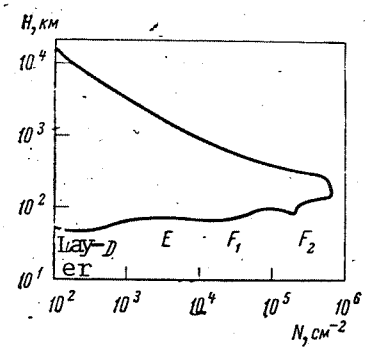

Figure 3.3. Electron profile of the ionosphere in the middle latitudes for quiet sun.

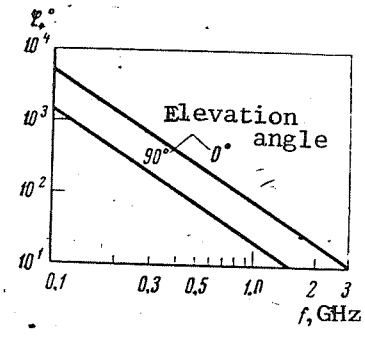

Figure 3.4. Faraday rotation angle in terms of frequency (the Faraday effect).

Figures 3.2 - 3.4 show the change that takes place in the earth's magnetic field strength with height, the electron profile of the ionosphere, and the Faraday rotation angle for the earth's middle latitudes in terms of frequency [46].

Matched circular polarization is used in radars for reception and transmission in order to eliminate change in the echo level caused by the Faraday effect.

Eqs. (2.87) and (2.89), cited in #3 of Chapter II, can be used to find

the radar cross section of the near side of the lunar surface in terms of the average incoming signal power when the antenna beamwidth exceeds the moon's angular size.

If the antenna beamwidth is very much narrower than the moon's angular size, the radar cross section of sections of it, the size of which can be determined by the antenna beamwidth without using a complicated frequency-time selection system, can be measured (see #4, Chapter III). The radar cross section in terms of selenocentric coordinates can be measured by having the antenna beam scan the lunar surface, and in this way obtain a radar chart of the lunar surface. /67

The procedure for constructing a chart such as this will be discussed in #4 of this chapter. The pulse radar is used only for lunar investigation because of its lower energy characteristics, and is not used when radar is involved in investigating planets from the earth. Continuous radiation methods, the radiation of a monochromatic signal, with linear frequency modulation in the case of a small index, and with frequency shift keying in the case of pseudonoise modulation, have been used to investigate the planets in the solar system closest to the earth, Mars, Venus, Jupiter, and Mercury. The latter method, because of its good energy characteristics, also is widely used today in systems for transmitting information over remote space communication lines.

Thus, the pulse method of radar detection of the moon from the earth makes it possible to measure the moon's radar cross section (for $2\theta_{ant} > 30'$) and the moon's backscattering pattern, $B(\theta)$, and, with an antenna system with a beamwidth $2\theta_{ant} < 30'$, to obtain a radar chart of the lunar surface with a resolution determined by the antenna beamwidth, or (when frequency-time selection is used) with a resolution determined by the characteristics of this selection arrangement (see #4, Chapter III).

Practice has shown that the accuracy with which the planet's radar cross section can be measured by radar detection from the earth is a mean of ±3 dB. Individual measurements were obtained with an accuracy of ±1 dB. The value of σ_{0N} can be found by using the equations in #4, Chapter II, and the measured values of σ and $B(\theta)$.

3. Radar Detection from the Earth Using a Continuous Monochromatic Signal

The angular rates at which the moon and the earth rotate on their axes just about coincide, so a part of the lunar surface, the size of which changes somewhat in terms of time because of the moon's libration, always can be seen from the earth. This means the ground observer can see 59 percent of the entire lunar surface, rather than 50 percent.

Libration occurs because of the inclination of the plane of the moon's equator to the plane of its orbit, the result of the different angular rate of revolution of the moon as it moves in an elliptical orbit around the earth, and because of the observer's parallax, the result of his not being at the earth's zero latitude. The angular rate of the libration changes in the range $\omega_{lib} = (5 - 10)\ 10^{-7}$ radians per second [80].

Libration causes the spectrum of the echo from the lunar surface to differ from that of the illuminating pulse.

The movement of the moon's center of mass with respect to the ground observer results in a constant shift in frequency, Δf, and the moon's libration generates Doppler frequencies in the echo that depend on the distance of the scatterers within the plane of the figure from the axis of libration (see Figure 3.5). /68

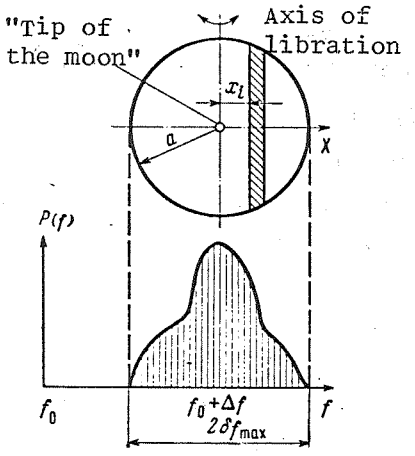

Figure 3.5. Formation of the Doppler spectrum by the moon's libration.

The geometric loci of points on the lunar surface with identical Doppler frequencies will be concentric circles lying in a plane perpendicular to the

plane of the figure, and parallel to the axis of libration (bands parallel to the axis of libration in the plane of the figure). The Doppler frequency increases linearly from the axis of libration to the limb of the moon in a direction normal to the axis of libration.

The Doppler effect results in the echo from each band in the plane of the figure at distance x from the axis of libration having a frequency shift that can be determined from

$$f_i = \frac{2\omega_л x_i}{c} f_0. \qquad (3.7)$$

The Doppler expansion in the spectrum of frequencies from the entire planet is

$$2\delta f_{max} = \frac{4\omega_л a}{c} f_0. \qquad (3.8)$$

The value of the Doppler frequencies in the echo spectrum can be established uniquely by the location of the scatterer on the lunar surface, so the backscattering pattern can be obtained from the echo spectrum.

A spectrum analyzer can provide the true distribution of echo power spectral density in the case of the ideal monochromatic signal and infinite frequency resolution. The relationship between the relative value of the echo power spectral density for the particular Doppler frequency and that of the intensity of the reradiated power for the corresponding angle of incidence will yield the backscattering pattern. /69

Deviation in the spectrum from monochromatic at the receiver output is determined by instability in the frequency of the transmitter frequency and of the master oscillator in the receiver. Today, persistent instability in these frequencies has been reduced to 10^{-9}, which is an instability of ~ 1 Hz at a frequency of 1000 MHz. The transient instability (lasting for a few minutes) is between 1 and 1.5 orders of magnitude higher. A spectrum width ~ 5 Hz has been achieved for a wavelength of 8.6 mm ($f \simeq 3.5 \cdot 10^{10}$ Hz), corresponding to a transient instability of $1.4 \cdot 10^{-10}$ [147].

Modern techniques of spectral analysis used in observing the planets with radar (the Arecibo radar operated by Cornell University) can resolve frequency differences of 0.02 Hz [159], and this is equivalent to obtaining spectrum resolution at a frequency of 440 MHz for a lunar echo equal to

$$\delta f/2\delta f_{\max} = 0{,}02 \text{ Hz}/10{,}3 \text{Hz} \simeq 0{,}2\%. \tag{3.9}$$

Here $2\delta f_{\max}$ was found by using Eq. (3.8).

Goldstein [117] and Karpenter [137] derived formulas for determining the connection between the backscattering pattern for the near side of the moon, B(θ), and the echo frequency spectrum, p(f)

$$p(f) = \int_{\sin^{-1}(f/\delta f_{\max})}^{\pi/2} \frac{B(\theta)\sin\theta\, d\theta}{(\delta f_{\max}^2 \sin^2\theta - f^2)^{1/2}}, \tag{3.10}$$

$$B(\theta) = -\frac{2(\delta f_{\max})\cos\theta}{\pi} \int_{\delta f_{\max}\sin\theta}^{\delta f_{\max}} \frac{p'(f)\, df}{(f^2 - \delta f_{\max}\sin^2\theta)^{1/2}}. \tag{3.11}$$

Here, f, P(f), and P'(f) are, respectively, the frequency, the power spectral density, and its derivative, corresponding to the band x distant from the axis of libration (see Figure 3.5). Eq. (3.11) was obtained from Eq. (3.10) by an inverse transformation using the Abel integral equation.

The derivations of Eqs. (3.10) and (3.11) assumed that all elements on the surface have the same backscattering pattern, no reradiation among individual surface elements existed, and that the total echo power is the sum of the powers reradiated by the scatterers.

The magnitude of the equivalent scattering area of the lunar surface is /70
readily obtainable from the formulas cited in #3, Chapter II, once the full echo power is measured. Radar measurements resulting from the use of monochromatic radiation provide the backscattering pattern, B(θ), and the radar cross section, σ, of the near side of the lunar surface, that is, the same parameters obtained when pulse radar is used. The accuracy is of the same order of magnitude in either case.

The echo received by CW planetary radars is processed as follows. A spectrum analyzer is installed at the output from the last frequency converter, and analysis is series, or parallel.

The series analysis spectrum analyzer is a narrow-band bandpass filter with bandwidth Δf, equal to the required frequency resolution. The middle frequency of this filter is retuned continuously, or discretely, in the frequency band equal to the width of the echo spectrum. This is the design used

to build most frequency characteristic analyzers, sweep generators, and spectrum measuring analyzers. Spectrum analysis time is quite high, however. The time to obtain one spectrum, when required resolution is 1/N = 0.2% of the Doppler spectrum of the echo, $2f_{max}$ = 10 Hz, will be

$$T_{an} = 3N^2/2\delta f_{max} = 3 \cdot 500^2/10 = 7{,}5 \cdot 10^4 \text{ sec} = 20{,}9 \text{ frequencies} \qquad (3.12)$$

where

N is the number of spectrum sections analyzed.

This long analysis time is why systems containing retunable filters are not widely used in planetary radars.

The parallel analysis arrangement uses a multichannel filter consisting of parallel connected narrow-band band-pass filters, the middle frequencies of which are tuned to a magnitude that is a multiple of the pass band for each filter, and this latter is fixed by the required echo spectrum frequency resolution, or by the engineering potentials for building narrow-band filters. At the output from each filter is a square-law detector, providing a DC voltage proportional to the product of signal power spectral density and the filter pass band width. The planetary radar receiver thus is designed to be linear, so the voltage across the output of the square-law detector will be proportional to the echo power spectral density.

The DC voltage across the outputs of the square-law detectors is recorded /71
on the paper tape of multichannel recorders. The multichannel analyzer reduces the analysis time by a factor of N, compared to that provided by a single-channel, retunable analyzer. A correlation spectrum analyzer with a digital correlator can be used at the receiver output when the S/N ratio is not high enough.

The block diagram of correlation processing such as this would look as follows. The signal, and the noise, are fed from the output of the amplifier in the last frequency conversion stage to a time quantizer switch. The spectrum of this signal contains all the Doppler frequencies of the echo, symmetrically located on both sides of the middle frequency to which the filter for the receiver's last i-f amplifier is tuned.

The i-f amplifier pass band, Δf_i, is selected close to the Doppler spectrum of the echo, $2\delta f_{max}$.

The conversion of the continuous signal into a digital one is accomplished by series time and amplitude quantization. Time quantization is accomplished by a switch with constant signal interrupter frequency. A train of amplitude modulated pulse signals of constant duration and repetition rate appears at the switch output. The pulse repetition rate is selected wider than the spectrum of the Doppler frequencies in the signal so that quantization will not result in loss of the CW envelope containing information on the signal spectrum. The signal then is fed into the amplitude quantizer. This was a simple, two-level quantizer-limiter in certain experiments, and a multilevel amplitude sampler in others. The signal path now is from the output of the signal limiter to the digital correlator. Correlator storage capacity is selected such that an adequately long observation time, T_{ob}, will not overload it.

The correlator calculates the autocorrelation function of the signal and noise supplied to its input. Analysis has shown that this function agrees quite well with the autocorrelation function of a continuous signal with noise at the output of the receiver's i-f amplifier.

The S/N ratio in the spectrum analyzer, found from [117]

$$\left(\frac{P_s}{P_n}\right)_{out} = \frac{1}{\pi}\left(\frac{P_s}{P_n}\right)_{ifa}(\Delta f T_{ob})^{\eta_1}. \qquad (3.13)$$

improves with increase in analysis time.

The digital signal describing the autocorrelation function is fed from the correlator output to the computer handling the signal spectrum calculation, that is, making the inverse Fourier transform. Since receiver set noise is processed with the signal, the spectrum that results is the spectrum signal plus the noise. The noise spectrum can be calculated similarly, and the /72
noise spectrum contained in the signal plus noise spectrum can be calculated to obtain the noise spectrum, with the result the spectrum of just the signal remaining. This can be done by operating the radar in an alternating mode, radiating, then turned off.

During the turned-off cycle hardware noise will appear at the input to the spectrum analyzer and its spectrum will be subjected to correlation processing. Signal plus noise will appear at the spectrum analyzer input during

the radiation cycle and the result of processing will be the signal plus noise spectrum. The noise spectrum now is extracted from the signal plus noise spectrum to obtain the unknown Doppler spectrum of the echo from the planet.

4. Radar Detection from the Earth Using Pulse Modulation and Doppler Frequency Spectrum Analysis

Investigation of the properties of scatter from small regions of the lunar surface is a current problem for two reasons. First, flights by automatic and manned spacecraft in orbits as artificial moon satellites, as well as their landings on the lunar surface, require knowledge of these parameters in order to determine the energy characteristics of the r-f equipment installed in the spacecraft. Second, the scatter characteristics of fairly small, local regions, together with the results of measurements of properties of the surfaces of these regions by other means, will provide valuable data on the physical characteristics of the surface, and of the surface layers, in these regions. Variations in the physical properties of the lunar surface thus obtained will make it possible to estimate the inhomogeneity of the lunar surface layer, and, on the basis of definite hypotheses, arrive at a judgment concerning the history of the moon's development.

Improvement in area resolution can come about in two ways when investigating the distribution of the lunar surface scatter characteristics.

The first is to reduce the beamwidth of the planetary radar. Modern antenna engineering provides antenna systems with a beamwidth of 6 - 10', corresponding to the simultaneous illumination of an area in the center of the lunar disk with a diameter of 650 - 960 km. There is little possibility of significant improvement in angular resolution because the task of designing antenna systems with such narrow beams is extraordinarily complex. /73

The second approach is the use of echo time, as well as frequency, selection. A combination of delay time selection, used in pulse radar detection, and Doppler frequency selection, used in continuous radar detection, will result in obtaining resolution of smaller areas on the planet's surface than is the case when but one of these methods is used, and also will make if possible to determine the selenographic coordinates of these areas.

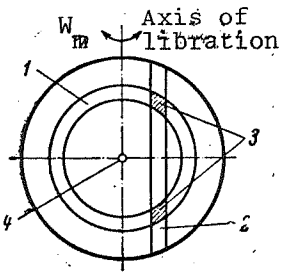

Figure 3.6. Frequency-time selection and identification of sections on the surface.

1 - annular zone isolated by time selection;
2 - zone isolated by Doppler frequency selection;
3 - regions separated by a combination of the two types of selection;
4 - "tip" of the moon.

The pulse selection method isolates an annular region corresponding to the specified delay on the disk of the planet in the plane of the figure, and frequency selection isolates a band parallel to the axis of libration corresponding to the specified Doppler frequency, so combined selection isolates two regions formed by the intersection of these zones (see Figure 3.6). As will be seen from the figure, when the ground radar's beamwidth is larger than the angular size of the moon from the earth, there are two zones on the lunar disk, symmetrically located simultaneously with respect to an axis normal to the axis of libration, that correspond to identical Doppler frequencies and identical delays. Consequently, a unique correspondence between small areas on the lunar surface and the frequency-time characteristics of the echo can be arrived at if the ground antenna beamwidth is less than half the angular size of the moon from the earth (that is, $< 15'$). This condition is met by the largest of the planetary radars, such as the Cornell University's radar in Arecibo, the USSR's planetary radar, the West Ford radar of the Lincoln Laboratory, and the Maryland Observatory radar.

This method of radar detection requires a much higher peak power than is the case for pulse radar detection because the useful signal decreases in proportion to the ratio of the Doppler frequency spectrum to the pass band of one filter for the same radiated power and the same pulse width. Hence, these investigations can be made only by planetary radars with high peak powers.

A radar chart of the lunar surface is obtained from tieing in the scatter intensity and the selenographic coordinates of the scatterers. Two problems must be solved in order to construct the charts.

1. Identify the delay and the Doppler frequency in the echo with /74
the selenographic coordinates of the scatterer.

2. Determine the scatter intensity from the corresponding scatterer.

The radar chart is superimposed on a photographic mosaic of the region on the lunar surface investigated in order to simplify analysis and interpretation of the radar measurements. Thompson and Dyce [166, 159, 167] selected photographic charts from Kuiper's Photographic Lunar Atlas [141], as well as some from the album of Lunar Astronautical Charts (LAC), scale 1 : 1,000,000 [145], for comparison with the radar charts of the moon.

The accuracy of the tie between the scatterer and its selenographic coordinates is one-half the size of the target in delay and Doppler frequency. Pettengill and Henry [155], in the first experiment with the Millstone Hill radar to investigate the echo properties in the region of the crater Tycho, obtained a resolution of ±25 km for both selenographic coordinates when τ_p = 100 μsec. Thompson and Dyce used the Arecibo radar to obtain a resolution of 20 km in delay for this same region, and 37 km in Doppler frequency (when τ_p = 100 μsec and Doppler frequency resolution was 0.1 Hz).

Delay and frequency resolution for other regions of the lunar surface investigated ranged from 25-37 km and 35-38 km, respectively.

Area resolution is greatly dependent on its selenographic coordinates, degrading with movement from the center of the disk to the limb. Plans for future work to improve the characteristics of the planetary radar in Arecibo [159] have proposed increasing the delay and Doppler frequency resolution by a factor of 5, reducing the width of the transmitted pulse to 20 μsec, and increasing the Doppler frequency resolution to 0.02 Hz. This would result in resolution at the lunar disk of 3 to 8 km in delay, and 5 to 10 km in Doppler frequency (for the full width of the spectrum of Doppler frequencies from the lunar disk equal to 10 - 14 Hz) on a wavelength of 70 cm.

Later measurements made by Pettengill and Thompson [156] on 3.8 and 70 cm after the radar had been modernized resulted in the obtaining of a radar chart of the crater Tycho with resolution of 1 - 2 and 7 - 10 km, respectively, for the two coordinates. A λ = 3.8 cm radar chart then was obtained for a polarized, as well as a depolarized, component of the echo. Figures 3.7 - 3.9 are a radar chart of the crater Tycho region, a photographic mosaic of the same region borrowed from the LAC atlas, and a photograph of the crater Tycho obtained by Lunar Orbiter 5.

It is very difficult to establish the characteristics of the reradiation /75
from the tie to the scatterers on the lunar surface.

Reradiation conditions for each scatterer, the size of which is determined by the delay and Doppler resolution, determine the backscattering pattern, which is measured only as the average for the whole of the lunar disk. Moreover, the geometric area of the scatterer is unknown because there are no data on the distribution of surface slopes in the area investigated. Lack of such data requires the introduction of a number of simplifications and assumptions when compiling a radar chart of the lunar surface and this, naturally enough, results in certain differences in the characteristics obtained for reradiation from the areas shown on the radar chart from their true values. None of the authors of radar cartography have estimated these differences, so the existing radar chart of lunar regions must be assessed as qualitative, rather then quantitative, so far as characteristic of reradiation from local surface areas are concerned. This is particularly true of regions near the limb, and of measurements of absolute echo characteristic values. The following premises were adopted in compiling radar charts of the regions of the moon investigated.

1. The radar chart can be compiled for the case of rearward scattering for normal incidence.

2. Measurements of echo properties are relative. Thompson took the relatively flat, smooth region of Mare Imbrium as the standard for calibration, and characteristics of reradiation from an unknown region were compared with those of the standard region. This was done because absolute calibration of a radar is extremely complicated.

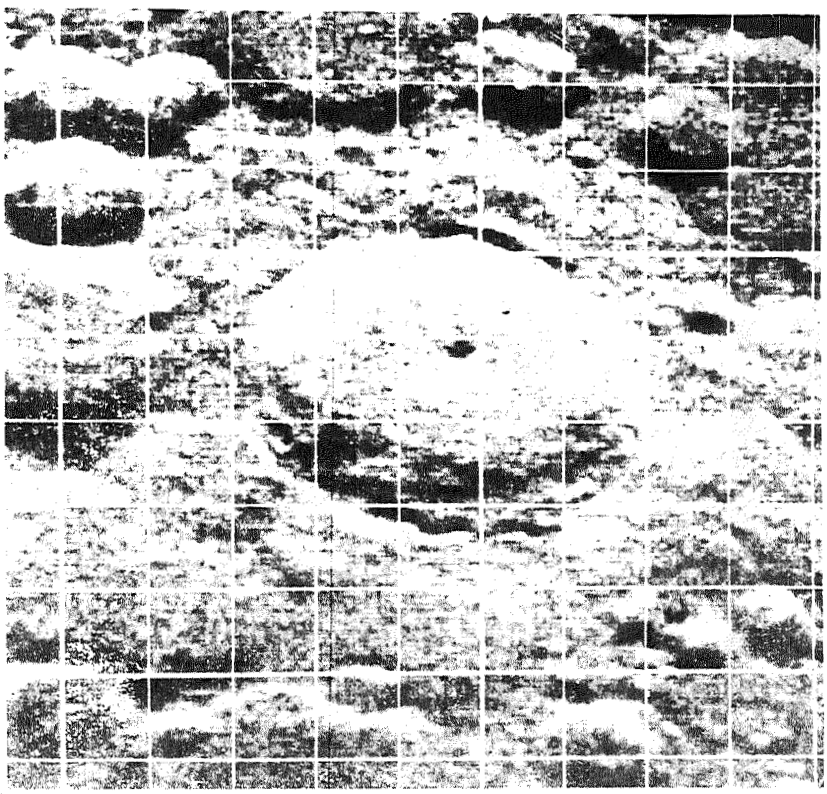

Figure 3.7. Radar chart of the crater Tycho with high resolution on a wavelength of 3.8 cm (G. H. Pettengill, T. W. Thompson - Icarus, 1968, 8, No. 3).

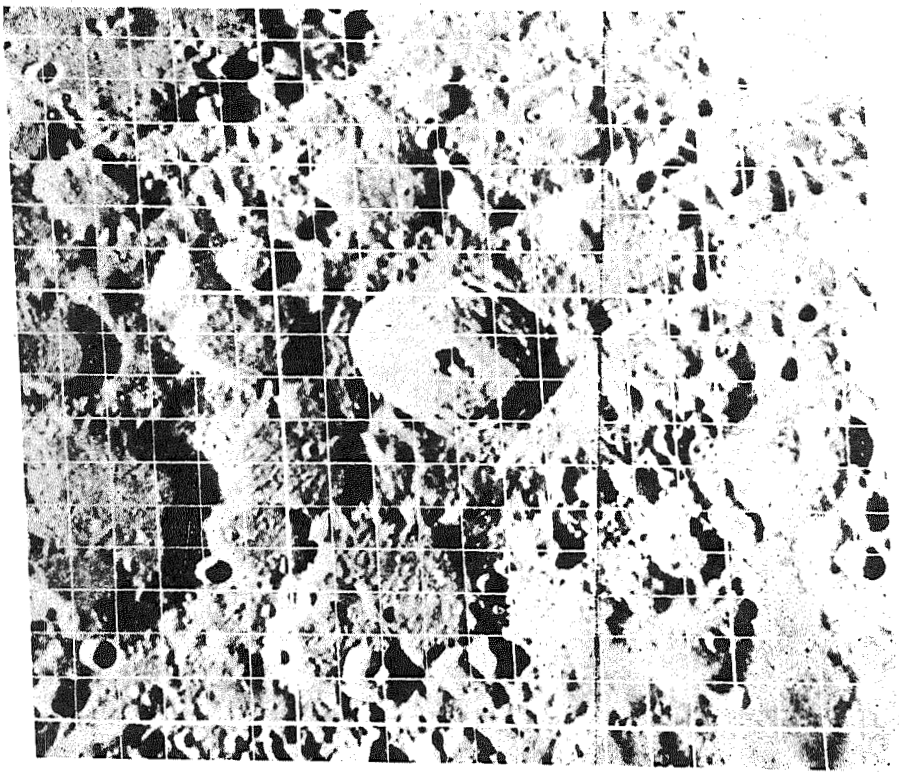

Figure 3.8. Photographic chart of the crater Tycho from earth observations. (G. H. Pettengill, T. W. Thompson - Icarus, 1968, 8, No. 3).

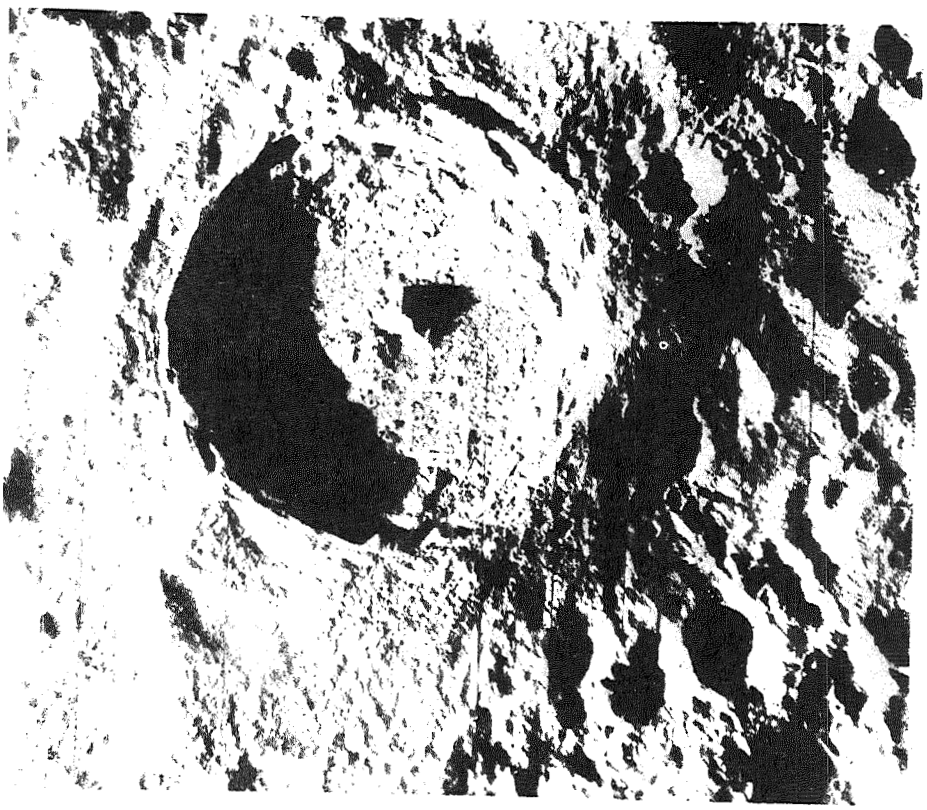

Figure 3.9. Photography of the crater Tycho from Lunar Orbiter 5 (G. H. Pettengill, T. W. Thompson - Icarus, 1968, 8, No. 3).

3. Reradiation properties can be estimated from the magnitude of N, which is proportional to the ratio of the corrected value of the power reradiated in the rearward direction to the incident power at the area of the lunar surface considered, the dimensions of which are determined by the resolution of the radar [117, 167]

$$N = c P^{*}_{re} / P^{*}_{in}. \tag{3.14}$$

4. The magnitude of the power incident at the surface under consideration is determined by the incident flux power angular density (the radar's antenna pattern taken into consideration), size of the area, and the angle between the direction of incident and the local vertical to the surface at the center of this area. The true slope of this area relative to the local vertical thus is not considered.

$$P^{*}_{in} = \frac{P_{trans} G_{max}}{4\pi R^2} F(\alpha) \cos\theta \Delta S, \tag{3.15}$$

where F (α) is the radiation pattern of theradar transmitting artenna in the direction to the area to be investigated; /76

ΔS is the size of the area investigated, equal to the resolution on the lunar surface for the planetary radar for the selenographic coordinates of the area;

θ is the angle between the direction from the ground radar to the center of the area and the local vertical for that area;

R is the distance from the radar to area investigated.

5. The magnitude of the power reradiated back to the radar can be calculated for the case of normal incidence by using the averaged backscattering pattern, measured for the entire near side of the moon

$$B(\theta)_{\Delta S} = \bar{B}(\theta). \tag{3.16}$$

6. The magnitude of the power reradiated by the area investigated can be calculated from the data from the spectral analysis of the echo as follows

$$P^{*}_{re} = \frac{P_{rec}(f) \Delta F_D \bar{B}(\theta) 4\pi R^2}{A_{rec} F_{rec}(\alpha)}, \tag{3.17}$$

where

$F_{rec}(\alpha)$ is the radiation pattern of the radar receiving antenna in the direction of the area investigated.

A_{rec} is the effective area of the receiving antenna;

ΔF_D is the resolved band of Doppler frequencies, corresponding to the band of frequencies from the area investigated;

$P_{rec}(f)$ is the power spectral density of the echo from the lunar surface at the input to the radar receiver, corresponding to the area investigated in terms of delay and Doppler frequency.

7. It can be assumed that mutual reradiation from neighboring sections of the surface is absent. This is valid for surfaces with small echo factors. The lunar surface is one such surface.

8. The proportionality factor in Eq. (3.14), c, is selected by researchers such that $N \simeq 100$ for a section of the lunar surface, the return from which is close to the average characteristic for the lunar surface.

As will be seen, the chart of the lunar surface, while not reflecting the true properties of the return for normal incidence, does show regions with increased backscattering (increased "radar brightness").

Compilation of radar charts is very time consuming, so global radar cartography of the entire near side of the moon from the earth is scarcely a possibility.

Measurements have been made, however, and radar charts of regions with increased backscattering have been compiled. These are the regions of the /77
"young" lunar craters, such as Copernicus, Aristillus, Tycho, Theaetetus, Werner, and some others. Figure 3.10 is a radar chart of the region in which the crater Tycho is located. It is known for its heat, optical, and radar anomalies. Corresponding delay and Doppler frequency grids are overlaid. Figures corresponding to N in Eq. (3.14) are entered at the points of intersection of lines of identical delay and Doppler frequency, and equal reradiation power lines (lines of equal N) are plotted.

It is extremely difficult to process the echo spectra from the area investigated to determine the power spectral density at the receiver output, $P_{rec}(f)$. Fluctuations in the echo, and an inadequate S/N ratio, require acquisition and averaging of the results of several spectra, measured for the same delay in the interval of delays equal to the pulse width. The signal spectrum for this delay can be determined by digital computer processing of

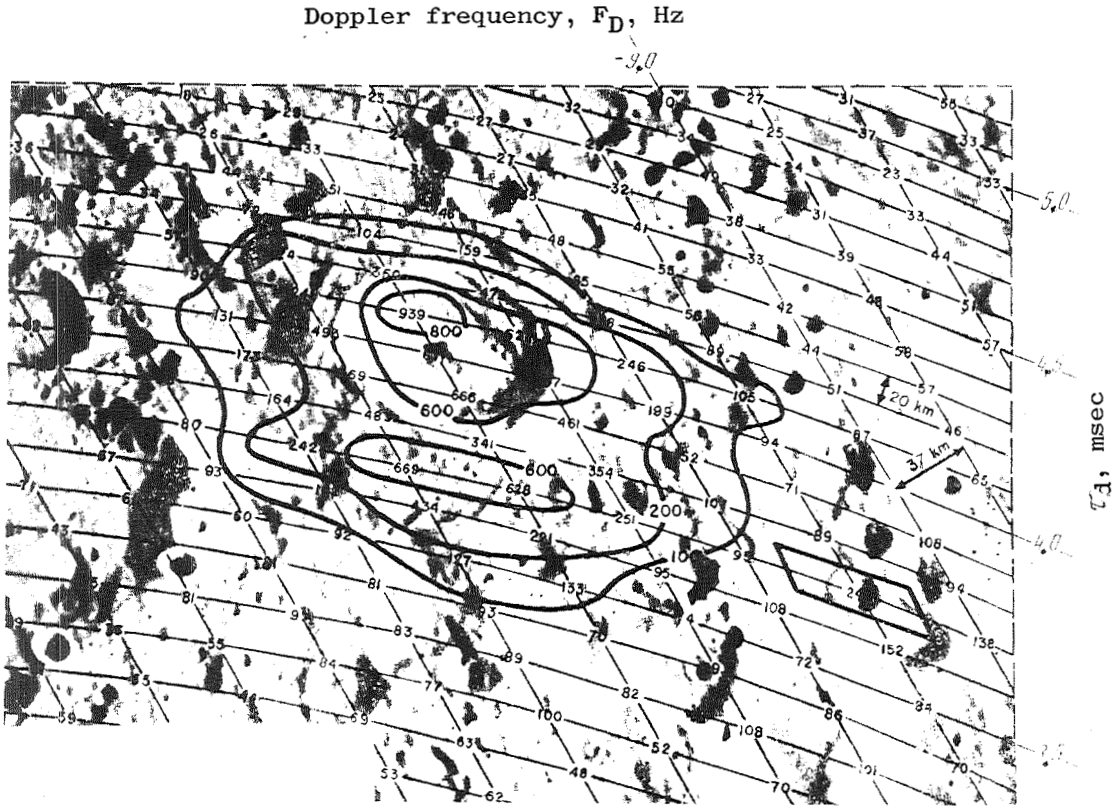

Figure 3.10. Radar chart of the crater Tycho at a wavelength of 70 cm.

(Doppler frequency, F_D, Hz - horizontal; τ_d, msec - vertical)

the autocorrelation function of this signal, obtained from the receiver output and corresponding to the delay, using an inverse Fourier transform. Square-law detection is used to obtain the signal amplitude at the receiver input proportional to the power of the incoming signal. Conversion of the CW signal into digital form introduced correlation processing in digital form and this simplified obtaining the autocorrelation function, and increased its accuracy as compared to correlation of an analog function.

If $\sigma_{0\ N}$ for some part of the surface with coordinates φ_1, and λ_1, for which N_1 is known, determined by frequency-time selection, can somehow be measured, and if the limitations introduced in this section are taken into consideration, $\sigma_{0\ N_i}$ for any region with coordinates φ_i and λ_i can be determined, provided N_i for it is known. In this case, $\sigma_{0\ N_i}$ can be determined from

$$\sigma_{0N_i} = \frac{\sigma_{0N_1} N_i \Delta S_1}{N_1 \Delta S_i}, \tag{3.18}$$

where

ΔS_1 is the area of the known scatterer with coordinates φ_1, λ_1;

ΔS_i is the area of the scatterer with coordinates φ_i, λ_i, investigated.

Thus, the formula will provide a chart of the near side of the lunar surface showing the distribution of the radar cross section per unit area for the lunar surface. This chart will have practical importance for calculating the energy characteristics of electronic equipment in use near the lunar surface.

5. Investigation of the Characteristics of Reradiation from the Surface with a Radio Altimeter or Radar Installed in a Spacecraft near the Lunar Surface /78

Signals that depend on the altitude at which a spacecraft is flying, and which are generated by a radio altimeter, are used by the spacecraft control system when spacecraft are orbiting the moon, as well as when they land. These can be individual signals, generated when specified heights above the surface are reached, or they can be continuous signals, the voltage, or current, of which is some function of the altitude.

Many parameters associated with the equipment in the spacecraft are recorded by telemetry in order to monitor control system operation. A whole

series of radio altimeter parameters are monitored in this way, including the voltage, which depends on the altitude at which the spacecraft is flying, or the fact of reaching one of the specified heights above the surface (depending on the radio altimeter output design), transmitter power, voltage across the receiver output, and the voltage across the receiver's automatic gain control (AGC). In addition, data on certain control system parameters, to be discussed in what follows, are needed to establish the properties of surface reradiation.

The characteristics of surface reradiation can be obtained from the energy characteristics of the communication line, instrument-surface-instrument. As will be shown, calculation of communication line energy characteristics from experimental data can provide the radar cross section per unit area for the lunar surface.

Let us consider the power requirements for the instrument-surface-instrument communication line for the general case of operation of a radio altimeter over the surface when the axis of the antenna beam is inclined at an angle θ_0 relative to the normal (to the local vertical) to the surface, and the antenna of the radio altimeter illuminates parts of the lunar surface. Reception and transmission use a common antenna in this case. Let us, for purposes of simplification of the calculations, assume that the radio altimeter's beam is symmetrical in terms of its axis.

Because the radio altimeter beam in the plane perpendicular to its axis usually is an ellipse, the introduction of the concept of radar cross section can reduce this problem to that of calculating the power for the radio altimeter communication line with a beam symmetrical to its axis

$$F(\alpha) = [F(\gamma) F(\beta)]^{\frac{1}{2}}, \tag{3.19}$$

where

$F(\gamma)$, $F(\beta)$ are the power patterns, measured in the orthogonal planes. /79
In this case, the power radiated by antennas with real and idealized patterns will be the same.

The radio altimeter transmitter emits high-frequency pulses with power P_r. The power incident on an area of dimensions dS of illuminated surface is

$$dP_{\text{in}} = \frac{P_t G_0 F(\alpha)}{4\pi R^2} dS, \tag{3.20}$$

where

G_0 is the maximum antenna gain;

$F(\alpha)$ is the averaged antenna pattern (AP) for the radio altimeter;

R is the distance from the antenna to the illuminated area dS.

Figure 3.11 shows the positions of the altimeter antenna and the illuminated surface relative to each other.

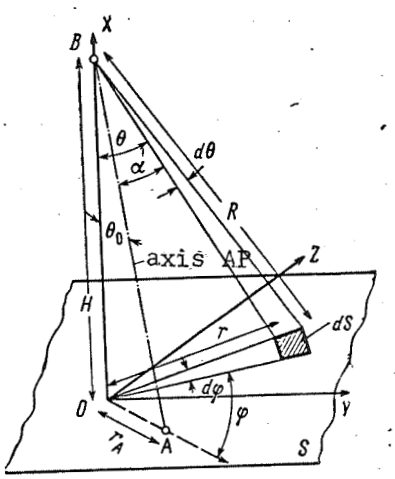

Figure 3.11. Geometry of reradiation.

The power reradiated by area dS will equal

$$dP_{\text{re}} = dP_{\text{in}} \sigma_{0N} B(\theta). \tag{3.21}$$

The echo from area dS at the altimeter receiver input will be

$$dP_{\text{r}} = \frac{dP_{\text{re}}}{4\pi R^2} \frac{G_0 F(\alpha) \lambda^2}{4\pi}. \tag{3.22}$$

Substituting dP_{in} and dP_{re} values from Eqs. (3.20) and (3.21) into Eq. (3.22)

$$dP_{\text{r}} = \frac{P_t G_0^2 F^2(\alpha) \lambda^2}{(4\pi)^3 R^4} \sigma_{0N} B(\theta) dS. \tag{3.23}$$

Total echo power at the receiver input can be found by integrating Eq. (3.23) /80 in terms of the whole of the illuminated surface, S

$$P_{\text{r}} = \frac{P_t G_0^2 \lambda^2 \sigma_{0N}}{(4\pi)^3} \int_S \frac{B(\theta) F^2(\alpha)}{R^4} dS. \tag{3.24}$$

Let us replace integration in terms of the surface by integration in terms of φ and θ. Remember that (see Figure 3.11)

$$R = H/\cos\theta, \tag{3.25}$$

$$r = H\,\mathrm{tg}\,\theta, \tag{3.26}$$

$$dS = \frac{Rr\,d\varphi\,d\theta}{\cos\theta} = \frac{H^2\sin\theta}{\cos^3\theta}\,d\varphi\,d\theta. \tag{3.27}$$

Here H is the height of the altimeter antenna above the surface. Accordingly

$$P_{\text{пр}} = \frac{P_{\text{т}} G_0^2\lambda^2}{(4\pi)^3 H^2}\,\sigma_{0N}\int_0^{2\pi} d\varphi \int_0^{\pi/2} B(\theta)\,F^2(\alpha)\sin\theta\cos\theta\,d\theta. \tag{3.28}$$

Eq. (3.28) is the precise expression for calculating the energy potential for the altimeter when the size of the illuminated surface is determined by the beamwidth. The formula for the power at the receiver output will be in a different form when the size of the illuminated area is determined by the pulse width. Now Eq. (3.28) will include the coefficient F(ρ) under the integral sign. It determines the shape at the receiver input, and depends on the altitude at which the spacecraft is flying, the beamwidth, and the inclination of the antenna axis to the local vertical. According to reference [26]

$$F(\rho) = \int_{x_1}^{x_2} xe^{-\frac{x^2+\varepsilon^2}{2}} I_0(\varepsilon x)\,dx, \tag{3.28a}$$

where

I_0 is a modified first-order Bessel function.

$$\rho = R - H = \frac{ct}{2}, \quad \rho_{\text{p}} = \frac{c\tau_{\text{p}}}{2}, \quad \varepsilon = \sqrt{\pi}\,\frac{\theta_0}{\alpha_{0,5}}, \quad x = \frac{\sqrt{\pi}}{\alpha_{0,5}}\,r;$$

$$x_1 = \begin{cases} 0 \text{ when } \rho \leqslant \rho_{\text{н}} \\ \sqrt{\dfrac{2\pi}{H\alpha_{0,5}^2}(\rho - \rho_{\text{н}})} \text{ when } \rho \geqslant \rho_{\text{p}} \end{cases}; \quad x_2 = \sqrt{\frac{2\pi}{H\alpha_{0,5}^2}\,\rho}.$$

Here, and in what follows, $\alpha_{0.5}$ is the half-power beamwidth, t is the time reckoned from first contact of the transmitted pulse with the surface, and τ_{p} is the pulse width. /81

Eq. (3.28) contains the mathematical expressions for the backscattering pattern and the antenna pattern, measured on different coordinate systems. Conversion of the antenna pattern from the instrument system (α) to the planetary system (θ) necessitates the use of the known association between angles α and θ

$$\cos\alpha = \cos\theta\cos\theta_0 + \sin\theta\sin\theta_0\cos \tag{3.29}$$

With Eqs. (3.29) and (3.28a) in mind, Eq. (3.28) becomes

$$P_r = \frac{P_t G_0^2 \lambda^2 \sigma_{0N}}{(4\pi)^3 H^2} \int_0^{2\pi} d\varphi \int_0^{\pi/2} B(\theta) F(\rho) F_1^2 \times \\ \times [\arccos(\cos\theta\cos\theta_0 + \sin\theta\sin\theta_0\cos\varphi)]\, d\theta. \tag{3.30}$$

Numerical solution of Eq. (3.30) yields the reflectivity of the surface for the values of the magnitudes of the parameters contained in this equation. The current values of P_r and P_t are found from telemetry from the altimeter, and those for G_0, λ, and $F(\alpha)$ from altimeter ground tests. The current value of θ_0 can be calculated from spacecraft control system telemetry. The current value of H can be determined from altimeter data, or from the ballistic calculation of the trajectory along which the spacecraft is moving, with a correction for the time the altimeter supplies recorded altitudes.

The numerical solution of Eq. (3.30) requires a mathematical approximation of the backscattering pattern and the antenna pattern. That for the antenna can be made in accordance with one of the following laws [41]

$$F(\alpha) = \cos^s(\alpha), \tag{3.31}$$

$$F(\alpha) = e^{-\alpha^2/2\sigma^2}, \tag{3.32}$$

$$F(\alpha) = \cos^2(k\sin\alpha). \tag{3.33}$$

The parameters s, σ, and k in these formulas are determined from an experimental antenna pattern as follows:

$$0{,}5 = \cos^s(\alpha_{0,5}) \tag{3.34}$$

$$0{,}5 = \cos^2(k\sin\alpha_{0,5}), \tag{3.35}$$

$$\sigma = 1{,}24 \cdot 57{,}3\lambda/D, \tag{3.36}$$

where

D is the diameter of a parabolic antenna;

$2\alpha_{0.5}$ is the half-power beamwidth;

2σ is the effective beamwidth.

The following can be used to approximate the backscattering pattern

$$B(\theta) = (\cos^4\theta + C\sin^2\theta)^{-3/2}, \tag{3.37}$$

$$B(\theta) = \cos^m(\theta). \tag{3.38}$$

C can be determined from Figure 2.6 for the given wavelength, and m from

$$0{,}5 = \cos^m(\theta_{0.5}), \tag{3.39}$$

where

$2\theta_{0.5}$ is the half-power backscattering pattern.

The unknown in Eq. (3.30) is the backscattering pattern for the illuminated section of the lunar surface. Measurement of the backscattering pattern for small sections of a surface from spacecraft is very complex, but is possible from an artificial planetary satellite when antenna scan in the plane of the orbit takes place as it moves. The relationship between the angular position of the antenna and the local vertical for the illuminated area can be determined by using the trajectory measurements. The group that equates to the selected area can be selected from the measurements. The results of the measurements in this group will correspond to different angles of incidence. Normalizing the echo power for different angles of incidence to its value when incidence is normal, we obtain the backscattering pattern for angles of incidence determined by the parameters of the satellite's orbit, and the antenna scanning angles. If antenna scanning, or scanning by the spacecraft when the antenna is fixed to the hull, takes place during the descent to the surface of the planet, different sections of the surface will be illuminated throughout the experiment. Hence, the relationship between the angle of incidence and the echo strength, normalized with respect to the slant range, will reflect the actual backscattering pattern for the surface only when the electromagnetic characteristics of the surface layer are identical, and the surface shapes of all areas illuminated during the experiment are the same.

The backscattering pattern for the particular area of the lunar surface can be said to coincide with the averaged backscattering pattern for the entire near side of the lunar surface when the antenna pattern is sufficiently narrow as compared with the width of the backscattering pattern ($\alpha_{0.5} < \Delta B(\theta)_{0.5}$) and small angles of inclination of the axis of the antenna pattern from the local vertical ($\theta_o < \Delta B(\theta)_{0.5}$). /83

Aided by these simplifications, Eq. (3.30) can be used to find $\sigma_{0\,N}$, and the error can be estimated for concrete experimental conditions. The difference in surface layer characteristics in the region studied from the averaged characteristics of the surface on the near side of the moon can be

evaluated by comparing $\sigma_{0\ N}$, measured for the particular area, with the averaged $\bar{\sigma}_{0\ N}$ for the whole of the near side.

6. Radar Detection Using a System with a Synthesized Antenna Installed on a Spacecraft Near the Lunar Surface

Radar systems with an antenna with a synthesized aperture have been used successfully in recent years to chart the earth's surface with high resolution, approaching 3 to 4 miles [28, 76].

The high azimuth resolution of these systems is created by storing signals, and by coherent summing of these signals over a section of the flight trajectory equal in extent to the length of the large (synthesized) antenna in the system. The addition of signals arriving from a target at different times should be similar to the instantaneous summing in multielement broadside arrays. In these systems, therefore, the storing of the signal reradiated by a specific target considers its relative phase, and for this purpose the radar has a highly stable master oscillator that phases a high-frequency pulse transmitter and generates a reference voltage at the receiver phase detector.

High range resolution results from the use of very short pulses, $\sim$ 50 nanoseconds. The surface sections to be studied are selected on the subtarget line (subsatellite line) side because it is difficult to provide the required range resolution when ranges are short. The required range resolution is

$$\Delta D = \tau c/\cos\beta, \tag{3.40}$$

where

τ is the radiated pulse width;

β = arctan H/D;

β is the grazing angle;

H is the flight altitude;

D is the range to the target.

Target range changes as the target is illuminated, causing additional phase travel. This travel is less for long-range targets that for targets at shorter range, given the same buildup time. /84

Phase travel reduces the amplitude of the built-up signal. The amplitude of the built-up signal is decreased 10 percent, for example, when the target moves $\lambda/4$ in slant range. Consequently, from this point of view it is desirable to increase the scanning range. To do so, however, means increasing radar power, and this is not always possible.

The unfocused synthetic aperture(USA) compensates for the Doppler frequency of the target during its illumination by a real beam. Additional phase compensation for change in range to the target is added in systems with a focused synthetic aperture (FSA). Therefore, in the absence of phase destabilizing factors (of instability in the carrier frequency of transmitter and oscillation, non-linearity of flight in course and speed, oscillations of the vehicle relative to its center of gravity, and the like), the FSA system provides a longer coherent summing time as compared to a system without focusing. This, in turn, results in realization of high potential for the radar and provides better resolution.

If the width of the main lobe between nulls for conventional antennas is

$$2\theta = 2\lambda/D_A \text{(rad)}, \tag{3.41}$$

the limiting width of the main lobe for the USA is

$$2\theta_{(USA)min} = \sqrt{\lambda/D_t} \text{ (rad)}, \tag{3.42}$$

and for the focused

$$2\theta_{(FSA)min} = D_A/D_t \text{ (rad)}, \tag{3.43}$$

where

D_A is the antenna aperture, in meters;

D_t is the distance to the target, in meters;

The linear resolution of the target for these three systems will be, respectively [28, 76]

$$\Delta L = \theta D_t = \lambda D_t/D_A, \tag{3.44}$$

$$\Delta L_{(USA)max} = \theta_{(USA)} D_t = \frac{1}{2}\sqrt{\lambda D_t} \tag{3.45}$$

$$\Delta L_{(FSA)max} = \theta_{(FSA)} D_t = \frac{1}{2} D_A. \tag{3.46}$$

The limits of beamwidth for antennas with a synthetic aperture usually are so great that practical realization is impossible because of the many /85

destabilizing factors interfering with precise coherent summing of pulses over a long time span. The time limit for coherent buildup in a real system is determined by the time the relative phase travel of target signals reaches 180° for high frequency, with the resulting signal returning to 0.

If the requirement is for high azimuth resolution, and, as a result the obtaining of a longer coherent storage time, it is necessary to introduce rigid stabilization of the antenna array, as well as compensating signals when the spacecraft deviates from straight-line, uniform motion, as well as when it oscillates with respect to its center of gravity. The following additional equipment is installed in the spacecraft for this purpose: (1) an altimeter, for measuring the altitude and rate of change in altitude; (2) a Doppler measurer of the side and fore-and-aft components of the flight speed and drift angle; (3) a gyroscope system for measuring angles and the angular velocities of the spacecraft's oscillations with respect to the center of gravity; (4) an inertial system for measuring side and fore-and-aft accelerations.

The vertical antenna pattern for radars with a synthetic aperture is selected in the same manner as for on-board surface search radars. The vertical beam shape, in terms of energy, is selected as $F(\beta) = \operatorname{cosec}^2\beta$, where β is the grazing angle, in order to keep the echo signal amplitude from depending on range.

The beam maximum is the maximum range to the target when altitude is minimum.

The radar energy potential can be determined from

$$\frac{P_S}{P_N} = \frac{P_t G^2 \lambda^2 \sigma_0 \Delta R \, \Delta L F_r T_s}{(4\pi)^3 R^4 S k T N \Delta f}, \qquad (3.47)$$

where

G is the antenna gain for a real antenna;

ΔR is the range resolution, in meters;

ΔL is the linear azimuth resolution, in meters;

F_r is the repetition rate;

N is the receiver noise factor;

S is the transmission, reception, and processing signal loss;

Δf is the receiver pass band; T_s is storage time.

The following factors determine the signal loss: (1) reception and transmission losses in the antenna fairing and in the r-f line; (2) losses attributable to less than ideal coherent processing in the case of phase instabilities; (3) losses as the signal is propagated in the medium; (4) inaccuracies in the orientation of the antenna in terms of the normal to the line of flight because of oscillations in the carrier; and other factors.

Losses can total 15 to 17 dB. /86

Proposed characteristics for a radar with a synthetic aperture are listed below. This radar was to have been installed in the EROS artificial earth satellite [105]:

Wavelength, λ, cm	1.82
Beamwidth in vertical and horizontal planes $2\theta = 10^{\circ}$, with separate vertical and horizontal polarization	
Four-channel signal recording: vertical polarization; horizontal polarization; sum and difference of horizontal and vertical polarization	
Surface resolution, meters	30.5
Scanning band, km	10 x 600
Altitude of flight, km	320
Size of synthetic aperture, meters	15
Weight of solid-state elements, kg	74

The weight does not include the equipment for transmitting radar information to the ground measuring station.

The synthetic aperture radar provides a radar chart of a section of the surface on the subtarget line side, and makes it possible to evaluate change in reflectivity of individual sections of the surface studied. The absolute values of the reflectivity, σ_0, can be determined from Eq. (3.47) when absolute calibrations are made. This method, as distinguished from aerial photographic survey methods, is convenient because it does not require flying directly over the regions of interest to us, and can be used in cloudy weather and at night.

7. Pulse Modulation of the On-Board Transmitter of a Spacecraft near the Lunar Surface Receiving a Signal from the Earth

A great deal of information on the scattering characteristics of the lunar surface can be obtained by using a pulse transmitter on board an orbital spacecraft [44].

The ground reception complex will receive and record a direct signal from the transmitter, P_d, and the echo signal from the lunar surface, P_e. The direct signal is readily distinguishable from the echo when the spacecraft's altitude is $H > \tau c$, where τ is the transmitter pulse width (see Figure 3.12). The echo signal will be superimposed on the trailing edge of the received signal when $H < \tau c$ but the direct and echo signals can be distinguished from each other in many cases.

/87

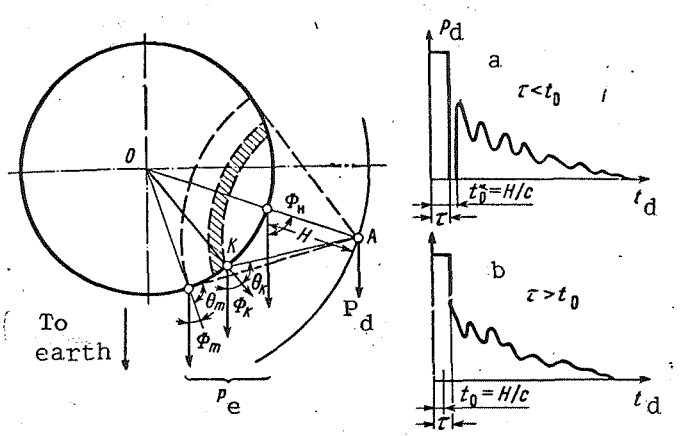

Figure 3.12. Reradiation of radio waves from the lunar surface in the case of pulse illumination by a spacecraft and reception of the signal on the earth.

Independent on-board synchronization, with positive synchronization of the recorder by the incoming direct signal, or positive synchronization of the on-board transmitter by the signal from the ground synchronizer, transmitted to the vehicle over the earth-vehicle radio communication line, can be used to provide definite synchronization between the commencement of recording and the leading edge of the direct signal. The timer, too, can synchronize the recorder. The latter mode was used in the experiment conducted with Luna 10, the artificial moon satellite.

A special delay circuit, supplying the signal for recorder synchronization, was used because of the delay in synchronization signals resulting from their propagation over the earth-vehicle radio communication line, the delay in signals in the processing and conversion circuit on board the satellite, and the delay in the transmitter signals resulting from their propagation from the artificial moon satellite to the ground receiver.

The pulse signal radiated by the transmitter illuminates part of the lunar surface, as shown in Figure 3.12. Only that part of the illuminated surface on the near side of the moon reradiated electromagnetic energy back to the earth.

The $P_{re} = f(t)$ relationships contain information on angles of incidence, θ, on aspect angles, Φ, and on the ratio of the intensities of reradiated and incident powers. The family of $P_{re} = f(t)$ dependencies are processed as follows.

The system of outer-trajectory measurements makes it possible to associate each oscillogram with the position of the spacecraft relative to the lunar surface; that is, to determine the altitude H, the coordinates of the subsatellite points (the latitude φ and longitude λ), the angle between the directions of spacecraft-moon and earth- ψ, as well as the components of the speed vector for the spacecraft in the direction moon-earth-V_x, and in the chart plane V_y, V_z. /88

The altitude, H, the distance from the artificial moon satellite to the point under consideration, K, on the surface, R_k, and the angle of incidence, θ_k, and the aspect angle, Φ_k, corresponding to this point, are associated with the delay in the reradiated signal relative to the leading edge of the direct signal by the following (see Figure 3.12)

$$R_k = t_k c, \tag{3.48}$$

$$H = t_0 c, \tag{3.49}$$

$$\theta_k = 90^\circ - \arccos\left(\frac{R_k^2 - 2aH + H^2}{2aR_k}\right), \tag{3.50}$$

$$\Phi_k = \psi - \arccos\left(\frac{(H+a)^2 + a^2 - R_k^2}{2(H+a)a}\right). \tag{3.51}$$

Eqs. (3.48) - (3.51) permit the use of data from outer-trajectory measurements to determine the corresponding incident and aspect angles for each t_k.

The illuminated surface, and the incident and aspect angles, change as the spacecraft moves in its orbit. The fact that the illuminating flux density is different for different sections of the illuminated surface must be taken into consideration in order to determine the properties of reradiation from the surface. This is associated with change in distance from the spacecraft to the section of the surface under study, as well as with different antenna gains in different directions, that is, with deviation of the onboard transmitting antenna pattern from isotropic. Consequently, normalization must be introduced for the echo oscillogram whereby the incident flux density for any section of the illuminated surface will be the same, or

$$P^{\bullet}_{\text{re}} = P_{\text{re}}(t)_k n_k. \tag{3.52}$$

The normalizing factor is in the form

$$n_k = G_p R_k^2 / G_k H^2. \tag{3.53}$$

The G_p/G_k ratio in the normalizing factor, n_k, is found quite readily when the real spatial antenna pattern for the satellite, and its orientation in space relative to the planet's surface, are known. Measuring the three-dimensional antenna patterns of spacecraft is an extremely complex and time-consuming task. The different types of objects within antenna pavilions cause secondary reradiation of electromagnetic energy from these objects during spacecraft antenna pattern measurements, and this results in a change in the antenna-medium match, and the superposition of the secondary radiation field on the measured field. All of this causes the measured pattern to differ from the real pattern. /89

A great many measurements are required to develop space patterns and the procedure usually can be replaced by one measuring patterns in several planes associated with the coordinates of the target axes. The number of such planes can vary from 2 to 16.

Orientation of the axes of artificial satellites in space can be as follows, depending on the mission: (1) rigid orientation in absolute space for all three axes; (2) rigid orientation of one of the axes relative to the local vertical for the planet, and of the other two axes relative to the target's speed vector (to the plane of the orbit); (3) twist of the satellite

relative to the axis with the maximum moment of inertia; (4) twist of the satellite relative to the direction to the sun.

The outer-trajectory measurements provide the nature of the movement of the satellite's center of gravity. Data on its movement relative to the center of gravity can be obtained uniquely only by some sort of autonomous equipment installed in the satellite. Examples of instruments such as these include different types of verticals using optics, infrared, electronic, or gravitational techniques. These instruments provide the direction of the local vertical with respect to the satellite's coordinate axes.

If the satellite is carrying cameras, the position of the satellite's axes relative to the surface of the planet can be determined from a series of photographs of the surface made in synchrononism with radar measurements. While extremely complex, this method is very useful because radar measurements can be tied with surface relief and, at the same time, increase the information available on surface physical properties.

If the space pattern for the satellite's antenna is unknown, or if the instantaneous position of its coordinates relative to the surface of the planet is unknown, the G_p / G_k ratio can be established only when the satellite is rotating about its axis rapidly enough as it moves in orbit, by averaging the measurements of direct and reradiated signals during the period of satellite rotation. The period of the satellite's rotation about its axis should not exceed the time of significant change in the geometry of surface illumination, or in the properties of the illuminated surface. /90

Introducing averaged $P_{re} = f(t)$ for the time exceeding the satellite's period of rotation relative to its axis can eliminate the dependence of the factor n_k on the instantaneous change in the G_p/G_k ratio. Primary processing of measurements provides the set

$$P^{\bullet}_{re} = f(R_k). \tag{3.54}$$

R_k in turn is a function of incidence and aspect angles, found by using Eqs. (3.50) and (3.51), resulting in a set

$$P^{\bullet}_{re} = f(\theta_k, \Phi_k). \tag{3.55}$$

Simultaneous handling of the set of dependencies in Eq. (3.55) when Φ = constant, or θ = constant, yields the set

$$P^{*}_{\text{re}\,n} = f(\theta_k) \text{ when } \Phi_n = \text{const} \quad (\text{con}\,n = 0 \text{---} 90^\circ), \quad (3.56)$$
stant

$$P^{*}_{\text{re}\,m} = f(\Phi_k) \text{ when } \theta_m = \text{const} \quad (\text{con}\,m = 0 \text{---} 90^\circ). \quad (3.57)$$
stant

Normalization provides the scattering indicatrix for the surface

$$i_n(\theta_k, \Phi_k) = \frac{P^{*}_{\text{re}\,n}}{(P^{*}_{\text{re}\,n})_{\max}} = \frac{f(\theta_k)}{[f(\theta_k)]_{\max}} \quad \text{when } \Phi_n = \text{constant} \quad (3.58)$$

or

$$i_m(\theta_k, \Phi_k) = \frac{P^{*}_{\text{re}\,m}}{(P^{*}_{\text{re}\,m})_{\max}} = \frac{f(\theta_k)}{[f(\Phi_k)]_{\max}} \text{ when } \theta_m = \text{constant} \quad (3.59)$$

Simultaneous handling of the set of dependencies in Eq. (3.55) when Φ = θ = constant, provides the surface backscattering pattern

$$B(\theta) = \frac{P_{\text{re}\,l}(\theta_k)}{[P_{\text{re}\,l}(\theta_k)]_{\max}} \quad \text{when} \quad \theta_k = \Phi_k. \quad (3.60)$$

By comparing the direct and reradiated signal strengths we can find the albedo of the surface layer and the reflectivity. Surface layer albedo can be found from Eqs. (2.126) and (2.127).

The surface reflectivity for normal incidence, after the corresponding calculations, is /91

$$\sigma_{0N} = \frac{\bar{P}_{\tau\,\text{re}}}{\bar{P}_{\tau\,\text{rec}}} \frac{G_d}{G_p} 2 \frac{H^2}{ac\tau i(\Phi_p)}, \quad (3.61)$$

where

$\bar{P}_{\tau\text{re}}$ and $\bar{P}_{\tau\text{d}}$ are the P_{re} and P_d values, found by using the formulas

$$\bar{P}_{\tau\text{re}} = \int_0^{\tau} P_{\text{re}}(t)\,dt \quad [\text{in the range interval from } H \text{ to } (H + c\tau)], \quad (3.62)$$

$$\bar{P}_{\tau\,\text{d}} = \int_0^{\tau} P_{\text{d}}(t)\,dt. \quad (3.63)$$

G_p and G_d are the on-board antenna gains in the directions of the local vertical and the ground observer. Φ_a is the aspect angle for the subsatellite point.

A radar chart of the planet's surface can be compiled by finding $\sigma_{0\,N}$ for each subsatellite point during the satellite's movement in its orbit. Surface resolution can be established by the size of the simultaneously illuminated scatterer near the subsatellite point

$$R_{p1} \approx \sqrt{ac\tau}. \qquad (3.64)$$

Mutual processing of the $P_{re} = f(t)$ oscillograms can increase the resolution found from Eq. (3.64) several times.

8. Monochromatic Radiation from the On-Board Transmitter of a Spacecraft near the Lunar Surface with Signal Reception on the Earth

The angles between the direction of the speed vector and the directions to area dS on the lunar surface, as well as the angle between the speed vector and the direction satellite-ground measuring point, will change as the artificial moon satellite moves. Consequently, when the on-board transmitter emits a continuous monochromatic signal, the direct signal and the signal reradiated from the lunar surface received on the ground will, in the general case, have different frequencies, differing from radiation frequency by the corresponding Doppler frequencies, which can be determined from the known formula /92

$$f_{di} \simeq \frac{V_{ri}}{c} f_0 = \frac{Vf_0}{c} \cos \alpha_i, \qquad (3.65)$$

where

α_i is the angle between the direction of the speed vector and the corresponding direction to the ground point, or surface section;

V is the modulus of the satellite's speed vector;

f_0 is the carrier frequency.

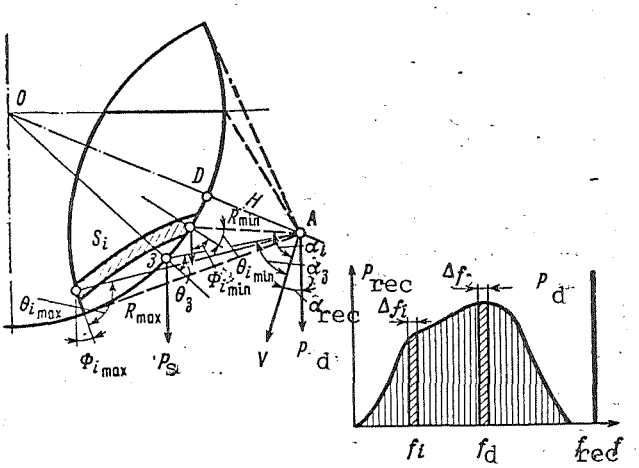

Figure 3.13. Reradiation by the surface for monochromatic illumination from a space vehicle and reception of the signal on the ground.

Based on Figure 3.13, $\alpha_i = \alpha_{rec}$ for the direct signal, $\alpha_i = \alpha_{ik}$ for the signal reradiated by area ΔS_k, and so on.

That part of the lunar surface visible from the earth and which is, simultaneously, illuminated by the on-board transmitter through the antenna array, participates in producing the echo received on the ground. But the echo will contain the whole spectrum of frequencies, the width and shape of which will depend on the properties of the scatterer (its scattering indicatrix), as well as on the range of angles between the direction of the speed vector for the satellite and the direction to the edge of the illuminated region.

The direct signal has but one spectral line. Spectrum difference, as well as amplitudes, is what makes it possible to separate the direct and echo signals at the reception point on the ground. Analysis of the echo spectrum is extremely complicated. Readily seen is the fact that echoes from that region of the lunar surface that can be determined by the lines of intersection of the spherical lunar surface with two concentric cones with a common apex at the point where the satellite is located, and the axis of /93 which coincides with the direction of the satellite speed vector, will correspond to a constant Doppler frequency. The difference in angles at the apex of these cones determines the resolution of the system in terms of Doppler frequency and transmitter radiation spectrum. It can be shown that the difference in angles at the apex of these cones, $\delta\alpha_k$, can be found from

$$\delta\alpha_k = 2\arcsin\frac{\delta f d_\Sigma c}{2Vf_0\sin\alpha_k}, \qquad (3.66)$$

where $\delta f d_\Sigma$ is the summed resolution for the system, determined by the resolution of the measuring arrangement used with the spectrum analyzer, by the instability in the local oscillator frequency, by the width of the transmitter spectrum, and by certain other factors.

It is important to note that the angle of incidence and the aspect angle will differ for a fixed position of the satellite in orbit at points along the line of intersection of sphere and cone. Hence, study of the spectrum will not derive analytical relationships between Doppler frequency in the spectrum and the angle of incidence, or aspect angle.

Strictly speaking, therefore, analysis of the echo spectrum will not yield the scattering indicatrix, or the backscattering pattern. However, recognizing that the effectiveness of reradiation from different sections of an illuminated surface is not the same, one can make a quantitative evaluation of the nature of the reradiation from the lunar surface with a different error for different on-board transmitter wavelengths, as will be pointed out below.

This evaluation is readily made for the case of scattering of radio waves by the surface of the planet in accordance with a law close to the specular reflection law for optical radiation. In this case, the echo spectrum will contain but two components with Doppler frequencies, respectively $f_{d_{direct}}$ and f_{d_s}.

In this case, the Fresnel coefficient can be found from the relationship that exists between the strengths of the direct and the reradiated signals at the receiver input

$$\frac{P_{re}}{P_d} = \frac{G_{re}}{G_d} \rho_s \alpha_k, \tag{3.67}$$

where

α_k is the divergence factor.

The formula for the divergence factor, Eq. (2.23), can be simplified when the signal is radiated from the satellite and received on earth, to become

$$\alpha_k = \frac{a \cos \theta_k}{R_k + a \cos \theta_k}, \tag{3.68}$$

where

R_k is the distance from the satellite to the area on the lunar surface under investigation;

θ_k is the angle of incidence of a wave at this area.

In the specular reflection case $R_k = R_s$, and $\theta_k = \theta_s$. It can be shown that R_s and θ_s are linked with the altitude of the satellite above the surface, H, and by the angle earth-moon-satellite, φ_A, by /94

$$\operatorname{tg}(2\theta_s - \varphi_A) = 2 \operatorname{tg} \theta_s, \tag{3.69}$$

$$R_s = (a + H) \frac{\sin(\varphi_A - \theta_s)}{\sin \theta_s}. \tag{3.70}$$

The ratio of satellite transmitting antenna gain in the direction of specular reflection and in the direction of the ground point (G_{re}/G_d), is found by using the procedure described in the preceding paragraph.

So, by measuring the ratio of reradiated and direct signal strength at the receiver input we can find the Fresnel coefficient, ρ_s, and its dependence on the angle of incidence. But, because it is not a point, but some region of the surface with an elliptical shape that produced the echo, its spectrum will not be monochromatic, even for specular reflection. Eqs. (2.17) and (2.18) can be used to find the dimensions of the ellipse. Calculations show that when λ = 30 cm, the orbital speed is V = 2 km/sec, satellite altitude is H = 400 km, and angle of incidence θ = 45° (φ = 26.5°), the size of the area producing the echo will be 1 km x 1.5 km for specular reflection, and that the width of the Doppler spectrum will be 3.3 Hz, or $7 \cdot 10^{-4} f_0$. But, because the lunar surface scatters in accordance with a law different from the specular reflection law, the actual size of the scatterer will be larger, and can be estimated from the change in power spectral density with frequency.

Measuring $f_{d_{min}}$ and $f_{d_{max}}$, in the echo spectrum (we assume a power level equal to 0.1), we find α_{min} and α_{max} corresponding to them from Eq. (3.65).

The Doppler frequency, f_{d_i}, will correspond to some zone, S_i, on the lunar surface for which α_i = constant. The angles of incidence, θ_i, and the aspect angles Φ_i, corresponding to them, in this zone will change from $\theta_{i_{min}}$ to $\theta_{i_{max}}$, and from $\Phi_{i_{min}}$ to $\Phi_{i_{max}}$, but it is not mandatory that $\Phi_{i_{min}}$ have the maximum of all values for the corresponding f_{d_i}. The following equations can be used to find $\theta_{i_{min}}$ and $\Phi_{i_{min}}$

$$\alpha_i + \alpha_{rec} = 180° - (\theta_{i_{min}} + \Phi^*_{i_{min}}), \tag{3.71}$$

$$\frac{a+H}{\sin\theta_{i_{min}}} = \frac{r_a}{\sin(\theta_{i_{min}} + \Phi^*_{i_{min}} - \varphi_A)}. \tag{3.72}$$

Here $\Phi_{i_{min}}$ is the angle between the projection of the aspect line in the plane of the orbit of the satellite and the local vertical passing through point Q on the lunar surface. $\theta_i = \theta_{i_{min}}$ for this point (see Figure 3.13). Φ_i is the angle between the aspect line and the local vertical passing through point Q on the lunar surface. /95

Eqs. (3.71) and (3.72) provide ready positions of points on the lunar surface corresponding to $f_{d_{min}}$ and $f_{d_{max}}$ for which $\theta = \theta_{min}$, and, correspondingly, $\Phi^* = \Phi^*_{min}$. Eq. (3.69) can be used in the same manner to find the position of the "mirror" point, M, for which θ_m and Φ_m are equal. The center of the scatterer will coincide with this point. Its radius can be estimated, roughly, from

$$r = \frac{a}{2}\left[\Phi^*_{min\,(for\,\alpha_{max})} - \Phi^*_{min\,(for\,\alpha_{min})}\right]. \tag{3.73}$$

A more precise estimate of the size of the scatterer can be obtained as follows. Assuming that the characteristics of the echo from the illuminated region on the lunar surface coincide with similar averaged characteristics for the whole of the visible area, we can find the region of angles of incidence $\Delta\theta$, for which $B(\theta) > -10$ dB from the backscattering pattern. We can find the maximum angles of incidence for each Doppler frequency in the spectrum, f_{d_i}, considering that

$$\theta_i = \theta_{i_{min}} - (\theta_{i_{min}} + \Delta\theta). \tag{3.74}$$

This expression establishes the coordinates on the line on the lunar surface for f_{d_i}, points along which help produce the reradiated signal. Performing a like operation for all Doppler frequencies in the spectrum from $f_{d_{min}}$ to $f_{d_{max}}$, we obtain the region on the lunar surface producing the reradiated signal. This can be done in the case of the moon in the meter and decimeter bands, where the backscattering pattern is narrow, and the reradiation region small.

The reradiation region broadens out in the centimeter band, and it no longer is possible to take the divergence factor as constant for the different points in this region. There is, in this band, a significant rise in the diffuse component in the echo, and since the divergence factor is correct only for the specular reflection mechanism, that is, for the quasi-specular component of the echo, use of this procedure in the lower part of the centimeter band can only provide an estimate. Change in the divergence factor for different angles α must be taken into consideration, therefore, when calculating α_{min} and α_{max} in terms of the magnitude of the relative echo spectral density. This signal spectrum provides the scatter region on the lunar surface, and, by using Eq. (3.75), an estimate of the averaged value of the /96

reradiation coefficient in the direction of the observer. This coefficient can be found from the ratio of the integral echo spectrum power to the direct power

$$\rho_{int} = \frac{\int_{f_{d\min}}^{f_{d\max}} P_{re}(f_d)\, d(f_d)}{P_d} \frac{G_d}{\bar{G}_{re}} \frac{1}{\bar{\alpha}}, \tag{3.75}$$

where

$$\bar{G}_{re} = \frac{1}{\alpha_{\max} - \alpha_{\min}} \int_{\alpha_{\min}}^{\alpha_{\max}} G(\alpha)\, d\alpha; \tag{3.76}$$

$$2\bar{\alpha} = \alpha_{\max} + \alpha_{\min} = \frac{a\cos\theta_{\max}(\alpha_{\max})}{R_{\max} + a\cos\theta_{\max}(\alpha_{\max})} + \frac{a\cos\theta_{\min}(\alpha_{\min})}{R_{\min} + a\cos\theta_{\min}(\alpha_{\min})}. \tag{3.77}$$

By finding ρ_{int} for different points along the trajectory, we can construct the dependence of this parameter on the angle of incidence.

Thus, the use of CW by the satellite enables us to establish the size of the echo-producing area on the surface, and to estimate the integral reradiation coefficient for that area, that is, to perform radar charting of the surface from an artificial planetary satellite.

CHAPTER IV

/97

RESULTS OF RADAR INVESTIGATIONS OF THE CHARACTERISTICS OF REREADIATION FROM THE MOON USING GROUND RADARS AND SPACE VEHICLES

1. Results of the Measurement of the Radar Cross Section of the Visible Part of the Lunar Surface from Ground Investigations

The first radar investigations of the moon were made in 1946, using a specially rebuilt long-range radar at a wavelength of 2.6 meters [65, 148, 173]. These measurements resulted in detection of a signal reradiated from the lunar surface, and in a rough approximation of the distance from the earth to the moon. However, lack of a modern system for processing the signal made it impossible to determine lunar reradiation characteristics.

Over the last 20 years, radar investigation of the moon from the earth has taken place at over 20 wavelengths in the band between 0.86 cm and 20 m. These measurements were not equivalent. They were, however, made over so broad a band, determined by the atmospheric radio window, that it was possible to evaluate the electromagnetic properties of the lunar surface in the r-f region. And processing the reradiation characteristics provided an estimate of many physical characteristics of the surface, and of the surface layer.

The most completely investigated facet during radar measurements of the moon from the ground was the relationship between the radar cross section, σ, and the wavelength, because σ is readily determined from the ratio of the echo power at the ground receiver input to the power radiated by the radar. And, as has been stipulated, σ is determined only for the polarizing component of the incoming signal.

The overwhelming majority of measurements was made of the polarizing component during reception because the power of the depolarizing component is much less than that of the polarizing, and the majority of the radars used for lunar investigation either cannot receive two-polarization signals, or

lack the energy potential needed to receive the depolarizing component. Reception of signals reradiated from the moon with two polarizations was accomplished at but two wavelengths (23 and 68 cm). /98

Measurement of the magnitude of the radar cross section has been taken to refer to an area of the lunar disk equal to

$$S_{\text{disk}} = \pi a^2 = 9{,}49 \cdot 10^{12}\ \text{m}^2. \qquad (4.1)$$

Table 4.1 lists data on the relationship for the band of wavelengths between 0.86 and 19.2 meters. The accuracies listed in the table are those cited by the authors in the corresponding references, or are taken conventionally as equal to ±3 dB.

TABLE 4.1

Wavelength, cm	$\sigma/\pi a^2$	Measurement accuracy, dB	Author	Year of measurement
0.86	0.07	±1	Linn et al. [144]	1961
3.0	0.07	±1	Kobrin [31]	1957
3.6	0.07	±1.5	Murray et al. (see [109])	--
3.6	0.04	±3	Evans and Pettengill	1963
10.0	0.07	±1	Kobrin [31]	1954
10.0	0.05	±3	Hughes [132, 133]	1961
12.5	0.0022	±3 *	Victor et al. (see [109])	1961
23	0.065	±0.5	Evans and Hagfors [110]	1965
33.5	0.09	±3 *	Aarons [109]	1959
61.0	0.05	±3	Blevis and Chapman (see [109])	1960
68.0	0.74	±3 *	Pettengill (see [109])	1960
73.0	0.074	±1	Fricker et al. (see [109])	1960
75.0	0.1	±3 *	Leadbrand [109]	1959
100.0	0.07	±4	Treksler [70]	1958
149.0	0.07	±3 *	Aarons [109]	1959
150.0	0.08	±4	Treksler [70]	1958
185.0	0.07	--	Getmantsev et al. [21]	1964

* Accuracy conventionally taken as equal to ±3dB [59, 109]

TABLE 4.1 (continued)

Wavelength, cm	$\sigma/\pi a^2$	Measurement accuracy, dB	Author	Year of measurement
199.0	0.05	±3 *	Webb [173]	1946
250.0	0.1	±3	Evans [80]	1957
300.0	0.1	±3	Evans et al. [59]	1959
600.0	0.1	±1	Hagfors [77]	1968
784.0	0.06	±5	Evans and Ingalls (see [106])	1962
1130.0	0.19	+3 -2	Davis and Rohlfs [103]	1964
1560.0	0.13	+3 -2	Davis and Rohlfs [103]	1964
1920	0.16	+3 -2	Davis and Rohlfs [103]	1964

* Accuracy conventionally taken as equal to ±3 dB [59, 109]

The magnitude ±3 dB corresponds to the average accuracy in determining the energy potential of receivers and transmitters for a communication line, using modern methods to calibrate receiver-transmitter tracts. /99

Reference [39], after processing σ values measured in the centimeter, decimeter, and meter bands, introduces the dependence of the mean value of the radar cross section of the lunar surface on the wavelength (Figure 4.1). As will be seen, the radar cross section in the r-f range increases with increase in the wavelength. The radar cross section changes from 0.06 πa^2 to 0.16 πa^2 with change in wavelength from 0.86 cm to 19.2 m, and measurement accuracy is ±(0.5-5) dB.

The $\sigma/\pi a^2$ values listed in Table 4.1 and shown in Figure 4.1 are for the case when the entire surface of the visible part of the moon takes part simultaneously in producing the power of the reradiated flow. The radar transit of the moon is 11.6 msec.

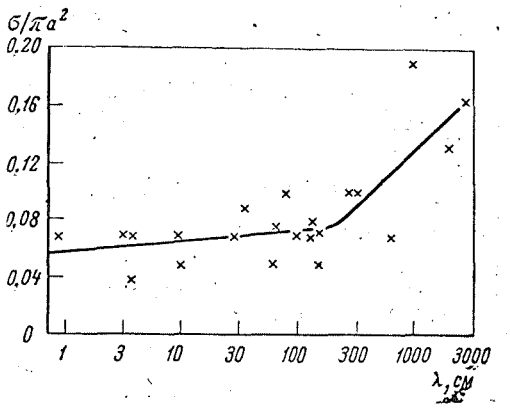

Figure 4.1. The ratio of the radar cross section of the moon to the area of its disk ($\sigma/\pi a^2$) in terms of wavelength λ. The crosses are plots of the measurements (disregarding the accuracy indicated in Table 4.1).

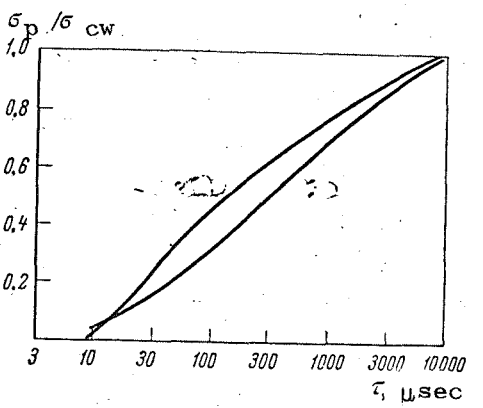

Figure 4.2. Reduction in the radar cross section of the moon when the width of the transmitted pulse, τ, from the ground radar is shortened (modulation losses). The upper curve is for λ = 150 cm, the lower for λ = 68 cm.

In the case of pulse modulation of the ground radar with a pulse width /100
shorter than 11.6 msec, the simultaneously illuminated surface of the moon will be less than the surface of its visible part, and this will result in a reduction in the magnitude of the flux of electromagnetic energy reradiated in the rearward direction. This is equivalent to reducing the radar cross section. Reduction in σ when the transmitted pulses are shortened has been

designated modulation losses. The magnitudes of modulation losses at λ = 68 cm [107, 109], and at λ = 150 cm [59, 70], are shown in Figure 4.2.

2. Results of Determining Backscattering Patterns for the Visible Part of the Lunar Surface from Ground Measurements

Illumination of the lunar surface by high-frequency pulses with a width of the order of a few microseconds resulted in obtaining relationships between echo strength and delay time, τ, in terms of the appearance of the first echo from the point on the lunar surface closest ("from the tip of the moon") to the ground radar. These relationships were measured at wavelengths of 0.86, 3.6, 10, 23, 68, 600, and 1130 cm, and are shown in Figure 4.3 [103, 107, 109, 110, 131, 139, 143, 144].

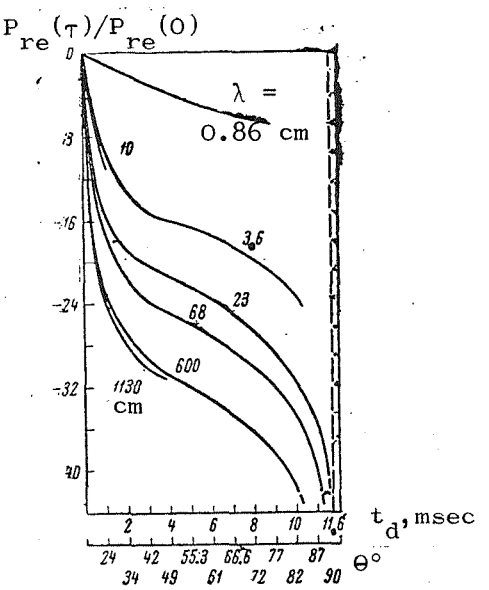

Figure 4.3. Power reradiated by the moon in terms of signal delay time with respect to the point on the moon closest to the ground observer.

The association between the angle of incidence, θ, and the delay, τ, for a spherical surface can be expressed by the formula

$$\theta = \arccos\left(1 - \frac{c\tau}{2a}\right). \qquad (4.2)$$

This formula makes it simple to convert $P_{re} = f(\tau)$ to $P_{re} = f(\theta)$.

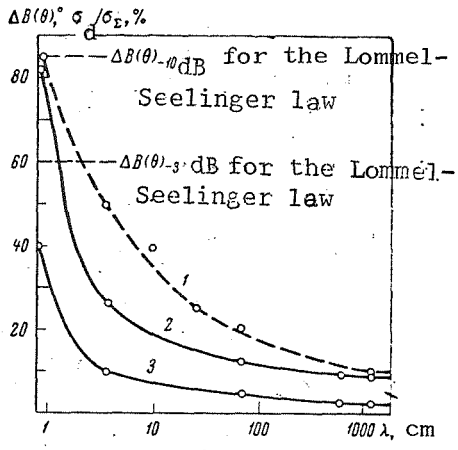

Figure 4.4. Width of backscattering pattern and relative power of the diffuse component in the echo. Circles are the plots of calculations for experimental backscattering patterns for the moon.

1 - diffuse component of the echo, σ_d/σ_Σ;
2 - width of backscattering pattern at the -10 dB level;
3 - width of the backscattering pattern at the -3 dB level.

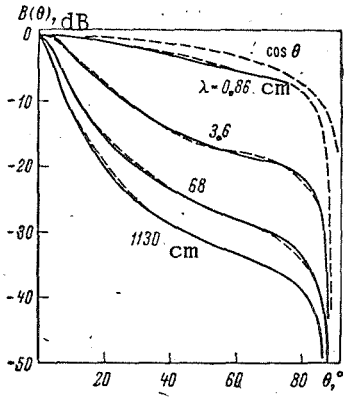

Figure 4.5. Backscattering patterns. The dashed line curves are experimental. The solid line curves were constructed using Beckmann's formula, Eq. (2.58).

As will be seen from Figures 4.4 and 4.5, the backscattering pattern narrows with increase in wavelength, and this can be evaluated as an increase in the echo of the quasi-specular component relative to the diffuse component.

The calculations often required the availability of a mathematical approximation of the backscattering pattern, measured experimentally. This approximation can be made by selecting known functions with constant coefficients, and this was done for six backscattering patterns (individually for the quasi-specular and diffuse components.

The approximating functions, and the range of angles of incidence, for which these functions are valid, are given in reference [39] (see Table 4.2).

Relatively wide transmitted pulses ($\tau > 10$ sec) have been used during /101
radar investigation of the moon from the ground in order to provide the necessary S/N excess for the planetary radar.

The angles of incidence between 3^o and 5^o therefore were not investigated. Instead, the moon's backscattering pattern between these angles, established experimentally, was plotted by extrapolating echo values from $\theta > 5^o$ to angles of incidence $\theta < 5^o$.

As will be seen from Table 4.2, the approximating law for the quasi-specular component differs for each wavelength and does not take in all angles of incidence, thus making for definite difficulties in the practical application of these approximations. It will be shown below that these drawbacks can be eliminated by using the approximating backscattering pattern for the moon and Beckmann's formula.

Consideration of the moon's backscattering patterns must include the /102
fact that the accuracy with which they are plotted is determined by the width of the transmitted pulse because change in pulse width causes a simultaneous change in the magnitude of the surface area illuminated and in the range of angles of incidence for this area.

The results of experiments at 68 cm (see Table 4.2) show that change in the transmitted pulse width causes a change in the measured backscattering pattern. So it is desirable to select the width of the transmitted pulses such that angles of incidence at a simultaneously illuminated surface do not differ greatly from each other (no more than 1^o to 2^o). Now the accuracy with

TABLE 4.2

Wavelength, cm	Specular component		Diffuse component		Author	Year
	formula	range of angles of incidence θ°	formula	range of angles of incidence θ°		
0.86	--		$\cos\theta$	50 - 90	Linn, Sohigian, Crocker [143, 144]	1961
3.6	$\exp(-7.1\sin\theta)$ $\tau = 30$ μsec	5 - 18	$\frac{1}{160}\cos^{3/2}\theta$	60 - 90	Evans, Pettengill [107]	1963
3.6	$\frac{1}{1+50\,\theta^2}$ (θ, rad)		Same		Evans, Pettengill [107]	1963
10	$\exp(-10.2\,\theta)$(θ, rad) $\tau = 12$ μsec	4 - 13	$\frac{1}{160}\cos^{3/2}\theta$		Hughes [132]	1961
68	$\exp(-15.3\sin\theta)$ $\tau = 12$ μsec	3 - 9	$\frac{1}{150}\cos\theta$	80 - 90	Evans [107a]	1963
	$\exp(-12.5\sin\theta)$ $\tau = 30$ μsec	5 - 12	$\frac{1}{150}\cos^{3/2}\theta$	45 - 80		
68	$\exp(-10.5\sin\theta)$ $\tau = 65$ μsec	7.5 - 60	$\frac{1}{150}\cos^{3/2}\theta$		Evans, Pettengill, Henry [155]	1962
68	$\frac{1}{1+46\,\theta^2}$(θ, rad)		$\frac{1}{150}\cos^{3/2}\theta$		Evans, Pettengill, Henry [155]	1962
75	$\exp(-10.5\sin\theta)$ $\tau = 70$ μsec	7 - 50	$\frac{1}{160}\cos^{3/2}\theta$	50 - 90	Pettengill [155]	1960
75	$(\frac{\sin\theta}{\theta})^{20\pm6}$ ±0.1		--		Leadbrand, Dyce et al. [142a, b]	1959
250	$\cos^{30}\theta$	0 - 90			Evans	1957

which the backscattering pattern can be plotted will be ±0.5 dB.

Beckmann's efforts (see #2, Chapter II) have made it possible to provide a universal approximating function for the moon's backscattering pattern in the band between 0.86 cm and 10 m [89, 93], valid for the lunar surface, as well as for the surface of Venus (the difference between it and the experimental backscattering patterns is a maximum of ±1 dB).

Figure 4.5 shows backscattering patterns, measured experimentally, and patterns plotted for these same wavelengths using Beckmann's formula [93, 109, 110]. Figure 4.6 shows backscattering patterns for the moon calculated using Beckmann's formula for wavelengths at which no backscattering pattern measurements were made.

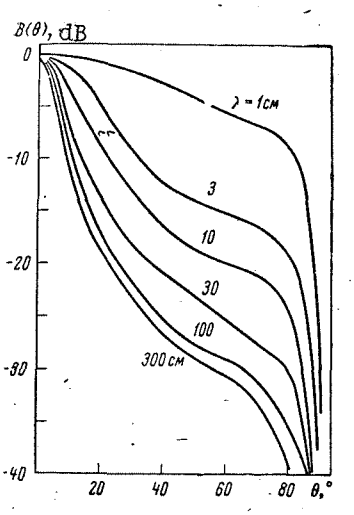

Figure 4.6. Calculated backscattering patterns for the moon.

3. Results of the Determination of the Reflectivity for the Normal Incidence Case from Data from Ground Radar Measurements /104

It is impossible to make a direct determination of the reflectivity, $\sigma_{0\,N}$, for the normal incidence case from ground radar observations. It can be determined only by the simultaneous processing of the results of radar of the radar cross section for the region investigated, and its backscattering pattern. And it is impossible, naturally to determine $\sigma_{0\,N}$ in small areas because of the narrow space-time selection available to ground radars (the

angular size of the moon from the earth is ~30°). This is why the calculations use the averaged value of the reflectivity, $\overline{\sigma}_{0N}$. Its magnitude can be found from Eq. (2.117), and the numerical solution requires specification of an integral of the $\int_0^{\pi/2} B(\theta)\sin(\theta)d\theta$ type, something that can be done only if the mathematical approximation of the backscattering pattern for the particular wavelength is available.

As we have pointed out, this approximation can be expressed by a law in the following form for the moon at centimeter, decimeter, and meter wavelengths

$$B(\theta) = (\cos^4\theta + C\sin^2\theta)^{-3/2}\exp\left[-\frac{1}{4}\operatorname{tg}\theta\operatorname{erfc}(K\operatorname{ctg}\theta)\right]. \qquad (4.3)$$

This formula was verified between 0.86 cm and 11.3 m. Figure 4.7 shows σ_{0N} values calculated for wavelengths between 0.86 cm and 2.5 m. Backscattering patterns, plotted using Eq. (4.3), and the C and K coefficients in reference [93], were used to calculate σ_{0N} values.

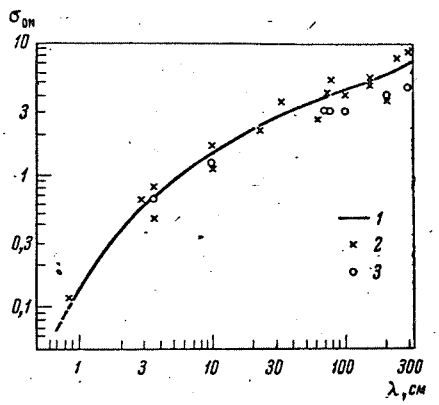

Figure 4.7. Reflectivity, averaged for the lunar disk. The crosses are plots of the calculations made using the data in Figure 4.1, and the circles those for the data in [41, 131].

The values for the radar cross section of the visible part of the lunar surface were taken from [39], where they were obtained by processing a great many σ values, measured experimentally using the least squares method. /105

Figure 4.7 is the plot of σ_{0N} values obtained in [41, 131] for an approximation of the backscattering pattern by other laws, ones differing from

Beckmann's law. The backscattering pattern approximations used in [41, 131] are valid only for specific wavelengths, but their use greatly simplifies solution of the integrals in Eq. (2.117) and at the same time simplifies determination of $\bar{\sigma}_{0\,N}$.

The accuracy with which $\bar{\sigma}_{0\,N}$ is determined is ±(3-4) dB, according to [41, 42, 131]. Increase in $\sigma_{0\,N}$ with increase in wavelength is regular because the specular nature of the reradiation increased with increase in the wavelength, which, in the normal incidence case, results in an increase in the rearward reradiated power, that is to a narrowing of the backscattering pattern, and to an increase in $\bar{\sigma}_{0\,N}$.

4. Ground Polarization Measurements of an Echo from the Moon

Illumination of a smooth surface by a wave with circular polarization results in a reflected wave with circular polarization with the opposite direction of rotation of the plane of polarization. But, when a rough surface is illuminated by a wave with circular polarization, the echo will have a circular polarization with two components, one of which will have the opposite direction of rotation of the plane of polarization (the polarized component), the other the same direction of rotation of the plane of polarization (depolarized component), with respect to the direction of rotation of the plane of polarization of the signal transmitted by the radar. The magnitude of the depolarized component of the echo will characterize the degree of roughness of the illuminated surface.

Polarization measurements also can be made during target detection by /106
transmitting radio waves with linear polarization. What occurs is reception of radio waves with two orthogonal polarizations, one of which has the same plane of polarization as that of the transmitted wave. Polarization measurements during radar detection of the moon have been made at two wavelengths, 23 and 68 cm. The 23 cm experiment was carried out for circular, as well as for linear, polarization, that at 68 cm for circular polarization only. Figures 4.8 - 4.11 show the results. Figures 4.8 and 4.9 show echo strength in terms of delay time for the depolarized component. Figure 4.10 shows the

polarization factor in terms of the delay for circular polarization, and Figure 4.11 that for linear polarization.

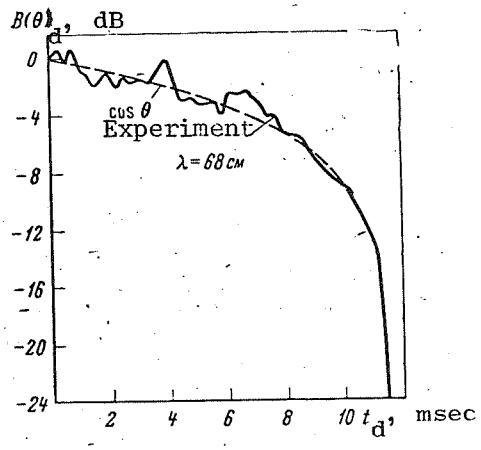

Figure 4.8. Power of depolarized component in terms of delay time when λ = 68 cm.

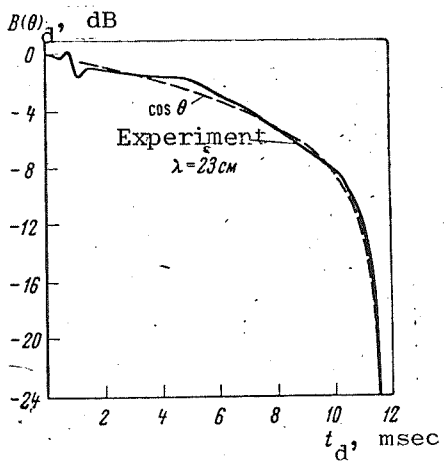

Figure 4.9. Power of depolarized component in terms of delay time when λ = 23 cm.

The polarization factor can be determined from

$$\Pi = \frac{P_p - P_d}{P_p + P_d} \cdot 100\%, \qquad (4.4)$$

where

P_p is the power of the polarized component;

P_d is the power of the depolarized component.

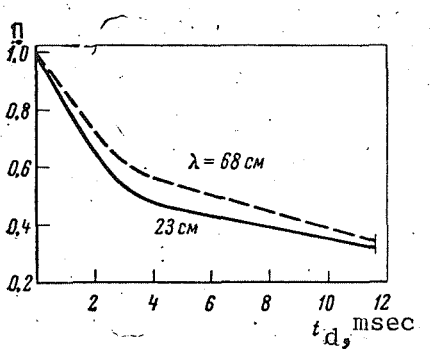

Figure 4.10. Polarization factor in terms of delay time for echo with circular polarization and reception of echo with two circular polarizations with rotations in opposite directions.

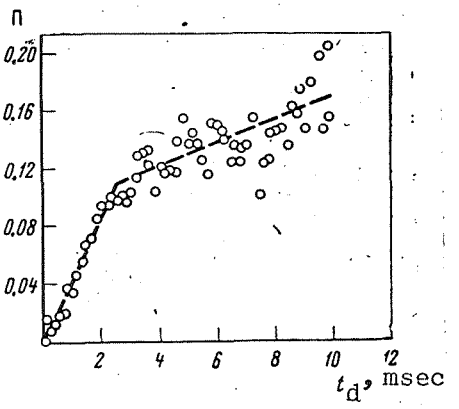

Figure 4.11. Polarization factor in terms of delay time when radiation is of a linearly polarized signal and reception is of an echo with two orthogonal linear polarizations (λ = 23 cm, τ = 200 μsec).

The approximation of the backscattering pattern for the depolarized components at both wavelengths (23 and 68 cm) coincides with the cos θ law, which corresponds to a uniformly bright disk (the Lommel-Seelinger law). A comparison of polarized and depolarized components when polarization is circular shows that the ratio of echo strengths in the two components is identical for 23 cm and 68 cm, and equals 3.

Measurement of echo strength ratio for two orthogonal polarizations when λ = 68 cm shows that in the region in which the diffuse component of the echo prevails (from 3 to 11.6 msec) approximately 12.5 percent of the total echo strength is found in the component with orthogonal radiated polarization.

5. Measurement of Reflectivity during the Landing of Luna 9 and Luna 13 on the Lunar Surface

Experiments designed to study the properties of reradiation from the moon's surface layer in the r-f region were carried out by certain of the space vehicles launched into circumlunar space. These measurements, in the majority of cases, were operational in nature and were designed to evaluate the operability of transceivers carried by the spacecraft, and were not in pursuit of scientific goals. Nevertheless, the results provided valuable /108 data on the properties of the lunar surface layer. Experiments of this type were carried out by the Soviet space vehicles Luna 9, Lune 10, Luna 11, Luna 12, Luna 13, and Luna 14, and, judging from the published data, by the American vehicles Surveyor 1, Surveyor 3, Surveyor 5, Surveyor 6, Surveyor 7, Lunar Orbiter 1, and Explorer 35.

These experiments were carried out in accordance with one of two cited plans:

1. by Luna 9, Luna 13, Surveyor 1, Surveyor 3, Surveyor 5, Surveyor 6, and Surveyor 7, all of which landed on the lunar surface: emission, reception of echoes from the surface, and processing on-board;

2. by Luna 10, Luna 11, Luna 12, Luna 14, Lunar Orbiter 1, and Explorer 35: signals emitted by transmitters carried by the vehicles, with reception and processing at ground measuring stations.

Let us review the results obtained during the experiments carried out during the flights of Luna 9 and Luna 13. Special 3 cm radars were installed in these automatic stations.

Programs for the on-board equipment carried by both spacecraft were the same during the descent stage, so we shall limit ourselves to reviewing the program for the Luna 13 radar when it measured the characteristics of

reradiation from the surface. The results of radar measurements by both spacecraft will be discussed separately.

The Luna 13 program for the descent stage was as follows. After determination of the direction of the lunar vertical (the direction to the geometric center of the moon) by the optical sensors in the astro-orientation system, the control system stored this direction on the trajectory and oriented the longitudinal axis of the spacecraft with respect to it. This was followed by the craft's stabilization system being energized automatically, thus maintaining the longitudinal axis of the spacecraft in the stored direction with adequately high accuracy. The radar then was energized by the programmer-timer. The on-board radio telemetry system simultaneously began to sample the radar parameters. The Luna 9 radar began operations 350 km above the lunar surface, Luna 13 when it was 550 km above the surface [45].

Telemetry measured the power emitted by the radar transmitter, echo /109
strength at the receiver input, and recorded the deviation of the longitudinal axis of the spacecraft from the direction of the lunar vertical.

Outer-trajectory measurements were used to determine the position of the automatic station relative to the lunar surface during the descent stage. The ballistic calculation made later established the trajectory for the part of the descent stage during which the radar was operating, established the relationship between astronomical time and altitude, and deviation of the radar beam from the direction to the center of the moon. The ballistic calculation was made from data from extra-trajectory measurements, and from sensor readings obtained by the spacecraft's control system.

The dependence on astronomical time was established from telemetry data and outer-trajectory measurements for the following parameters: (1) power transmitted by the radar transmitter; (2) signal strength at the radar receiver input; (3) the angle θ_0 between the direction of the beam maximum and the local vertical; (4) flight altitude.

Simultaneous processing of telemetry information and the results of the ballistic calculation of the descent path for the automatic station provided the flight altitude dependence for the above parameters.

Preflight radar tests included measurements of wavelength, transmitter pulse width, receiver noise factor, antenna pattern, and antenna gain factor.

Experimental radar beam patterns for Luna 9 for vertical and horizontal polarization coincided with the corresponding experimental patterns for Luna 13, and the averaged patterns for both polarizations of these antennas were similar. Figure 4.12 shows these patterns [41]. The telemetry data, when decoded, revealed that the power radiated by the radar transmitters of Luna 9 and Luna 13 remained constant during the measurements.

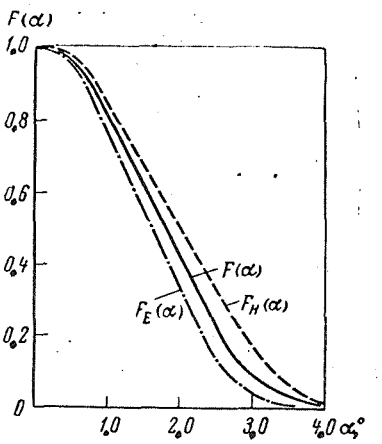

Figure 4.12. Experimental antenna patterns. E plane: $2\alpha_{0.5} = 3^{\circ}20'$; H plane: $2\alpha_{0.5} = 3^{\circ}50'$; Averaged: $2\alpha_{0.5} = 3^{\circ}36'$.

Figures 4.13 and 4.14 show the change in signal power at the radar receiver input with vehicle flight altitude for automatic stations Luna 9 and Luna 13.

The signal strength at the receiver input was used to find the reflectivity of the surface in the landing areas for these automatic stations. The $\sigma_{0\,N}$ was established in the range of altitudes at which the echoes were recorded.

The following law was used to approximate the on-board antenna pattern, measured experimentally (Figure 4.15) [41, 45] /110

$$F(\alpha) = \cos^{n}\alpha, \qquad (4.5)$$

where

$n = 1800$.

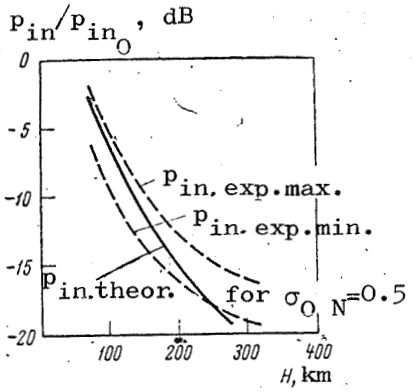

Figure 4.13. Power of reradiated signal at the input to the receiver in the automatic station Luna 9 in terms of flight altitude.

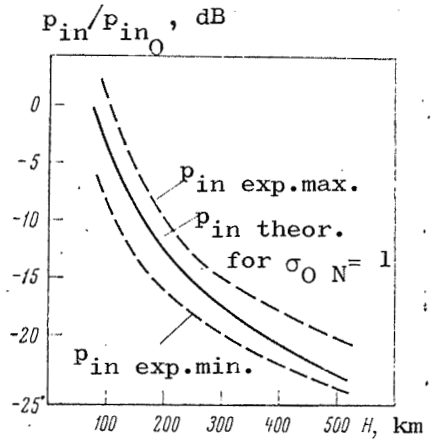

Figure 4.14. Power of reradiated signal at the input to the receiver in the automatic station Luna 13 in terms of flight altitude.

The following law was used to approximate the backscattering pattern for the lunar surface (Figure 4.16) [41, 45]

$$B(\theta) = \cos^m(\theta), \tag{4.6}$$

where

m = 46.

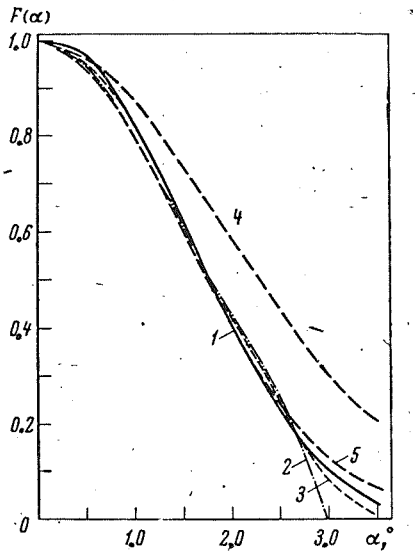

Figure 4.15. Approximation of the averaged beam pattern.

1 - experimental curve;
2 - approximation from the $\cos^{1400}\alpha$ law;
3 - from the $\cos(25 \sin \alpha)$ law;
4 - from the $e^{\frac{-2\alpha^2}{(3.8)^2}}$ law;
5 - from the $e^{\frac{-2\alpha^2}{(3.05)^2}}$ law.

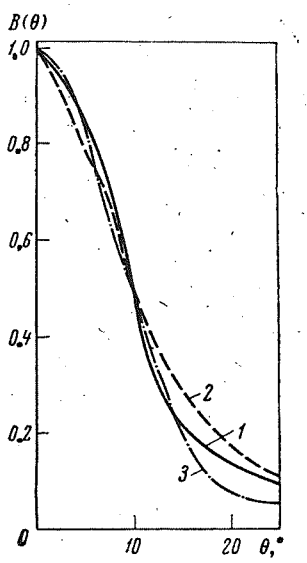

Figure 4.16. Backscattering pattern for the moon at 3 cm.

1 - experimental curve (Evans, Pettengill);
2 - approximation from the $(\cos^4 \theta + 21 \sin \theta)^{-3/2}$ law;
3 - approximation from the $\cos^{46}\theta$ law.

This latter approximation, as reference [41] points out, coincides closely with the experimental backscattering pattern at 3.6 cm (Figure 4.16) [109].

The $\sigma_{0\,N}$ for Luna 9 was established between 70 and 350 km, and at altitudes between 70 and 550 km for Luna 13 [26, 45]. The preliminary results of the $\sigma_{0\,N}$ determinations are contained in [41, 45]. They do not, however, include the pulse mode operation of radio altimeters, or the statistical characteristics of the echo. The r-f pulses reradiated by the lunar surface are very different from those radiated by the radar. They spread and fluctuate within the limits of their own width, as well as from period to period. The magnitude of this effect cannot be fixed by the measurement scheme, so the measurements were processed in [26] on the assumption that the echo amplitudes were random and distributed in accordance with Rayleigh's law. This was confirmed by the results of ground radar measurements in the case of the moon [21]. The distribution in [26] took this law into consideration /112
for the construction of the theoretical curves for signal strength at the receiver input in terms of altitude for constant $\sigma_{0\,N}$ values. These curves are shown in Figure 4.13 for Luna 9, and in Figure 4.14 for Luna 13 for $\sigma_{0\,N}$ values of 0.5 and 1.0, respectively [26].

Reference [26], in its calculation of echo strength, used Gaussian approximations of the surface backscattering pattern and antenna pattern. This resulted in a formula for echo strength different in form from that in this book.

Comparison of theoretical and experimental curves provided the reflectivity for each flight altitude. $\sigma_{0\,N}$ is plotted in terms of H for Luna 9 in Figure 4.17, and for Luna 13 in Figure 4.18. The measurement accuracies cited in [26] show that the errors for each flight altitude were approximately ±3.0 dB.

The mean $\sigma_{0\,N}$ values at the landing sites selected for the automatic stations were similar; $\sigma_{0\,N_m} \simeq 0.5$ for Luna 9 and $\sigma_{0\,N_m} \simeq 1.0$ for Luna 13.

Reference [41] assumed an error in the averaged reflectivity calculation for the visible part of the lunar surface, so the results were recalculated

in this book (see Figure 4.7) and the value was $\sigma_{0\,N} = 0.7$ at $\lambda = 3.2$ cm.

Comparing the measured mean values of reflectivity at the landing sites for these automatic stations with the averaged $\sigma_{0\,N}$ values for the lunar disk shows that $\sigma_{0\,N_m} \simeq 0.7\bar{\sigma}_{0\,N}$, for Luna 9, $\sigma_{0\,N_m} = 1.4\,\bar{\sigma}_{0\,N}$ for Luna 13, and that $\sigma_{0\,N_{mL-13}} = 2\,\sigma_{0\,N_{mL-9}}$.

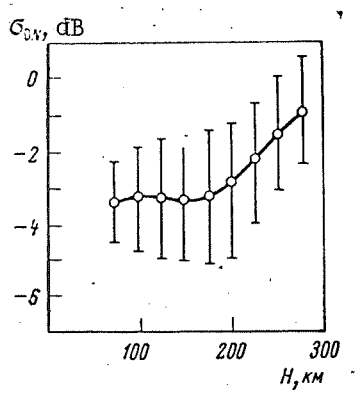

Figure 4.17. Reflectivity of the lunar surface for normal incidence at $\lambda = 3$ cm from Luna 9 measurements.

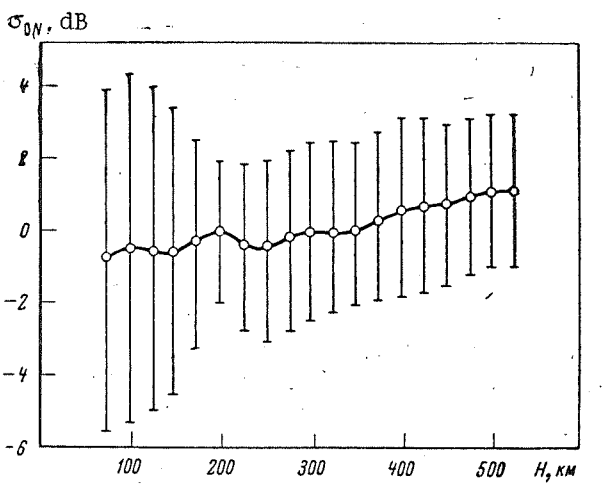

Figure 4.18. Reflectivity of the lunar surface for normal incidence at $\lambda = 3$ cm from Luna 13 measurements.

6. Measurement of the Reflectivity of the Lunar Surface during the Landing of Surveyor 1, Surveyor 3, Surveyor 5, Surveyor 6, and Surveyor 7 /113

The following equipment was installed in Surveyor 1, as well as in the other vehicles in this series [97].

1. An AMR 3-cm marker radio altimeter (RA) operating in the altitude range from 350 to 75 km above the lunar surface. This instrument generated a single signal to activate the main retrorocket 90 km above the lunar surface.

2. An RADVS 2-cm Doppler speed meter (DSM) that operated from 11 km down to the lunar surface.

3. A 2-cm low-altitude radio altimeter that operated from 11 km down to the lunar surface. This altimeter is part of the RADVS complex.

The low-altitude radio altimeter and the Doppler speed meter were connected into the vehicle control system circuit during the descent stage. They generated signals proportional to the flight altitude and the components of the speed vector of the approach to the lunar surface for three axes, the two lateral and the vertical. Table 4.3 lists the principal characteristics /114 of these instruments.

TABLE 4.3

Parameters	High-altitude radio altimeter	Low-altitude radio altimeter	Doppler speed meter
Wavelength, cm	3.22	2.32	2.25
Transmitted power, watts	1800	0.28	2.2
Pulse width, sec	3.2	CW	CW
Repetition rate, Hz	350	same	same
0.5 level antenna beamwidth, degrees	3.2	5.4	6.0
Antenna gain	2300	800	650
Fixed antenna angle (from the normal to the surface), degrees	6	0	25
IF amplifier pass band, kHz	-	10	10

The echo levels at the inputs to their receivers were telemetered when these systems were in operation. The results of the measurements made of the characteristics of reradiation from the lunar surface by the high-altitude (marker) radio altimeter have not been published.

Once the telemetry of echo strength at the inputs to the three channels of the Doppler speed meter and the low-altitude radio altimeter had been processed, the results provided the radar cross sections of the illuminated areas. The low-altitude radio altimeter, calibrated for $\theta_0 \cong 0$, measured $\sigma_{0\,N}$. The Doppler speed meter, calibrated for $\theta_0 \cong 25^\circ$, measured reflectivity, σ_0. Figures 4.19 - 4.20 show the results of the $\sigma_{0\,N}$ and σ_0 measurements.

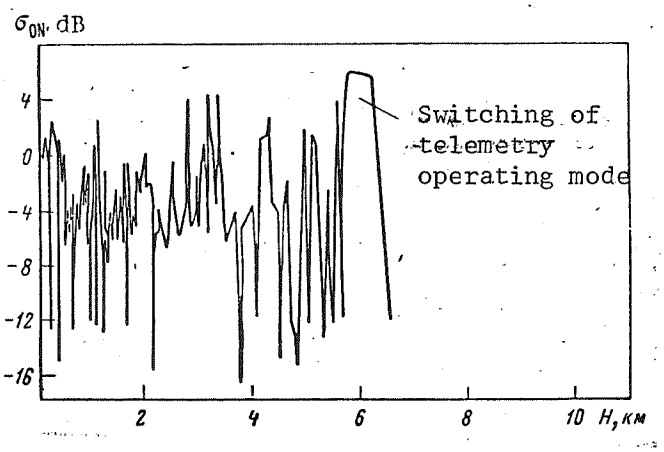

Figure 4.19. Reflectivity for normal incidence at λ = 2.32 cm from Surveyor 1 measurements.

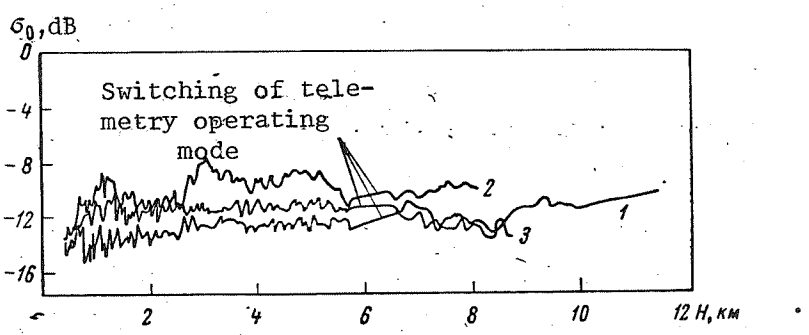

Figure 4.20. Reflectivity at λ = 2.25 cm from Surveyor 1 measurements. 1, 2, 3 - receiver channel numbers.

The Surveyor 1 landing site was photographed from Lunar Orbiter 1. Comparison of the Surveyor 1 landing trajectory from the σ_0 measurements for the landing stage and the photography of the areas provided a tentative connection between anomalies in the σ_0 measurements and the surface relief. It was established that the increased σ_0 value in the first channel at altitudes from 3000 to 6000 meters derived from illumination of part of the crater reaching these altitudes in the scan zone. This increased σ_0 approximately 2.5 dB. This same phenomenon was noted on the second channel at altitudes between /115
1000 and 1500 meters, where the σ_0 increased approximately 2 dB. The surface area within the zone illuminated by the third channel was found to be relatively level, with comparatively identical echo characteristics. Combined processing of σ_0 values from the three channels of the Doppler speed meter showed that in the case of a comparatively level surface (no craters with D > 100 m) and $\theta_0 = 25^\circ$ at $\lambda = 2.25$ cm the reflectivity was $\sigma_0 = -12\pm2$ dB (0.04-0.1).

Processing the σ_0 measurements by the low-altitude radio altimeter reveals that the reflectivity (normal incidence) at $\lambda = 2.32$ cm was $\sigma_{0\,N} =$ -6 ± 4 dB (0.1-0.64). Individual surges in measurements achieved values of /116
$\sigma_{0\,N_{max}} = -14$ to 4 dB.

If it is accepted that the backscattering pattern, $B_0(\theta)$, for the section of the surface illuminated by the antennas of the Doppler speed meter coincides with the averaged backscattering pattern for the visible part of the lunar surface, $B(\theta)$, the formula

$$\sigma_0 = \sigma_{0N} B(\theta). \tag{4.7}$$

can be used to find $\sigma_{0\,N}$ from the measurements made of σ_0. Assuming that the approximating function for the backscattering pattern for the visible part of the moon is a law subordinate to Beckmann's formula, Eq. (2.58), we will have C = 10.5, and K = 3.7 for $\lambda = 2.25$ cm. The backscattering pattern for the moon for $\lambda = 2.25$ cm is shown in Figure 4.21. It already has been pointed out that the deviation of the real pattern, $B(\theta)$, from the diagram obtained by the Beckmann formula is a maximum of ±1 dB. So $B(25^\circ) = -6\pm1$ dB for $\theta_0 = 25^\circ$. In this case, $\sigma_{0\,N}$ at $\lambda = 2.25$ cm will be $\sigma_{0\,N} = -6\pm3$ dB (0.12 to 0.5) [43]. Thus, the mean $\sigma_{0\,N}$ value from the $\lambda = 2.25$ and 2.32 cm

measurements equals 0.25. This is the averaged magnitude for an area, the dimensions of which were equal to the area of the illuminated section of the surface that changed from 1.5 km^2 to units of square meters during the experiment. The area illuminated by the low-altitude radio altimeter too changed from 0.7 km^2 to units of square meters. The error in determining the value of the reflectivity by the low-altitude radio altimeter and the Doppler speed meter could reach ±4 dB in this experiment [97]. The calculation of the averaged $\sigma_{0\,N}$ for the visible part of the moon for λ = 2.3 cm from data from ground radar measurements yields $\sigma_{0\,N} \simeq 0.4$, with an accuracy of ±3 to 4 dB. So, we see that the measurements of $\sigma_{0\,N}$ in the 2 cm band for the Surveyor 1 landing area (a relatively level mare region) differ slightly /117 from those for the lunar disk.

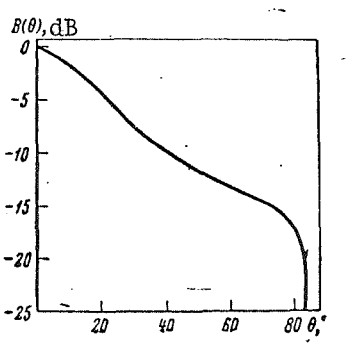

Figure 4.21. Calculated backscattering pattern for the moon at λ = 2.25 cm.

Measurement of characteristics of reradiation from the lunar surface by the other vehicles in the Surveyor series was made similarly. Whereas the flight of Surveyor 1 over its descent site was made precisely along the direction of the local vertical, the other vehicles in the Surveyor series landed at rather large depression angles. Therefore, while σ_0 was found for but two depression angles, 0° for the low-altitude radio altimeter, and 25° for the three channels in the Doppler speed meter, it was found for all angles between 0 and 60° for Surveyors 3, 5, 6, and 7. This made it possible to calculate $\sigma_{0\,N}$, and to determine the backscattering pattern for the local

regions of the lunar surface in the landing areas for these vehicles. Figures 4.22 - 4.24 show the data for the Surveyor 5, 6, and 7 landing sites.

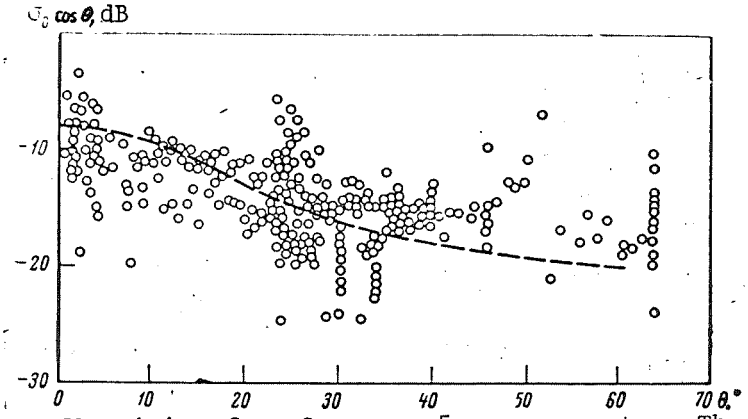

Figure 4.22. Reflectivity from Surveyor 5 measurements. The dashed curve is for $\bar{\sigma}_{ON}(\cos^4\theta + 10\sin^2\theta)^{-3/2}\cos\theta$.

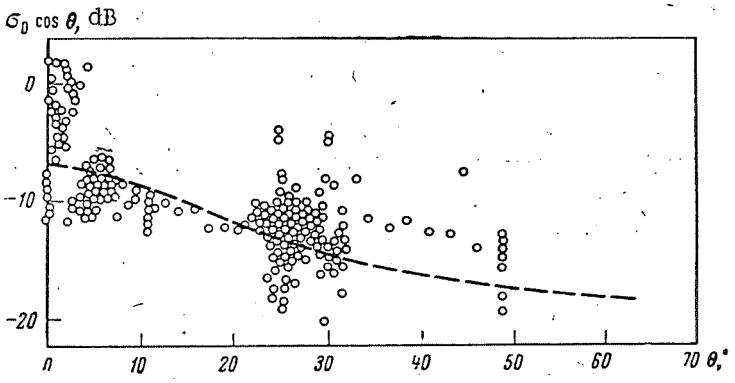

Figure 2.23. Reflectivity from Surveyor 6 measurements. The dashed curve is for $\bar{\sigma}_{ON}(\cos^4\theta + 10\sin^2\theta)^{-3/2}\cos\theta$.

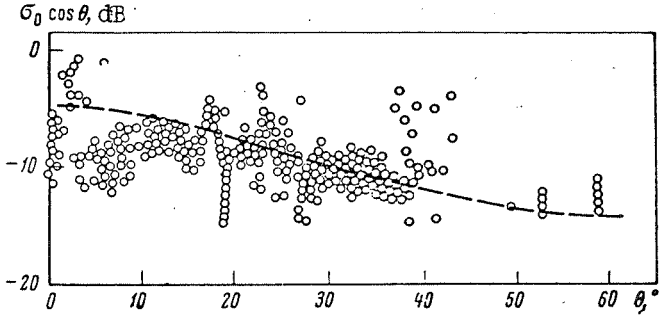

Figure 2.24. Reflectivity from Surveyor 7 measurements. The dashed curve is for $\bar{\sigma}_{ON}(\cos^4\theta + 5\sin^2\theta)^{-3/2}\cos\theta$.

Analysis of the $\sigma_{0\,N}$ measurements by the vehicles in the Surveyor series in the 2 cm band shows little difference in their values for the maria regions investigated. The strongest echo (Surveyor 1 landing site) differs from the weakest (Surveyor 5 landing site) by a factor of 1.5 (2 dB) The $\sigma_{0\,N}$ value at the Surveyor 7 landing site (the continental region near the crater Tycho is greater than the $\sigma_{0\,N}$ value found for the Surveyor landing sites in the maria regions by a factor of 2. This difference apparently is connected with the greater mean density of the lunar surface layer material in the continental regions relative to the maria regions, and with the relatively small difference in the density of the material of the moon's upper crust at different places in the maria regions.

The backscattering patterns obtained are such that it is difficult to approximate the reliability of some sort of definite law with any degree of certainty, because of the considerable scatter in the measurements of the σ_0 values at different depression angles. However, such an attempt was made in the course of the a priori approximation by Beckmann's law [see Eq. (2.58)]. The result was to find the least root-mean-square error for the approximation of the backscattering patterns for maria regions (Surveyor 3, 5, 6) using Beckmann's law with a coefficient C = 8 to 10, and for the crater Tycho region, again using Beckmann's law and a coefficient C = 5. These approximations correspond to approximately identical roughnesses of the surfaces of the maria sections studied, and to the rougher surface in the crater Tycho region. It should be pointed out that the backscattering pattern for the moon has C = 10.5, based on the Beckmann law approximation for λ = 2.25 cm. In other words, the nature of the backscattering of radio waves in the moon's maria regions is very nearly that of the moon's backscattering when observed from the earth.

The radar measurements from the vehicles in the Surveyor series permit the drawing of certain conclusions with respect to the influence surface relief has on the echo strength. The mean value of the echo increases, and there is a considerable increase in echo fluctuation, when craters and surface sections with extensive relief changes are within the zone illuminated by the radar (Figure 4.25). Fluctuations rising from 1-2 to 5-7 dB were

noted as the beam traversed hilly areas, young craters, and particularly craters with central peaks. The σ_0 value rose 3-5 dB in the latter case. These results agree well with the results of ground radar charting of the moon, and with the Lunar Orbiter 1 experimental data.

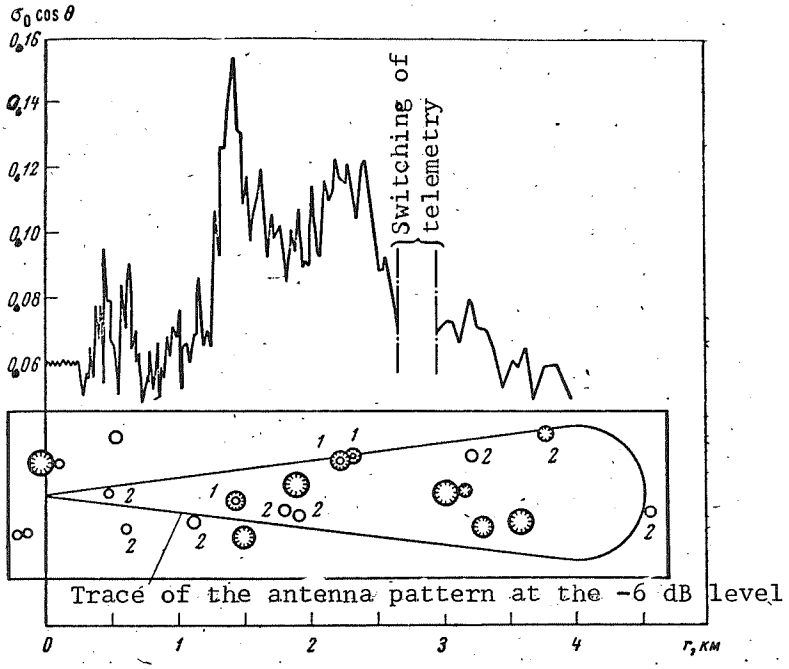

Figure 4.25. Correlation between the radar signal and the illuminated surface (first channel Surveyor 1).

1 - crater with central peak;
2 - young crater.

Table 4.4 lists the results of measuring reflectivity for local regions /120 of the moon from spacecraft.

7. Measurement of Integrated Reradiation Coefficient by Luna 11 and Luna 12

Measurements were made by simultaneous readings at ground stations of the power of the direct signals and of the signals reradiated from the lunar surface. The vehicle's on-board transmitter operated on CW at a wavelength of $\lambda \simeq 1.7$ meters, radiating electromagnetic energy from an omnidirectional antenna. Direct and reradiated signals were selected by frequency filtering this signal, which had different Doppler frequencies. The orbital parameters of Luna 11 and Luna 12 are contained in the appendix.

TABLE 4.4

Spacecraft	Wavelength cm	Radiation	Antenna beamwidth, °	Reflectivity for normal incidence				Measurement region
				Mean measured value		Averaged value for disk		
				Magnitude	Accuracy, dB	Magnitude	Accuracy, dB	
Luna 9				0.5				Mare
Luna 13	3	Pulse	3.5	1.0	±3	0.7	±(3-4)	Mare
Surveyor 1				0.25				Mare
Surveyor 3				0.2				Mare
Surveyor 5	2.25	CW	6	0.16	±4	0.4	±(3-4)	Mare
	2.32	Same	5.4					
Surveyor 6				0.2				Mare
Surveyor 7				0.4				Continent
Lunar Orbiter 1	13.1	Unmodulated	Omnidirectional	$\frac{\sigma_0}{\overline{\sigma}_{0\ \text{background}}} < 7$				Continent

The Luna 11 and Luna 12 antenna patterns were quite different from isotropic, so for purposes of eliminating the effect of the radiation pattern when processing the measurements to find the ratio of reradiated to direct signal powers, η^2, there was introduced an average for this ratio, obtained from a great many identical measurements. Luna 11 and Luna 12 took over 150 measurements at different grazing angles and altitudes. These were combined into 20 groups, with each group containing measurements in which grazing angles were very nearly the same [81, 82]. Each group was averaged, followed by the construction of two dependencies of η on the grazing angle. These are shown in Figure 4.26. Curve 1 is for the average satellite altitude, equal to 250 km, and curve 2 is for a mean altitude of 1000 km [82].

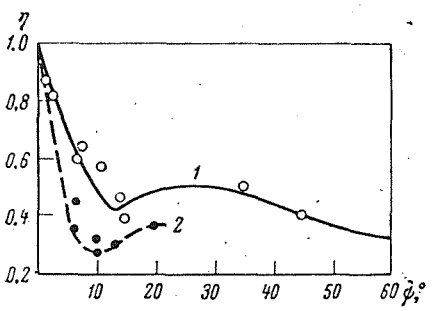

Figure 4.26. Scatter factor η in terms of grazing angle at $\lambda = 1.7$ m from Luna 11 and Luna 12 measurements ($\psi = 90^\circ - \theta$).
1 - H_m = 250 km; 2 - H_m = 1000 km.

The reradiation coefficient for a spherical surface depends on a number of factors, including the divergence factor (for the quasi-specular component of the echo), determined by the distance from the satellite to the scatterer on the lunar surface and the angle of incidence [see Eq. 2.23)].

Figure 4.26 shows that increasing the flight altitude results in a reduction in η, something apparently associated with change in the divergence factor, as well as with change in the dimensions of the scatterer contained within the maximum for the lobe of the on-board antenna pattern. The authors of reference [82] found instability in η at large angles of incidence (greater than 80°), and associated it with the great difference in reradiation from different sections of the lunar surface, creating diffuse scattering, or

specular reflection, of radio waves, depending on the individual properties /122
of the sections.

Nevertheless, η remains relatively constant for a specified grazing angle when such angles are larger than 10°. Reducing θ results in a drop in η, tending to a magnitude that can be found by radar measurements from the ground when $\theta = 0$.

Reference [81] estimated the width of the echo spectrum at less than 20 Hz, and this corresponds to the specular nature of the reradiation from the lunar surface at $\lambda = 1.7$ m. This agrees well with the results of ground radar measurements at the same wavelength. Recording of the diffuse component of the echo was very irregular in these experiments.

The η to θ ratio obtained made it possible to estimate the permittivity and depression angle for the lunar surface scatterers by comparing this experimental ratio with a number of theoretical ones.

The calculation revealed that at a wavelength of 1.7 meters the permittivity, ϵ, is 2.85 ± 0.15, and that the root-mean-square depression angle for large-scale irregularities, σ_{α}, is 12°.

8. Measurement of Characteristics of Reradiation by Lunar Orbiter 1 and Explorer 35

The method used to measure the nature of the reradiation from the lunar surface by Lunar Orbiter 1 on 12 October 1966 [170], was very like that used earlier by Luna 11 and Luna 12 [81, 82].

Lunar Orbiter 1, while in lunar orbit, radiated an unmodulated signal /123
at a wavelength of 13.1 cm from an omnidirectional antenna. The separation of the direct signal and the signal reradiated from the lunar surface was accomplished at a ground station by Doppler frequency selection. But, as distinguished from the procedure used in the experiments conducted with Luna 11 and Luna 12, Lunar Orbiter 1 measured the reradiated signal power, made a continuous recording of its spectrum with a high degree of resolution, and measured its frequency shift relative to the direct signal. Lunar Orbiter 1 did its work in the equatorial zone, near the eastern edge of the moon, in the vicinity of the crater Kastner. Its orbit was very nearly

equatorial, with the altitude at the pericenter approximately 40 km. These measurements were made during the satellite's "radioset" beyond the eastern edge of the moon. A simplified recording of the reradiated signal spectrum, obtained while the space vehicle was moving, is shown in Figure 4.27.

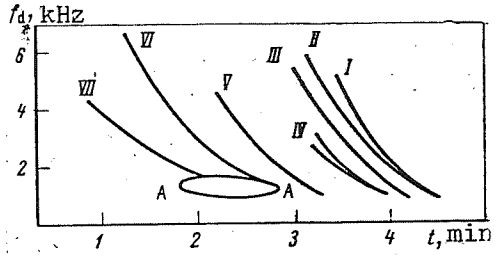

Figure 4.27. Simplified recording of echo spectrum at λ = 13.1 cm from measurements by Lunar Orbiter 1.

The Doppler shift in the echo relative to the direct signal is plotted along the vertical. Signal strength is found from the brightness of the recording for the corresponding section of the spectrum. Several discontinuous lines, the Doppler frequencies of which changed with time, were obtained on this recording near the "radioset" region. This change in the Doppler frequency can be explained by the scattering of the radio waves by a fixed "bright" scatterer on the lunar surface. This scatterer was near the limb during the experiment, and when the satellite approached this scatterer the difference in the Doppler frequencies of direct signals and echoes from this scatterer decreased.

Determination of the center, and of the dimensions of the scatterers corresponding to the lines designated by the numbers in Figure 4.27, was made as follows. The position of the satellite in orbit, the magnitude and direction of the speed vector, and the coordinates of the subsatellite point, and of the point corresponding to the specular reflection, were determined for each moment in time from exterior trajectory measurements. /124 The line on the lunar surface corresponding to the Doppler shift in echo frequency for the unknown scatterer then was determined. This line, as has been pointed out, is the line of intersection of a cone with a spherical planetary surface. There can be two such lines on the planet's surface in the general case. This duality can be eliminated by using the hypothesis that the centers of reradiation are located in the vicinities of the specular reflection points.

The line of intersection of cone and surface can be determined for each moment in time because of the correspondence between the Doppler frequency from the scatterer and the angle between the direction from the space vehicle to the scatterer and the direction of the space vehicle's speed vector. This is expressed by

$$f_{d_{sc}} = \frac{V}{\lambda} \cos \xi, \qquad (4.8)$$

where

$f_{d_{sc}}$ is the Doppler frequency for the corresponding scatterer;

V is the modulus of the space vehicle's speed vector.

A sequential determination of lines on the lunar surface for different times satisfying Eq. (4.8), the time of existence of which can be determined from the recording of the echo spectrum, results in finding the boundary of the "radio bright" area, points within which participate in producing this signal. The processing of the echo spectrum provided the data for compiling a radar chart of the section of the lunar surface in the crater Kastner area. This chart, superposed on corresponding sections of the complete chart of the moon [57], is shown in Figure 4.28. The error in fixing the centers of the "radio bright" scatterers on this chart is a maximum of 10 km. The centers of the rectangles indicate the coordinates of the centers of reradiation, and the dimensions of scatterers I, II, and III are fixed by measurement errors, according to the authors of the experiment [170]. Scatterers IV, V, VI, VII and A have dimensions fixed by measurement errors, as well as by the inherent dimensions of radar targets, ranging to 10-30 km.

Analysis of the locations of the scatterers on the lunar surface revealed that several radio bright areas (as many as four) located near the line of specular reflection point travel reflect simultaneously, at the same time that this point coincides successively with Scatterers IV, VI, VII. These scatterers continue to radiate strongly even when the "specular reflection" condition is no longer satisfied for them. Analysis of change in signal corresponding to curve III in Figure 4.27 revealed that this curve on the lunar surface corresponds to two regions, IIIa and IIIb, as well as to a region intermediate between them. Thus, of 36 points considered, 10 are in region IIIa, 15 in IIIb, and 11 in the intermediate region. /126

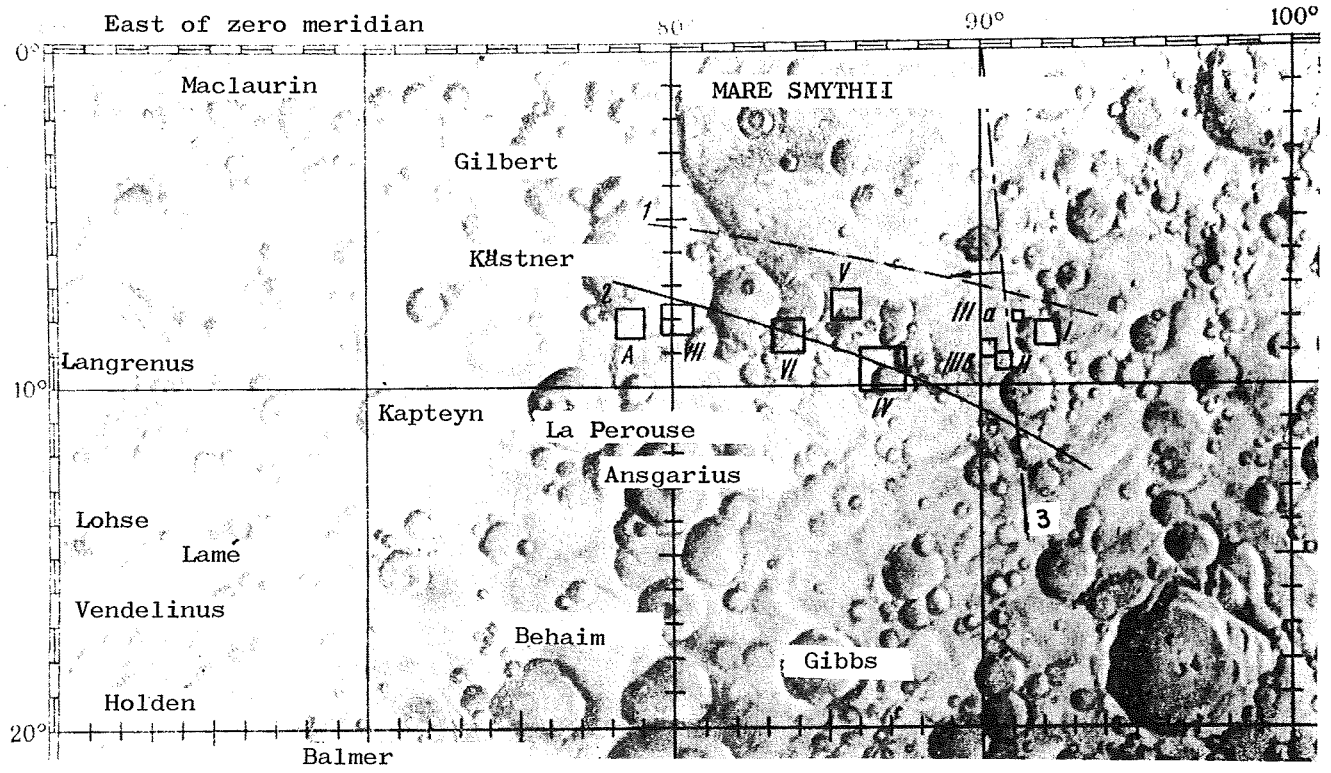

Figure 4.28. Radar chart of the crater Kästner region.

1 - plot of subsatellite point;
2.- plot of specular reflection points;
3 - boundary of visible part of the moon from the earth during the experiment.

The appearance of an intermediate reradiation region is the result of regions IIIa and IIIb simultaneously taking part in producing the echo. The echoes from these regions undergo temporal strength changes leading to a shift in the effective center of their reradiation, as it were.

Analysis of the brightness of individual sections of the echo spectral line reveals the excess of the echo level from the "bright" sections relative to the level of an echo from the surface surrounding these sections. This excess was 3 - 4 dB for all sections other than III, where it was 5.5 dB. Ground radar observations of backscattering from lunar craters developed a similar excess [155, 167]. True enough, observation conditions were different during ground radar investigation of the moon than during the Lunar Orbiter 1 experiment. In the latter case, the incidence and aspect directions did not coincide, whereas they did in the former. All other conditions being the same, in the latter case the echo level is determined by the scattering indicatrix, and by the backscattering pattern in the former.

Analysis of temporal change in echo strength from each "radio bright" scatterer, made by the authors of the experiment, revealed that the observed nature of the change cannot correspond to isotropic scattering from these scatterers in the case of an increased reradiation coefficient for them relative to the surrounding surface. The authors are of the opinion that the most suitable model of such surface can be one in which the mechanism of reradiation from "radio bright" scatterers can be established by the simultaneous presence of three factors: an increased reflection coefficient; roughness of these scatterers; and a slope relative to the perpendicular to the local vertical.

The scattering indicatrix is about 6^{o} wide at the -3 dB level, according to the preliminary evaluation of the measurements (incidence and aspect angles between 78 - 90^{o}). Similar measurements, made by the authors of reference [170] in the central part of the lunar disk, where the shadowing effect is absent, revealed that there are individual "radio bright" scatterers on its surface as well. These measurements confirmed the hypothesis concerning the heterogeneity of the properties of reradiation by the lunar surface, something that can be explained by the difference in the reradiation

coefficient for different sections of the surface, and by the difference in their geometric characteristics (roughness and slope).

Matching the radio bright sections in the crater Kästner region with photography of this section of the surface (Figure 4.28) led to the following conclusions.

1. The majority of the sections (A, IIIb, IV, VII) are on the internal slopes of craters. /127

2. Some sections are inside craters (I, II).

3. Section IV includes parts of the surfaces of two craters (45 percent of the area of each crater).

4. Sections V and VI are on very uneven sections of elevated (VI) and depressed (V) sections of Mare Smythii.

5. The majority of the radio bright sections do not coincide with the specular reflection point.

6. Sections located at the bottom of craters can reradiate because of the focusing effect of the crater depression, and because of the increased density of its soil.

As we see, the majority of the radio bright sections are located at sites, the relief of which lends itself to increased reradiation of electromagnetic energy for constant electrical properties of their surface layer relative to more level sections of the surface (rough sections and internal slopes of craters).

Explorer 35 measured the characteristics of scattering by the lunar surface in the equatorial zone at $\lambda = 2.2$ m [170a]. The procedure used was similar to that used for Lunar Orbiter 1. Polarization characteristics of the on-board transmitting antenna were different for different directions relative to the antenna's geometric axis, so sections involving but four revolutions of the satellite for which the polarization of the signal illuminating the surface of the moon was clearly known could be selected for processing the results of the experiment. The plots of the specular reflection point for these sections were in the 0° - 10° S, 10° - 80° W regions. Three

of the four experiments were conducted for circular polarization of the flux illuminating the surface, and one for linear polarization.

Preliminary analysis revealed that the most instantaneous echo spectra observed during these experiments corresponded to the quasi-specular reflection with a small diffuse component. This is why a smooth surface model was used to interpret the measurements.

The linear polarization experiment measured the ratio of echo and direct signal strengths at a ground reception station in the range of angles of incidence $\theta = 15^{\circ} - 80^{\circ}$, but the circular polarization experiments measured this ratio for $\theta = 10^{\circ} - 45^{\circ}$ simultaneously at two orthogonal, linear polarization receiving antennas. These data were corrected for the divergence factor. The reflection factor then was plotted in terms of the angle of incidence. The Brewster angle was found for the linear polarization experiment, and the mean value of the permittivity of the surface layer in the region investigated was calculated /128

$$\varepsilon = (\arctan \theta_B)^2. \qquad (4.9)$$

The result was $\theta_B = 60 \pm 1^{\circ}$ and $\varepsilon = 3.0 \pm 0.2$.

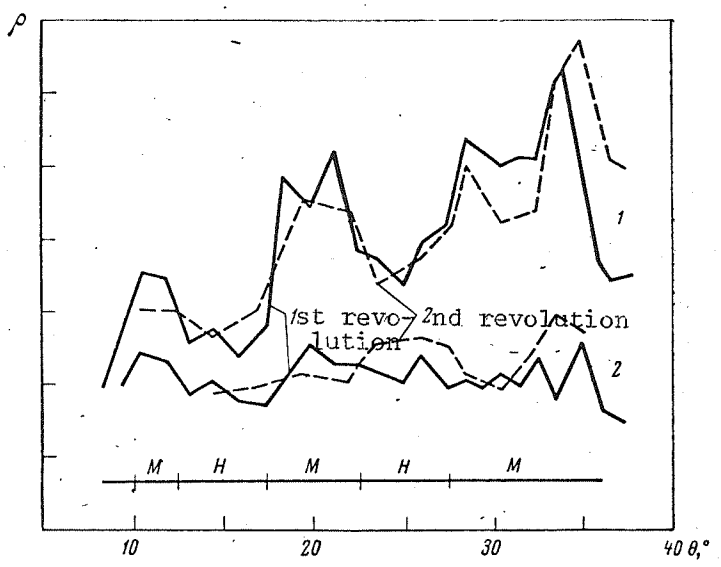

Figure 4.29. Reflection factor, ρ, in terms of angle of incidence at $\lambda = 2.2$ meters from Explorer 35 measurements. M - maria regions. H - continental regions.

Noted in the course of the circular polarization experiments was the fact that echoes from maria regions were approximately 30 percent stronger than those from the continental regions. This was explained by the fact that there was an approximate 15 percent increase in the permittivity of the surface layer of maria regions as compared to continental regions; $\epsilon_H = 2.8$ and $\epsilon_M = 3.2$. Figure 4.29 shows the reflection factor in terms of the angle of incidence for two series of measurements for orthogonal linear polarization (1, 2) of ground receiving antennas. These results differ from the generally accepted hypotheses whereby the mean density and permittivity of the material of the upper crust of the moon should be higher for the continental regions.

An increase in echo strength was noted in the crater Flemsteed region, which, within the context of a smooth surface model, corresponds to an increase in ϵ for this region to $\epsilon = 5.5 - 6.1$. These results correlate well with ground radar and infrared observations of this region [160a, 167] and, apparently, correspond to the protrusion of rocks onto the lunar surface in this region. /129

9. Measurement of Characteristics of Reradiation by Luna 14

The experiment conducted with Luna 14 to investigate the reradiation of radio waves was an extension of the Luna 11 and Luna 12 experiments. This experiment radiated unmodulated oscillations at $\lambda = 1.7$ meters, and recorded the strengths of the signals, both direct and those reradiated by the lunar surface, while recording the instantaneous echo spectrum.

The data obtained from the system of exterior trajectory measurements were used to determine the position of the satellite relative to the lunar surface, the positions of specular reflection points, and the values of the Doppler frequencies of the echo corresponding to them, for each of the instantaneous spectra. Comparison of calculated values of Doppler frequencies for specular points with measured values of frequencies corresponding to the maximum echo spectral density, revealed that the region of the surface producing the greater part of the echo is close to the specular reflection point, and that the center of this region coincides with the specular reflection point.

A preliminary analysis revealed that the instantaneous echo spectrum is determined by surface relief in the region near the specular reflection point. The instantaneous spectrum expands substantially in regions with uneven relief as compared to what happens where the surface section is relatively flat. The echo spectrum has a brightly reflected specular characteristic when flight is over level sections of the surface near the specular reflection point.

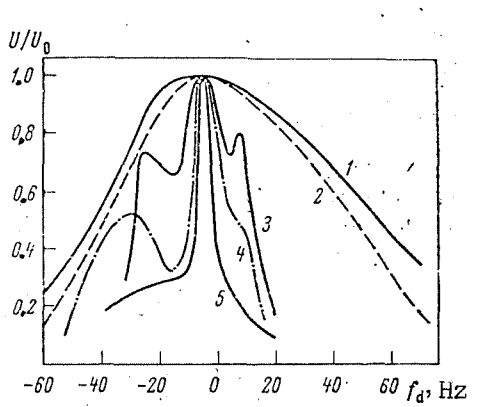

Figure 4.30. Some experimental spectra of an echo from the moon at λ = 1.7 m.

Figure 4.30 is an example of several instantaneous spectra of an echo (in terms of voltage) [84]. Doppler frequency, $f_D = f - f_0$, where f_0 is the carrier frequency of radiation from the on-board transmitter, and f is the current value of the echo frequency, is plotted along the horizontal axis.

Spectra 1 and 2 correspond to reradiation from an uneven region of the lunar surface. The contribution of the narrow-band component attributable to reradiation from the region in direct proximity to the specular reflection point is significant in spectra 3 and 4.

Spectrum 5 corresponds to reradiation from a relatively flat section of the surface. The following angles of incidence, θ, and satellite flight altitude, H, correspond to these spectra: /130

Spectrum	1	2	3	4	5
θ, °	69	76	66	82	36
H, km	500	500	580	800	816

The echo spectrum width, on the average, decreases with increase in flight altitude because of the spherical divergence effect, and depends on the magnitude of the satellite's speed vector component in the direction of the specular reflection point.

Analysis revealed that a comparison between the instantaneous spectrum of the echo and the surface relief made it possible to estimate the size of the area making the principal contribution to echo production, and to determine the value of their root-mean-square angle of incidence within the scope of a model of a spherical surface covered with flat reflectors of random size, but significantly longer λ, located at random angles to the normal at the specular reflection point.

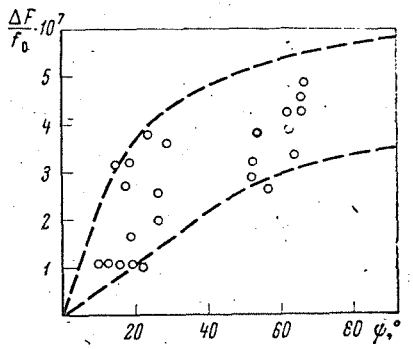

Figure 4.31. Relative width of echo spectrum. The circles are the experimental points.

Figure 4.31 is a plot of the relative high-power spectrum width in terms of the depression angle for satellite altitudes from 200 to 500 km. The dashed curves are the limit values of observed changes in spectrum width. The value of the root-mean-square angle of incidence for large-scale non-level areas is 3^o to 14^o, according to analysis.

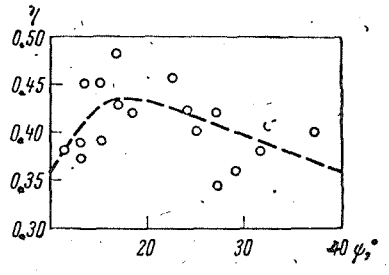

Figure 4.32. Scatter factor (in terms of voltage).

Measurement of the ratio of the powers of the direct and reradiated signals during the experiment provided the power scatter factor, η^2. Figure 4.32 is a plot of the voltage scatter factor, η, in terms of the depression angle for a satellite altitude of 200-400 km. Each experimental point is the average of 15-20 independent measurements for very nearly the same depression angles. Reference [82] compared the experimental relationship with the theoretical, $\eta(\psi)$, and found that a permittivity of $\epsilon = 2.8 - 3.0$, and a root-mean-square angle of incidence $\sigma_\alpha = 5^\circ - 8^\circ$ correspond to this curve. The ratio of echo and direct signal strengths changed during the experiment, even for identical depression angles and very nearly the same satellite altitudes. If this change is associated with change in the permittivity of the surface layer, change in ϵ for individual sections of the visible portion of the moon between 2 - 6 will correspond to it.

Thus, the use of radar from on-board an artificial satellite with a CW transmitter, and reception of direct and reradiated signals at a ground station with continuous recording of the instantaneous echo spectrum, opens up additional possibilities for radar charting the surface of a planet, for estimating the value of the permittivity and slopes of the surface near the specular reflection point, and for determining the size of the scatterer producing a substantial part of the echo. /132

A more detailed analysis of the shape of the instantaneous echo spectrum, and of its change during the experiment, obviously will make it possible to determine the slope, as well as the nature and the prevailing form, of the surface relief.

CHAPTER V

/133

INTERPRETATION OF THE RESULTS OF RADAR INVESTIGATION OF THE MOCN TO DETERMINE THE PHYSICAL CHARACTERISTICS OF ITS SURFACE LAYER

Radar investigation of the lunar surface has made possible an evaluation of certain of the physical properties of the surface layer, and this is in addition to the determination of the echo characteristics over a broad band of radio waves. So radar methods of conducting research provided the capability for establishing the permittivity of the moon's surface layer at different wavelengths, and this, in turn, made possible an assessment of the change in the density of the material with depth. In other words, materials needed to construct a model of the moon's surface layer were obtained. Measurement of the relationship between the angle of incidence and the strength of the electromagnetic energy flux reradiated by the surface provided the backscattering pattern, and the capability for evaluating the roughness of the lunar surface.

1. Coefficient of Reflection for the Moon in the RF Band

The normal incidence power reflection coefficient, $\rho_{s\,N}$, as distinguished from all of the echo characteristics used in radio link energy potential calculations (σ, σ_0, $\sigma_{0\,N}$, $B(\theta)$), does not depend on surface relief, but rather is determined solely by the electromagnetic properties of the material found on the surface of the planet [see Eq. (2.14)]. When the material is a perfect dielectric, the $\rho_{s\,N}$ value establishes its permittivity

$$\rho_{sN} = \left(\frac{\sqrt{\varepsilon}-1}{\sqrt{\varepsilon}+1}\right)^2. \qquad (5.1)$$

The value of the reflection coefficient depends on the wavelength if there is a change in the electromagnetic characteristics of the surface layer (ε, σ_s, μ), with change in the wavelength.

The power reflection coefficient in the RF band can be found from radar observations as well as by processing data from certain radioastronomy observations (polarization measurements, measurements of the distribution of /134

radio-brightness temperature over the disk of the planet). Section 4 of this chapter will compare the results.

There are several ways to define the reflection coefficient from radar observations. These methods represent the lunar surface as two structures, superposed upon each other, and distributed over the lunar surface in random fashion. The irregularities in the surface of the first structure have dimensions shorter than the wavelength, and the echo from them is diffuse in nature, subordinate to Lambert's law. The second structure is a sphere covered with flat facets, each of which is positioned at random angles relative to the local vertical at a particular point on the spherical surface and has dimensions longer than the wavelength, or is represented simply as a perfectly smooth sphere (according to the procedure used by Evans and Pettengill). The echo from the second structure is specular, and in the case of the sphere covered with flat facets the echo strength increases as compared to the strength of the signal reflected from the perfectly smooth sphere of the same size. Consequently, different calculated reflection coefficients will be obtained for each of the models of the second structure participating in producing the specular component of the reradiated signal.

Circular polarization is used for transmission, and reception, in planetary radars in order to do away with the Faraday effect in the propagation of radio waves in the ionosphere of the earth and planets. Theoretical research, and the results obtained from experiments with circular polarization, have shown that what happens in the case of specular reflection is reversal in the direction of rotation of the plane of polarization, at the same time that a diffuse-scattering surface produces an echo with the same, and opposite, directions of rotations of the plane of polarization. The echo with the opposite direction of rotation of the plane of polarization relative to the radiated signal is called the polarized component, that with the same direction the depolarized component.

And, because the power of the echo in the polarized component is stronger than the echo in the depolarized component, the overwhelming majority of radar investigations of the moon, and of the planets, from the ground were made for the polarized component only. Moreover, radar cross section and backscattering pattern magnitudes were measured only for this component. Nevertheless,

recent theoretical and experimental work takes note of additional possibilities of extracting information on surface properties by measuring the echo in both components at once. The particular aspect of these measurements is /135
the simplification of the separation of the echo into diffuse and quasispecular components.

There are different methods for calculating the reflection coefficient, once it is established that the two components can be received simultaneously. However, because the two components were received simultaneously from the moon on just two wavelengths (23 cm and 68 cm), the procedure for finding the reflection coefficient corresponding to this reception method still has but limited application [109, 110].

Existing methods for finding the reflection coefficient from ground radar observations will be reviewed and compared in what follows.

The Rea, Hethering, and Mifflin Method

This method [157] for finding the reflection coefficient uses the results of polarized observations, with measurements of radar cross section and backscattering pattern made for the polarized, as well as the depolarized, component $[\sigma_p, \sigma_d, B_p(\theta), B_d(\theta)]$.

The reflection coefficient is found for the condition that the quasispecular component of the echo is produced by a wavy spherical surface, the dimensions of the irregularities of which are significantly longer than the wavelength.

The radar cross section can be found in terms of the echo strength only for the polarized component, that is, in the same way as for the conventional determination of the radar cross section made for one polarization of the received signal

$$\sigma_\Sigma = \sigma_p = \sigma_s + \sigma_d. \tag{5.2}$$

The backscattering pattern for the quasispecular component can be found from

$$\sigma_s B_s(\theta) = \sigma_p B_p(\theta) - \xi\sigma_d B_d(\theta). \tag{5.3}$$

The magnitude of ξ can be found for the condition that all of the power of the reradiated signal in the polarized component at the limb of the disk is that of the diffuse component. The practical approach for the moon in the RF band is made when $\theta > 50^\circ$. Thus

$$\xi = \frac{\sigma_p B_p(\theta)}{\sigma_d B_d(\theta)} \quad \text{when} \quad \theta > 50^\circ. \tag{5.4}$$

The quasispecular component of the radar cross section σ_s can be found from Eq. (5.3) when $\theta = 0$ /136

$$\sigma_s = \sigma_p - \xi\sigma_d. \tag{5.5}$$

Then, too, the quasispecular component of the echo can be found from

$$\sigma_s = 2\pi a^2 \rho_{s.N} \int_0^{\pi/2} B_s(\theta) \sin\theta \, d\theta. \tag{5.6}$$

Eq. (5.6) is valid only when coherence between radiations from individual surface elements is lacking [see the note to Eq. (2.60)].

Thus, the quasispecular component of the radar cross section, and the reflection coefficient, for the normal incidence case can be found from the σ_p, σ_d, $B_p(\theta)$, and $B_d(\theta)$ measurements with Eqs. (5.3) - (5.6) taken into consideration. These equations also provide the means for calculating the directivity, g_s, for large-scale irregularities.

Reference [109] cites the quasispecular component of the radar cross section as being equal to

$$\sigma_s = \pi a^2 g_s \rho_{s.N}. \tag{5.7}$$

Comparing Eqs. (5.6) and (5.7), we see that

$$g_s = 2 \int_0^{\pi/2} B_s(\theta) \sin\theta \, d\theta. \tag{5.8}$$

The following results were obtained after Rea et al., [158], used the above procedure to process the results of the polarized measurements obtained during the $\lambda = 68$ cm experiment [107]: when $\sigma_\Sigma = 0.074\ \pi a^2$, $g_s = 1.11$, $\sigma_s/\sigma_\Sigma = 0.85$, and $\rho_{s\,N} = 0.057$.

The Evans and Pettengill Method

This method considers only the echo for the polarized component [107]. Two superposed components were used as the surface model: the perfectly smooth one, and the rough one, reradiating in accordance with Lamber's law, and having irregularity dimensions $\leq \lambda$. This method used the convention that the planet's radar cross section comprises the quasispecular and diffuse components, as is the case in the other methods, but found from

/137

$$\sigma_\Sigma = \sigma_S + \sigma_d, \tag{5.9}$$

$$\sigma_S = (1-x)\rho_{S_N}\pi a^2, \tag{5.10}$$

$$\sigma_d = x g_m \bar{A} \pi a^2, \tag{5.11}$$

where

$g_m = 2.67$ is the directivity for a surface reradiating according to Lambert's law;

x is the relative area of the planet's disk attributable to the diffuse component of the reradiated signal;

$\bar{A}$ is the albedo, averaged for all angles of incidence and polarization.

This method does not include waviness of the planet's surface with dimensions of irregularity significantly longer than the wavelengths. And because there are such irregularities in the RF band in the case of the moon, the use of this method to find the reflection coefficient for the lunar surface material will introduce an error, the magnitude of which will be assessed in what follows.

The expression for the planet's radar cross section will, after transformations, take the form

$$\sigma_\Sigma = [(1-x)\rho_{S_N} + 2{,}67x\bar{A}]\pi a^2. \tag{5.12}$$

The authors of this method, like Rea et al. [157], believe that only the diffuse component has a hand in reradiation at the limb. They find the diffuse component of the echo by extrapolation from the backscattering pattern from the limb to the center of the disk in accordance with Lambert's law. The coefficient μ for the diffuse component of the backscattering pattern is found from the slope of direct backscattering pattern, measured experimentally near the limb (for the moon when $\theta > 50^\circ$), that is

$$B(\theta)_d = \varkappa \cos^2\theta, \tag{5.13}$$

where

$$\varkappa = \left|\frac{B(\theta_1)}{\cos^2\theta_1}\right|, \quad \theta_1 = 50 - 90^\circ. \tag{5.14}$$

The authors of this procedure equated the normal incidence reflection coefficients, $\rho_{s\,N}$, to the albedo, averaged for all angles of incidence and polarization, $\bar{A}$, so Eq. (5.12) could be solved, but even they admit it is not satisfactory in all respects. Still, if this is not done, the equations have two unknowns and cannot be solved. The parameter x in Eq. (5.12) can be found from Eqs. (5.9), (5.11), and (5.12) in the form

$$x = \frac{\sigma_d/\sigma_\Sigma}{2{,}67 - 1{,}67\sigma_d/\sigma_\Sigma}. \tag{5.15}$$

The following expression is used in combination with the backscattering pattern, measured experimentally, to find the ratio of radar cross sections σ_d/σ_Σ /138

$$\frac{\sigma_d}{\sigma_\Sigma} = \frac{\int_0^{\pi/2} \varkappa \cos^2\theta \sin\theta\, d\theta}{\int_0^{\pi/2} B(0) \sin\theta\, d\theta}. \tag{5.16}$$

The moon's backscattering patterns were measured at the following wavelengths: 0.86, 3.6, 10, 23, 68, 600, and 1130 cm. Evans and Hagfors [108] calculated the σ_d/σ_Σ ratio, x, and $\rho_{s\,N}$ values for 0.86, 3.6, and 68 cm. They [110] and Girand [116] calculated the σ_d/σ_Σ ratio only for the other wavelengths (10, 23, 1130 cm).

The following formula can be used to find the value of $\rho_{s\,N}$ for these wavelengths using this method

$$\rho_{3N} = \frac{\sigma_\Sigma}{\pi a^2 (1 + 1{,}67x)}. \tag{5.17}$$

Table 5.1 lists the results of all calculations. The normal incidence reflection coefficients have been calculated from radar data at different wavelengths by others besides Evans and Hagfors, but they failed to cite their procedures, so we do not know if they did, or did not, include large-scale irregularities. These reflection coefficients are listed in Table 5.2. The data in these tables were used to plot the mean value of the normal

TABLE 5.1

Wavelength, cm	σ_d/σ_Σ, %	x, %	$\sigma_\Sigma/\pi a^2$, %	$\frac{\sigma_\Sigma}{\pi a^2 \rho_{sN}}$	$\rho_{s\,N}$, %	Source
0.86	85	68 (68*)	7	2.14	3.5 (3.28*)	Evans and Hagfors [108], this book
3.6	50	14 (27.4*)	7	1.46	5.5 (4.8*)	Evans and Hagfors [108], this book
10	40	20*	5	1.33	3.76*	Girand [116], this book
23	25	11.2*	6.5	1.187	5.5*	Evans and Hagfors [110], this book
68	20	8 (8.6*)	7.4	1.135	6.5 (6.5*)	Evans and Hagfors [108], this book
1130	10	4.2	19	1.07	17.7*	Girand [116], this book

Notes. * This author's calculations using the Evans and Pettengill method. $\rho_{s\,N}$ for λ = 1130 cm was obtained as much larger than that calculated by the authors of the experiment (see Table 5.2). The radar cross section value used by the authors for their calculation evidently differed from the measured value.

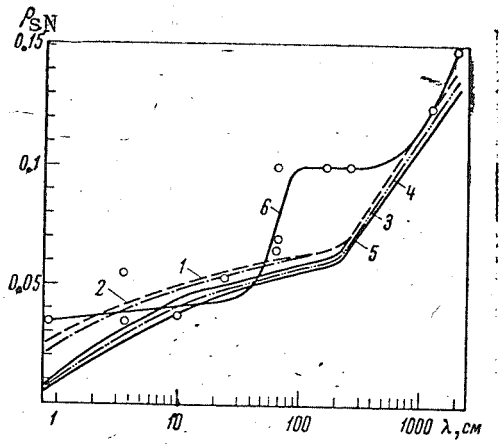

/139

Figure 5.1. The normal incidence reflection coefficient. Circles show the findings of the different authors (Table 5.2).

1 - the curve for $A_i = \rho_{s\,N}$, $g_s = 1$;

2 - for $A_i = \rho_{s\,N}$, $g_s \neq 1$; 3 - for $A_i = 0.07$, $g_s \neq 1$;

4 - for $A_i = 0.0158 * g_s \neq 1$; 5 - for $A_i = 0.375$ and 0.9, $g_s \neq 1$

6 - extrapolation of the results of findings for $\bar{\rho}_{s\,N}$ by the different authors using the least squares method.

incidence power reflection coefficient in terms of wavelength in Figure 5.1, which shows that the reflection coefficient increases with wavelength. There is a smooth rise of from 3.2 to 4.5 percent between 0.8 and 30 cm, almost no change in the mean value of the reflection coefficient, which holds at 10 percent, between 1 and 5 - 7 meters, and an increase by a factor of approximately 1.5 when the wavelength increases from 7 to 20 meters. There is an increase in the reflection coefficient by a factor of 2 between 30 cm and 1 meter. Bear in mind that the value in the decimeter and meter bands, calculated using the Evans and Pettengill method, will not be significantly larger than the $\rho_{s\,N}$ values calculated including the reflections from large-scale irregularities (see paragraph 1 of this section). /140

TABLE 5.2

Wavelength, cm	$\rho_{s\,N}$	Author of Experiment	Author of Processing	Year of Measurement
0.86	0.035	Linn	Evans and Hagfors [108]	1961
3.2	< 0.1	Kobrin	Kobrin [31]	1957
3.6	0.035	Morrow	Girand [116]	
3.6	0.055	Evans and Pettengill	Evans and Hagfors [108]	1963
10	< 0.1	Kobrin	Kobrin [31]	1954
10	0.038	Hughes	Girand [116]	1961
68	0.065	Pettengill	Evans and Hagfors [108]	1960
68	0.057	Pettengill	Rea et al. [157]	1960
73	0.07	Fricker et al.	Fricker et al. [111]	1960
75	0.1	Leadbrand	Pettengill [154]	1959
150	0.1	Trexler	Trexler [70]	1958
250	0.1	Evans	Evans [80]	1957
300	0.1	Evans	Evans et al. [59]	1959
1130	0.125	Davis and Rohlfs	Davis and Rohlfs [103]	1964
1920	0.15	Davis and Rohlfs	Krupenio [40]	1964

The Aleksandrov and Rzhiga Method

Reference [2] proposed a method for finding the reflection coefficient that was similar to that of evans and Pettengill, but included the presence of large-scale irregularities ($h \gg \lambda$). Hagfors' Eq. (2.27) was used to calculate the reflection from such irregularities. The directivity, g_s, for a wavy specular surface was determined by using the backscattering pattern for the quasispecular component of the reradiated signal [122] as follows. When the expression for the distribution law for large-scale irregularities has an exponential autocorrelation function of the form

$$\rho(d) \sim \exp(-d/d') \tag{5.18}$$

the backscattering pattern for the quasispecular component, according to Hagfors, can be approximated by a law in the form

$$B_s(\theta) = (\cos^4\theta + C_s \sin^2\theta)^{-3/2}. \tag{5.19}$$

But it must be remembered that this expression is valid for the moon when $\theta < 65^\circ$ [93] because shadowing of part of the surface by the irregularities must be included for larger θ values.

The directivity, g_s, is related to the parameter C_s in Eq. (5.19) by

$$g_s = 1 + C_s^{-1/2}. \tag{5.20}$$

The Aleksandrov and Rzhiga method expresses the radar cross section for the surface of the planet by

$$\sigma_\Sigma = [(1-x)\rho_{sN} g_s + x 2.67 A_i)]\pi a^2, \tag{5.21}$$

where

A_i is the illustrative albedo.

It is impossible to determine the value of A_i for the RF band from ground observations, so the authors of this method use an A_i value in the RF band equal to its value in the optical region ($A_i = 0.158$ [79]). However, differences in the nature of the surface roughness for different wavelengths in the RF band (see #3 of this chapter) make it impossible to take this magnitude as a constant for the different wavelengths in the RF band and equal to the value of the magnitude found for the moon in the optical region. /141

The following should be noted when comparing the three methods cited in the foregoing.

1. Inclusion of large-scale irregularities ($h \gg \lambda$) in the Hagfors formulas in the methods used by Rea et al., as well as by Aleksandrov and Rzhiga, provides a more correct presentation of reradiation from the lunar surface and provides a more precise determination of the reflection coefficient than does the Evans and Pettengill method.

2. The method used by Rea et al., is good only for processing the results of polarization measurements, whereas the overwhelming majority of the lunar measurements were made for just one component of the reradiated signal.

3. The Aleksandrov and Rzhiga method requires a knowledge of the magnitude of the illustrative albedo, something that cannot be determined in the RF band from ground observations. Moreover, this method fails to point out concrete methods for finding the specular and diffuse components of the reradiated signal.

4. The Rea et al., method can be used to find the ratio of quasi-specular and diffuse power components of the reradiated signal for polarization measurements, whereas the Evans and Pettengill method can be used to find this ratio when only one pclarized component of the incoming signal is measured.

5. Calculation of the diffuse component by the Evans and Pettengill method requires knowledge of the moon's albedo, and its dependence on wavelength in the RF band. But it is impossible to determine the albedo value from ground radar observations experimentally.

Recognizing the inadequacies inherent in the methods described, it is desirable to propose a more refined method, one that could be used to find the reflection coefficient, regardless of the signal reception method (by a single, or by two polarizations), and one that would permit of a more precise calculation of the diffuse component of the reradiated signal for single polarization measurements.

The Refined Method

Measurements of the scattering properties of different kinds of materials have shown that in the visible light region the true (Lambert) albedo of a substance has no direct connection with its reflection coefficient, as determined by the permittivity of the substance. Sugar and snow, for example, have very nearly the same true albedos, yet their permittivities are materially different. Glass, which has a reflection coefficient of a few percent, has a true albedo very nearly unity when pulverized.

The concept of the illustrative albedo, which, in planetary photometry, is determined by the ratio of the mean brightness of the disk when in its full phase to the brightness of a body of the same dimensions, but absolutely white (scattering light in accordance with Lambert's law with a true albedo equal to unity [79]), must be used to describe the properties of the scattering of radio waves in a direction opposite to that of the illumination (the radar investigation from the earth case). The illustrative albedo, A_i, is linked with the true albedo, ρ, by [79] /142

$$A_i = \frac{3}{q}\int_0^{\pi/2} \rho(\theta)\sin\theta\cos\theta\, d\theta, \tag{5.22}$$

where

$$q = 2\int_0^{\pi/2} \varphi(\alpha)\sin\alpha\, d\alpha. \tag{5.23}$$

Here q is the phase integral, $\varphi(\alpha)$ is the phase function, and α is the phase angle (the angle between the direction of incidence of the light and the direction of the observation).

The following relationships can be satisfied for the orthotropically scattering spherical surface, doing so in accordance with Lambert's law (see [79])

$$\rho(\theta) = \rho_N = \text{const}, \quad q = {}^3/_2, \quad A_i = \rho = \rho_N,$$
$$\varphi(\alpha) = \frac{1}{\pi}[\sin\alpha + (\pi - \alpha)\cos\alpha].$$

We have, for the spherical surface scattering in accordance with the Lommel-Seelinger law (see [5, 79])

$$\rho(\theta) = \rho_N [1 - \cos\theta \ln(1 + \cos\theta)], \quad q = 1.6366,$$

$$A_i = \rho_N 0.585, \quad \varphi(\alpha) = 1 - \sin\frac{\alpha}{2} \operatorname{tg}\frac{\alpha}{2} \ln \operatorname{ctg}\frac{\psi}{4},$$

where ρ_N is the true albedo for the normal incidence case.

If the true albedo is known for the normal incidence case, the value of the illustrative albedo can be determined for the Lambert and Lommel-Seelinger laws, as well as for other scattering laws.

Processing the backscattering pattern for the visible portion of the moon in the band between 0.86 cm and 11.3 meters (this book, and [109, 110]), it was found that the law for the change in the backward reradiated power with angle of incidence for the diffuse component was $B_d(\theta) \approx \cos^{3/2}\theta$; that is, the experimental curve corresponding to this law differs but slightly from the curve using Lambert's law ($B(\theta) = \cos^2\theta$).

The formulas derived to calculate the scattering of radio waves in accordance with Lambert's law can be used to process the diffuse component of the reradiated signal. This is convenient as well because the results obtained in the RF region can coincide with the results for the optical region in which all calculations of illustrative albedo were made on the assumption of diffuse scattering of light by a standard sphere according to Lambert's law. Processing radar observations from the ground provides the radar cross section and the backscattering pattern, used to calculate the quasispecular and diffuse components of the backscattering pattern, $B_s(\theta)$ and $B_d(\theta)$, and the ratio of quasispecular and diffuse components of the radar cross section for the planet to its total radar cross section, σ_d/σ_Σ and σ_s/σ_Σ. /143

The diffuse component of the radar cross section depends on the illustrative albedo, as well as on the magnitude of the area of the planet's surface producing the scattered signal

$$\sigma_d = 2.67 x A_i \pi a^2, \tag{5.24}$$

where

x is the part of the area of the planet's surface producing the scattered signal, equated to the whole of the surface area.

This equation, since it contains two unknowns, A_i and x, can be solved only when a definite assumption is made with respect to one of the unknowns.

There is no justification for considering the value of the illustrative albedo in the RF range equal to its value in the optical range (A_i = 0.158 [2]). Measurements made of the scattering characteristics of various of the earth's coverings lead to the assumption that the value of the illustrative albedo can lie between 0.07 and 0.9, with the most probable values found in the lower part of this range.

The nature of the change in A_i (for the moon) with wavelength in the optical and infrared regions also confirms that the most probable A_i value will be found in the lower part of the above range. The procedure for finding the normal incidence reflection coefficient in the RF band, therefore, will be to use Eq. (5.24) and selected A_i values to find x for each of the wavelengths in the band

$$x(\lambda) = \sigma_d(\lambda)/\pi a^2 2{,}67 A_i, \tag{5.25}$$

where

$$\sigma_d(\lambda) = \sigma_\Sigma(\lambda) \cdot \sigma_d/\sigma_\Sigma(\lambda). \tag{5.26}$$

The reflection coefficient for the normal incidence case can be found from

$$\rho_{sN}(\lambda) = \frac{\sigma_\Sigma(\lambda) - \sigma_d(\lambda)}{(1-x)\, g_s}. \tag{5.27}$$

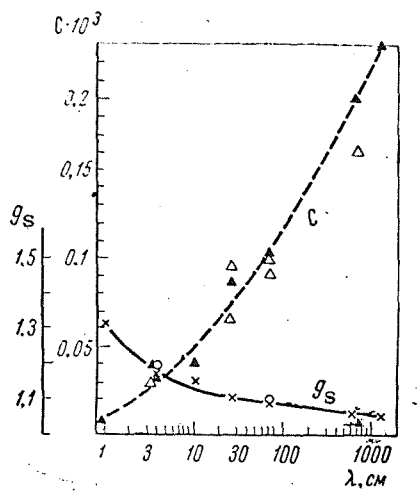

Figure 5.2. Directivity, g_s, and C_s in Eq. (5.42) in terms of wavelength.

The dependence of σ_Σ on λ is shown in Figure 4.1.

The procedure for finding ε_s is described in #3 of this chapter, and the results are shown in Figure 5.2. /144

The magnitude σ_d/σ_Σ in Eq. (5.26) can be found in different ways, depending on the method used to receive the echo. The Rea et al., method can be used for polarization measurements, the Evans and Pettengill method for measurements of one polarization. Figure 4.4 shows the results of the calculation of σ_d/σ_Σ in terms of the wavelength. The author solved Eqs. (5.25), (5.26), and (5.27) simultaneously, and obtained values for the reflection coefficient for the normal incidence case in the band of wavelengths from 0.86 cm to 20 m for discrete values of the illustrative albedo, A_i, equal to 0.07, 0.158, 0.375, and 0.9. Figure 5.1 shows these results.

A comparison of the results of the calculation made for the reflection coefficient using this method, and those from the Evans and Pettengill method, show that the value of the reflection coefficient found using both methods differs by a factor of 1.5 - 2.5 at the same wavelengths in the centimeter band, by 5 - 25 percent in the decimeter band, and by 2 - 3 percent in the meter band.

The Evans and Pettengill method is in good agreement with this method in the meter band, but does produce a significant error (2.5) at shorter wavelengths. This error occurs because the Evans and Pettengill method does not consider reflections from large-scale irregularities, and consideration of the diffuse component of the echo is not accurate enough.

2. Permittivity and Density of the Material Comprising the Moon's Upper Cover /145

Knowledge of the density and strength of the moon's surface layer is of great practical importance for planning the landing devices used for space vehicles, and the machines for moving about over the lunar surface. Here a great achievement of Soviet radiophysicists was to prove that Gold's dust hypothesis, according to which the moon should have been covered with many meters of unconsolidated, finely dispersed, dust, was unfounded. It would have been a practical impossibility to have landed and moved about on this surface. The first direct measurements, those made by Luna 9, fully confirmed

the conclusions of the Soviet radiophysicists, who had used indirect observations to find the density of the moon's upper cover.

Precision radioastronomy observations of the moon from the earth in the centimeter and decimeter bands, made under the supervision of V. S. Troitskiy, provided the means for measuring the radio-brightness temperature during lunations and eclipses. The only way to explain the nature of the change found in the radio-brightness temperature is to attribute it to the low thermal conductivity of the material of the moon's upper cover. Earth rocks with low thermal conductivity are silicate rocks. But, if earth silicate rocks are to have the same thermal characteristics under lunar conditions as moon rocks, they should be quite porous at shallow depths, and, consequently, not very dense.

Subsequent experiments using Luna 9, Luna 10, Luna 13, Surveyor 5, Surveyor 6, and Surveyor 7 completely confirmed the silicate composition of the material on the lunar surface, as well as the density values of that material, preliminarily estimated from radar and radioastronomy observations from the ground.

Numerous measurements of the permittivities of a variety of earth rocks enabled V. D. Krotikov [37] to obtain an empirical formula for silicate rocks that links the density of the material, ρ_d, with its permittivity

$$\rho_d = (\sqrt{\varepsilon} - 1)/a \ , \tag{5.28}$$

where

$$a \approx 0.5.$$

There have been several recent experiments designed to investigate the properties of earth rocks under conditions close to those found on the moon. B. W. Hapke [127], for example, has shown that rocks found on the lunar surface have optical characteristics very nearly like those of earth basalt after proton and meteor bombardments. Campbell [98] expanded the use of Krotikov's formula to include a great many other earth minerals and igneous rocks. /146

Recent research on the electromagnetic and physical characteristics of moon-like materials (Junites) has revealed that the parameter a in Eq. (5.28)

changes somewhat in the RF band, increasing from a = 0.5 at λ = 0.8 cm to a = 0.6 at λ = 30 m [12]. Figure 5.3 shows a in terms of λ, from data in [12].

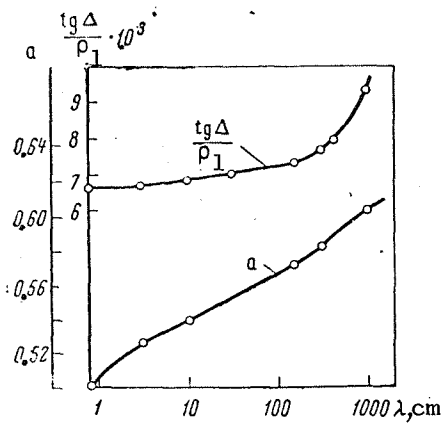

Figure 5.3. Electrical characteristics of the moon's upper cover from modeling.

As we know, the depth to which radio waves will penetrate into a material is fixed by the material's conductivity and permittivity at the particular wavelength. If material properties remain constant with depth, the depth to which radio waves will penetrate l_{el} (the depth of the "skin layer" at which the electromagnetic field is attenuated by a factor of e) can be found from

$$l_{el} = \frac{\lambda}{2\pi \operatorname{tg}\Delta \sqrt{\varepsilon}}, \tag{5.29}$$

where

Δ is the loss angle, equal to

$$\Delta = \operatorname{arc\,tg} \frac{2\sigma_c \lambda}{c\varepsilon}. \tag{5.30}$$

where

σ_c is the conductivity of the material [$ohm^{-1} \cdot m^{-1}$];

c is the speed of light [m/sec].

When, therefore, ε and σ_c are known in terms of the wavelength, a model of the lunar surface layer can be built by using Eqs. (5.28) - (5.30). But, because Eq. (5.29) is valid only for a material with properties that remain

constant with depth, the model thus built will be a crude one, purely tentative in nature, because depth distribution of the electromagnetic field will change with change in the electromagnetic properties of the material, and this will result in a change in "skin layer" thickness. /147

It should be pointed out that no one yet has found a precise solution to the problem of the propagation of radio waves in the depth of a material, one involving a complex law of change in the electromagnetic characteristics of a material with depth, as is the case for the moon, although such attempts have been made.

It is customary to turn this problem around, that is, to solve it for the reflectivity for the normal incidence case by giving the law of change in density of a material with depth and using the Riccati differential equation. T. V. Tikhonova and V. S. Troitskiy [69] solved this problem for certain models of the surface layer with linear and exponential laws of change in density with depth. The model selected for this solution as being the most reliable is one for which the theoretical relationship between reflectivity and wavelength is closest to the experimental relationship. Hence, use of this method of calculating the lunar surface layer model, because of the results obtained from processing radar data, requires finding the normal incidence reflectivity in terms of the wavelength, and then finding the value of the effective permittivity of the surface layer material corresponding to this reflectivity, because this value must be known in order to compare the radar data with the radioastronomy data for the same wavelengths. In what follows we shall consider only the relationship between the electrical parameters of the material of the lunar surface cover and the wavelength of the illuminating flux, and not the depth to which it penetrates. This approach will, in what follows, enable us to use Eq. (5.29) to make a rough approximation of the thickness of the layer with the above-indicated characteristics.

The research reported in references [12, 37] shows that a material that has the properties of the material of the lunar surface cover is a good dielectric, one for which the specific tangent of the loss angle ($\tan \Delta / \rho_1$) in the centimeter and decimeter bands has little relationship to the wavelength, and experiences but a slight increase in the decameter band (see

Figure 5.3). The last measurements of the magnetic field, and of the solar wind flux, made by Explorer 35 [54], revealed that the magnitude of the ratio of the rate of flow of the magnetic field through the body of the moon to the solar wind convection rate fixes the upper limit of the moon's effective conductivity, and that it is equal to 10^{-5}ohm^{-1}m^{-1}.

Magnetic field measurements near the moon, and on its surface, have shown that the moon's own magnetic field is slight, and that the permeability of /148
the lunar material is very nearly unity [24, 54, 152]. So, with what has been said as a base, the moon can be represented quite accurately as a body, the material of the upper cover of which is virtually a perfect dielectric.

Let us now use the results of the calculation made for the reflectivity of the lunar surface layer in #1 of this chapter, and the frequency relationships for the parameter a in Eq. (5.28), as well as the results of the model investigations of the tan Δ for ground analogues of moon rocks in the RF band [12], to find the permittivity and the density of the material of which lunar upper cover is made at depths corresponding to the "skin layer" thickness for wavelengths from 0.8 cm to 19 m. The permittivity of this material can be calculated from the value of the reflectivity found above by using the formula

$$\varepsilon = \left(\frac{\sqrt{\rho_{SN}}+1}{\sqrt{\rho_{SN}}-1}\right)^2. \qquad (5.31)$$

The value of $\rho_{s\,N}$ increases at longer wavelengths, and this leads to an increase in permittivity with increase in wavelength. The calculation made for depth of penetration of electromagnetic waves by Eq. (5.29), and including the relationship between ε and tan Δ and λ, shows increase in t_{el} with increase in the wavelength, pointing to an increase in material density with depth. The results of these calculations are shown in Figures 1.8, 5.3, and 5.4, which show the parameters ε, a, tan Δ/ρ_c, ρ_c, and t_{el} in terms of the /149
wavelength. The results of these calculations, and those obtained by using other methods, will be discussed in #4 of this chapter.

3. Surface Slopes

The characteristics of reradiation from the surface layer depend on the structure of the surface of that layer, as well as on the electrical properties

of the moon's upper cover. And, as has been pointed out above, the backscattering pattern is the most sensitive of all reradiation characteristics to surface structure.

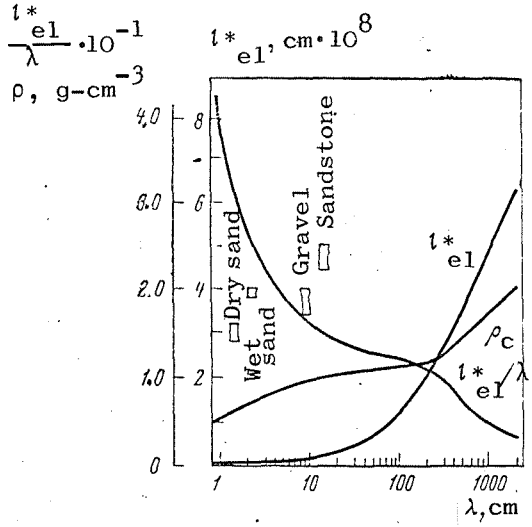

Figure 5.4. Density of the material of the lunar upper cover and depth of penetration of radio waves into the depth of the lunar surface layer in terms of the wavelength. Penetration depth for each wavelength is for a homogeneous material with a density that of the mean density for the particular wavelength.

The nature of the reradiation of radio waves depends on the dimensions of the irregularities relative to the wavelength, as well as on the law of distribution of surface irregularities. And irregularities, the dimensions of which exceed the wavelength of the illumination are of the most interest because including them in the calculations results in a more precise determination of the Fresnel coefficient, the permittivity, and the density of the material of the moon's upper cover, as well as of the statistical properties of surfaces ranging in size from a few centimeters to several meters. Knowledge of the irregularities on the lunar surface, found from statistical characteristics of the surface, are particularly important when planning landings for spacecraft, and vehicles for traveling about on the lunar surface.

Today's methods for calculating the reflections of radio waves from large irregularities are based on two theories, one of which is Kirchhoff's theory of physical optics, and the other is the much simpler theory of geometric optics.

Hagfors [123] compared the results of using Kirchhoff's formulas with the results obtained after using geometric optics formulas, and found but a slight difference in the slopes thus obtained. This was practical proof of the acceptability of using the simpler method of geometric optics to find the reradiation from large irregularities on the lunar surface. References [150, 157] develop the geometric optics method as applicable to reflection from the moon and the planets.

When one considers the reradiation of radio waves from the surface of a planet in terms of geometric optics, it is easy to see that the greater the range of depression angles individual reflectors on the spherical surface have to the surface of the sphere, the more conditions for signal reception are satisfied for a large range of angles of incidence.

Thus, information on depression angles of reflectors relative to the spherical surface of the planet will be available in accordance with the ratio of the power of the quasispecular component of the echo to the angle of incidence. /150

If it is assumed that the electrical properties of the material of the planet's upper cover are constant at any point on the planet, that is, they do not depend on the planetocentric coordinates, then the statistical characteristics of the irregularities of the surface under investigation can be determined.

It is the reverse of this problem that is solved to determine the slopes of surfaces, using either of the methods. Here the statistical law is applied to assign distributions of irregularities for different values of a mean, or root-mean-square, depression angle, and thus obtain backscattering patterns for the planet for the quasispecular components of the echo corresponding to these angles. The set of theoretical backscattering patterns then is used to select the pattern most closely resembling the quasispecular component of the experimental backscattering pattern. The corresponding value of the parameter characterizing the slope of the surface thus is found.

A model with a random law for the distribution of heights and slopes of large surface irregularities with autocorrelation functions determined by the

exponential law, Eqs. (5.32) and (5.33), or by the Gaussian law, Eqs. (5.34) and (5.35), can be used as the model for making these calculations

$$\rho(l) \sim \exp(-l/l_0), \tag{5.32}$$
$$\rho(h) \sim \exp(-h/h_0), \tag{5.33}$$
$$\rho(l) \sim \exp\left[-\frac{1}{2}(l/l_0)^2\right], \tag{5.34}$$
$$\rho(h) \sim \exp\left[-\frac{1}{2}(h/h_0)^2\right], \tag{5.35}$$

where

l_0, h_0 are the characteristic dimensions of the irregularities along the surface and in height;

l, h are the deviations along the surface and in height.

The root-mean-square slope of the surface is found for the exponential autocorrelation function, and the mean slope is found for the Gaussian [109, 121].

The results of measurements at wavelengths of 3.6, 68, and 185 cm provide an approximation of the quasispecular component of the backscattering pattern when the exponential autocorrelation function is used [21, 109]. Measurement of echo characteristics for different ground structures has shown that here too the closest correspondence between the theoretical and the experimental quasispecular components of the backscattering patterns is obtained when the exponential autocorrelation function is used [101, 129, 132, 133].

The backscattering pattern, $B_s(\theta)$, will correspond to the univariate law of distribution of slopes for a spherical surface, $f(\theta)$, when the geometric-optical approximation is used. The connection between $f(\theta)$ and $B_s(\theta)$ can be expressed by [109]

$$f(0)\,\Delta l\,\Delta\theta \simeq B_s(\theta)\cos\theta\,\Delta\theta, \tag{5.36}$$

/151

where

Δl is the size of the area with slope between θ and $\theta + \theta$.

And it is understood that the Fresnel coefficient does not depend on planetocentric coordinates. Since the law of distribution of slopes for the particular section of the surface can differ for different vertical sections, this law must be averaged for all vertical sections passing through the particular point on the surface. The integration by sphere of Eq. (5.36) will result in

the finding of the mean depression angle for large irregularities (shadowing not considered), with the averaging mentioned included. Reference [121] has it that the mean depression angle for large irregularities can be found from

$$\theta_m = \frac{\int_0 \theta B_S(\theta) \cos\theta \sin\theta \, d\theta}{\int_0 B_S(\theta) \cos\theta \sin\theta \, d\theta}. \tag{5.37}$$

Hagfors [121, 122] solved the problem of reradiation of radio waves by a surface with large irregularities, and thus obtained simpler formulas connecting the quasispecular component of the backscattering pattern with the mean and root-mean-square depression angles for the surface. In doing so, Hagfors used an approximation of the quasispecular component of the backscattering pattern

$$B_S(\theta) = (\cos^4\theta + C_S \sin^2\theta)^{-3/2}, \tag{5.38}$$

where

$$C_S = (l_0\lambda/4\pi h_0^2)^2. \tag{5.39}$$

Hagfors then derived the following formula for the mean depression angles for the surface

$$\operatorname{tg}\theta \simeq \frac{1}{2\sqrt{C_S}} \frac{C_S - 4}{C_S - \sqrt{C_S} - 2} \ln 4C_S. \tag{5.40}$$

This formula, as [109] has shown, is valid for $C_S > 100$, which, for the moon, corresponds to wavelengths longer than 1 m. The mean depression angle for the surface can be found with this formula for a base of the order of 10 wavelengths.

Hagfors derived the following formula to find the root-mean-square depression angles, σ_α, for the same approximation as that used in Eq. (5.38)

$$\sigma_\alpha = \operatorname{arc\,tg} C_S^{-\frac{1}{4}}. \tag{5.41}$$

/152

He included Eqs. (2.27) and (2.28) in his derivation of this formula.

The magnitude of the parameter C_S in Eq. (5.38) determines the directivity, g_S, for large irregularities, as well as the value of the mean and

root-mean-square depression angles. The relationship between the directivity and C_s is fixed by the formula [122]

$$g_s = 1 + 1/\sqrt{C_s} \qquad (5.42)$$

We can find the mean and the root-mean-square depression angles for the lunar surface, listed in Table 5.3, as well as the directivity, g_s, by approximating the quasispecular components of the experimentally measured backscattering patterns at wavelengths of 0,86, 3.6, 10, 23, 68, 600, and 1130 cm by Eq. (5.38) (Figures 5.5 - 5.11), and determining the magnitude of C_s for them by using Eqs. (5.40) - (5.42). The results of the calculation of these parameters are shown in Figures 5.2 and 1.1. There are other ways to calculate the slopes of large irregularities of a surface, and one is the polarization measurement method.

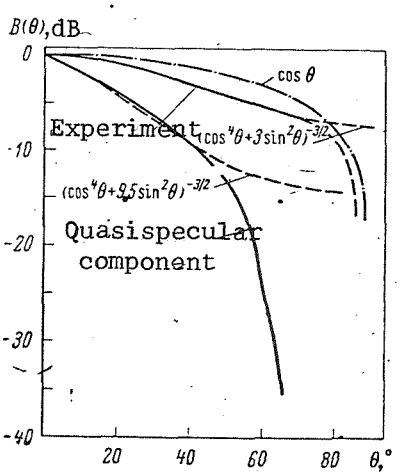

Figure 5.5. Experimental backscattering pattern for the moon at λ = 0.86 cm and its quasispecular component.

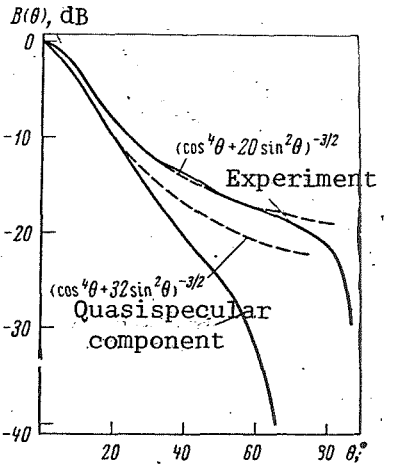

Figure 5.6. Experimental backscattering pattern for the moon at λ = 3.6 cm and its quasispecular component.

Beckmann [94] found the value of σ_α and ϵ by using Hagfor's [124] theoretical dependencies of the polarization factor for the echo from a surface with large irregularities on the permittivity and root-mean-square of the surface slope, σ_α, as well as by making experimental measurements of the dependence of the polarization factor on the angle of incidence at λ = 23 cm [110] for the specified wavelength. /153

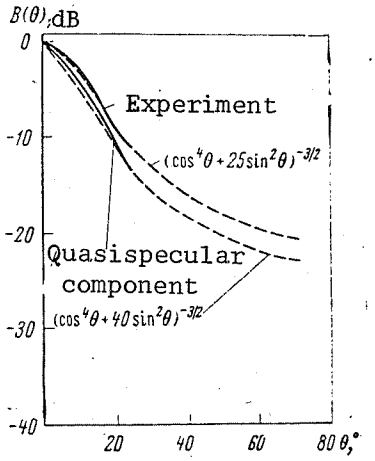

Figure 5.7. Experimental backscattering pattern for the moon at λ = 10 cm and its quasispecular component.

TABLE 5.3

Wavelength, cm	C_s	$C_s^{-\frac{1}{2}}$	σ_α, deg	$\bar{\alpha}$, deg
0.86	9.5	0.325	18.6	--
3.6	32	0.177	10	--
10	40	0.158	9	--
23	86	0.108	6.2	--
68	102	0.098	5.6	9.1
600	200	0.07	4.1	7.4
1130	230	0.066	3.8	6

Hagfors established the fact that the theoretical curves for the polarization factor at angles of incidence smaller than 35° depend more heavily on ε, than on the magnitude of the depression angle, and thus was able to find ε by analyzing the polarization factor curves for small angles of incidence. Analysis of these same curves for large angles of incidence made it possible to calculate the value of the depression angles.

Reference [82] proposed a method for finding the permittivity and the depression angles for a surface from the nature of the change in the radiation coefficient for a spherical surface with angle of incidence. The theoretical bases needed were taken from reference [64]. The authors used the

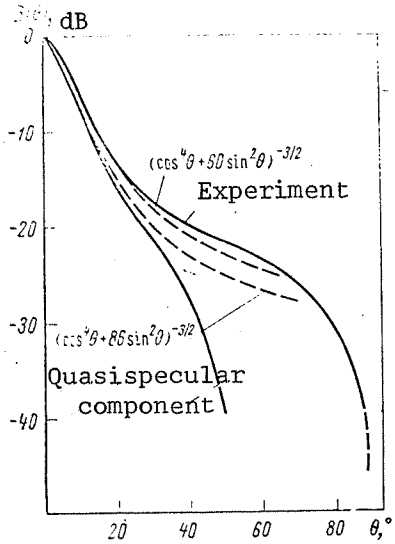

Figure 5.8. Experimental backscattering pattern for the moon at λ = 23 cm and its quasispecular component.

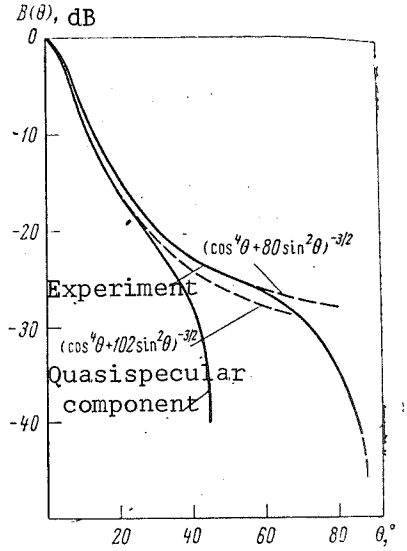

Figure 5.9. Experimental backscattering pattern for the moon at λ = 68 cm and its quasispecular component.

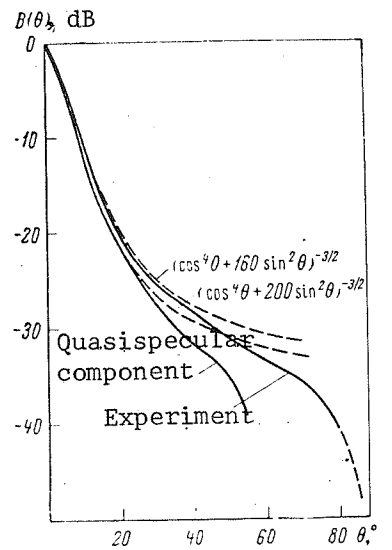

Figure 5.10. Experimental backscattering pattern for the moon at λ = 600 cm and its quasispecular component.

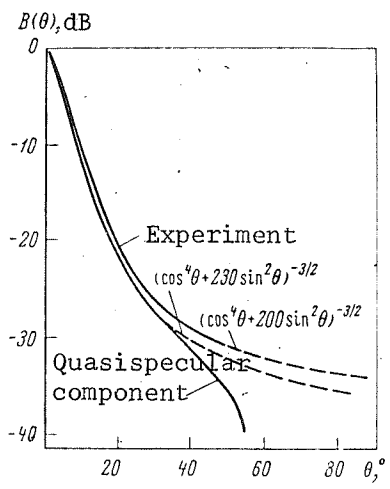

Figure 5.11. Experimental backscattering pattern for the moon at λ = 1130 cm and its quasispecular component.

proposed method to investigate the reflection of radio waves from the lunar surface during radiation of unmodulated oscillations from an artificial moon satellite, with reception of direct and reflected signals taking place at a ground station. Some authors have considered all of the reradiated signal in analyzing the characteristics of reradiation, rather than just the quasi-specular component, and this has resulted in mistaken values in their calculations of depression angles for the lunar surface. The results of the determination of the slopes of the lunar surface from radar data obtained from the ground, as well as from satellites, are listed in Table 5.4. /155

As we see, the lunar surface, on the average, is quite smooth, with the mean for depression angles a maximum 15° on a base longer than 40 cm, and with root-mean-square depression angles a maximum of 20° on this same base. The root-mean-square depression angles were 19° (base ~ 10 cm) when backscattering patterns at $\lambda = 0.86$ cm were processed. These larger depression angles can be explained by the effect of small rocks, of the order of 10 cm in size, on the lunar surface, as well as by the effect of the large internal depression angles of small depressions, those with diameters of about 10 to 70 cm.

4. Comparison of Results of Determining the Physical Characteristics of a Surface and a Surface Layer by Radar and Other Methods.

The resulting effect of measuring the polarization factor of thermal radiation in the RF band [66, 72] depends on ε, θ, and σ_α for the section of the surface investigated. By plotting the polarization factor in terms of the depression angle for different combinations of ε and σ_α values, and then comparing these families of theoretical curves with experimentally measured relationships between the polarization factor and the angle of incidence to select the corresponding values of σ_α and ε. It should be noted that the magnitude of the polarization factor at angles of incidence close to the normal is very small and shows no great increase until values are in excess of 35° to 45°. Still, the absolute magnitude of the polarization factor at small angles of incidence depends more on the value of ε, than on the value of σ_α, and this enables us to determine the magnitude of ε from the ratio of the polarization factor to the angle of incidence at small θ, and to determine the value of σ_α from the value of ε for large θ.

TABLE 5.4

/156

Wavelength, cm	Magnitude of mean slopes, $\bar{\alpha}$, deg	Magnitude of root-mean-square slopes, σ_{α}, deg	Author of Experiment	Author of Processing	Notes
0.86	--	10	Linn et al. [143, 144]	Beckmann [93]	
		18.6	Linn et al. [143, 144]	This book	
3.6	8	10	Evans, Pettengill [107]	Evans, Pettengill [107]	
3.6	15	--	Evans, Pettengill [107]	Evans, Hagfors [110]	
3.6	19	--	Evans, Pettengill [107]	Muhleman [150]	Including diffuse component
3.6	--	10	Evans, Pettengill [107]	This book	
10	3	--	Hay, Hughes (see [59])	Hay, Hughes (see [59])	
10	--	3	Hay, Hughes (see [59])	Evans [109]	
10	--	3	Hay, Hughes (see [59])	Hagfors [120]	
10	15	--	Hay, Hughes (see [59])	Muhleman [150]	
10	--	9	Hay, Hughes (see [59])	This book	
23	10	--	Evans, Hagfors [110]	Evans, Hagfors [110]	
23	--	13	Evans, Hagfors [110]	Beckmann [94]	
23	--	6.2	Evans, Hagfors [110]	This book	
68	8-12	--	Pettengill [154]	Daniels [101]	Including diffuse component
68	7	8	Pettengill [154]	Muhleman [150]	
68	11	14	Pettengill [154]	Daniels [100]	Including diffuse component
68	11	15	Evans, Pettengill [107]	Rea, Hethering, Mifflin [157]	
68	5	4.5	Evans, Pettengill [107]	Evans, Pettengill [107]	
68	10	--	Evans, Pettengill [107]	Evans, Hagfors [110]	

TABLE 5.4 (continued)

Wavelength, cm	Magnitude of mean slopes, $\bar{\alpha}$, deg	Magnitude of root-mean-square slopes, σ_α, deg	Author of Experiment	Author of Processing	Notes
68	---	11.2	Evans, Pettengill [107]	Beckmann [91]	
68	---	6	Evans, Pettengill [107]	Hagfors [120]	
68	9.1	5.6	Evans, Pettengill [10]	This book	
70	14	---	Evans (see [109])	Daniels [100]	
70	6.5	---	Evans (see [109])	Daniels [102]	Including diffuse component
170	6	3-14	Yakovlev, Yefimov, et al. [82, 83]	Yakovlev, Yefimov, et al. [82, 83]	Artificial moon satellite data
185	10	---	Getmantsev, et al. [21]	Getmantsev, et al. [21]	
250	---	6	Evans (see [109])	Hargreaves [128]	
300	---	4	Evans, et al. (see [109])	Hagfors [120]	
600	7.4	4.1	Klemperer [139]	This book	
1130	6	3.8	Davis, Rohlfs [103]	This book	

Radioastronomy data were obtained for the moon at wavelengths of 0.8, 2.05, and 3.2 cm. It also is possible to determine ϵ and σ_α from measurements to determine the disk radio brightness temperature. This method was used to investigate the moon at wavelengths of 6, 11.3, and 21 cm. The results of all of the above-cited radioastronomy measurements are listed in Table 5.5. /157

TABLE 5.5

Wavelength, cm	Permittivity, ε	Mean Depression angle, $\bar{\alpha}°$	Author of Experiment	Author of Processing	Notes
0.4	~1.5	--	Salomonovich [163]	Salomonovich [163]	
0.8	~1.5	--	Salomonovich [163]	Salomonovich [163]	
0.8	1.5±0.2	15±10	Losovskiy [49]	Losovskiy [49]	
	2.3±0.5	15±10	Losovskiy [49]	Losovskiy [49]	Including diffuse component of radiation
0.86	1.5	--	Moran, Staelin [149]	Moran, Staelin [149]	
1.6	1.5	20	Baars [86]	Krotikov [73]	
2.0	~1.5	--	Salomonovich [163]	Salomonovich [163]	
2.05	1.8	0	Baars, Metzger et al. [87]	Baars, Metzger et al. [87]	Center of disk (to 0.6a)
	1.5	0 - 15	Baars, Metzger et al. [87]	Baars, Metzger et al. [87]	Limb [(0.6 to 0.9) a]
3.2	1.65	0 - 20	Soboleva [66]	Soboleva [66]	
	1.5	20	Soboleva [66]	Krotikov [73]	
3.2	~1.5	--	Salomonovich [163]	Salomonovich [163]	
	1.5±0.3	--	Krotikov, Troitskiy [38]	Krotikov, Troitskiy [38]	
6.0	2.2±0.1	8 - 16	Davies, Gardner [104]	Davies, Gardner [104]	
6.3	2.0±0.3	--	Gol'nev, Soboleva [22]	Gol'nev, Soboleva [22]	
11.3	2.25± 0.05	8 - 16	Davies, Gardner [104]	Davies, Gardner [104]	
21.0	2.25± 0.05	8 - 16	Davies, Gardner [104]	Davies, Gardner [104]	
21.0	2.1	--	Heiles, Drake [130]	Heiles, Drake [130]	

The following conclusions derive from a comparison of the results of measuring the effective permittivity by radioastronomy methods with those from determining the values of ε on the corresponding wavelengths from radar data (see Figure 1.8).

1. The effective permittivity of the material comprising the moon's upper cover increases with the wavelength.

2. The effective permittivity changes slightly in the band of wavelengths from 10 to 200 cm, but there is a rapid rise in ϵ with the wavelength above 200 cm. /158

3. Permittivity values, determined experimentally by using radioastronomy measures, are in good coincidence with ϵ values calculated from radar data when the calculations were for the normal incidence reflection factor using the method described in #1 of this chapter.

4. What follows from comparing the results of finding ϵ by radar and radioastronomy methods is that the illustrative albedo, A_i, value for the lunar surface in the RF band can be between 0.07 and 0.375, and this differs from the A_i value for the visible light band by no more than a factor of 2.

5. The change in the magnitude of the effective permittivity, and, as a result, in that of the normal incidence reflection factor, is insignificant when A_i changes within the above-indicated limits.

As we have said, the depth to which radio waves will penetrate (the thickness of the "skin layer") depends on the mean values of permittivity and conductivity for the material, as well as on the law in accordance with which they are distributed with depth. Judging from the curves of change in $\epsilon \tan\Delta/\rho_1$ with wavelength (Figures 1.8 and 5.3), the properties of the surface layer material must change with depth. The results of direct measurements of lunar soil material density and strength at different depths also point in this direction. These measurements were made during experiments conducted by automatic stations that were landed on the lunar surface. Hence, there is no way to make a precise calculation of the depth of penetration of radio waves by using Eq. (5.29). Nevertheless, this equation can be used to make a very rough estimate of the thickness of the "skin layer" (with an accuracy of 1 to 1.5 orders of magnitude). The use of Eq. (5.28) to find the relationship between the effective density of the surface layer material and corresponding wavelengths yields data that can be compared with the depth to which radiation at these same wavelengths penetrates the moon, and in this way obtain what is a purely estimating model of the lunar surface layer. A

more accurate model can be obtained by using our relationship between the reflection factor and the wavelength (Figure 5.1), and then comparing this relationship with the family of theoretical curves for the reflection factor as a function of the wavelength obtained by solving the problem of the reflection of radio waves of different frequencies from a model of the surface layer, which is a set of individual layers with different densities, and different change laws.

As will be seen from the preceding comparison of the results of determining the relationship between the reflection factor and the wavelength by radar and radioastronomy methods, we can select the relationship when A_i = 0.158 (see Figure 5.1) as the mean relationship, $\rho_{s\,N} = f(\alpha)$. This A_i value was used to plot the density of the surface layer material, ρ_s, and of the depth of penetration of radio waves, t_{el}, in terms of wavelength in Figure 5.4. Note that between 0.8 cm and 20 m the depth of penetration of radio waves, calculated using Eq. (5.29), changes from tens of centimeters to tens of meters, which is ~30 wavelengths in the centimeter band, and 5 wavelengths in the decameter band. /159

The combining of $\rho_s(\lambda)$ and $t_{el}(\lambda)$ results in a rough estimate of the change in the density of the lunar surface layer material with depth. This estimate shows an increase in density from $\rho_s \approx 0.5$ g/cm^3 at the surface to $\rho_s > 2$ g/cm^3 at a depth of a few meters.

Calculations for a two-layer model of the moon's upper cover, using an exponential law of change in density with depth for $\rho_{surface} = 0.6$ g/cm^3 and $\rho_{sublayer} = 2.5$ g/cm^3, provided a value for the depth of the "plowed" layer of $t \approx 1.5$ m. This calculation was made for $\rho_{s\,N} = f(\lambda)$, when $A_1 = 0.158$, shown in Figure 5.1.

The data obtained from experiments conducted by automatic stations confirmed the change in density and porosity of the material of the moon's upper cover with depth. Surveyor 3 data show the density and porosity, respectively, as equal to 1 g/cm and 70 percent at a depth of a few millimeters, 1.5 g/cm^3 and 40 - 50 percent at a depth of 5 cm, and 1.8 - 2 g/cm^3 and < 40 percent at a depth of 10 cm.

The depth of the "plowed" layer, based on estimates of the results of the measurements made by the automatic stations in the Surveyor series, vary from 1 to 20 meters in the maria regions investigated, and is a maximum of 1 meter in the continental region near the crater Tycho, the landing site of Surveyor 7. It can exceed 1 meter in other continental regions [85]. Ranger series photography provides an estimate of the depth of the "plowed" layer of 10 - 20 m [161, 171].

Data on density of the material of the moon's upper cover also were obtained at the Luna 13 and Surveyor 7 landing sites. Luna 13 data show the mean density of the upper 5 cm layer to be approximately $\rho_s = 0.8$ g/cm^3, and Surveyor 7 data provide a mean of $\rho_s \simeq 1.5$ g/cm^3 for the layer 5 - 10 cm thick. The experiments conducted by Surveyor 7 found the density of one of the rocks on the surface to be $\rho_s = 2.5 - 3.3$ g/cm^3. Similar results were obtained from measurements made of the density of soil and rock samples brought back by Apollo 11. Gold's preliminary report has the density of the rocks varying between $\rho_s = 2.5 - 3.3$ g/cm^3, and that of the upper soil layer approximately equal to $\rho_s = 1.2$ g/cm^3. These latter figures can be inflated somewhat because of the possibility of soil impaction attributable to vibration during transportation, and to change in external conditions. /160

Luna 11, Luna 14, and Explorer 35 conducted radar experiments leading to an estimate of the permittivity of the upper cover for different regions of the moon. Krotikov's formula, Eq. (5.28), was used to find the density of the material from the data obtained for ϵ in these two experiments, and the value of a corresponding to the given wavelength. Table 5.6 lists the results. Ground radar data (see Figure 1.8) for these wavelengths show that when $\lambda = 1.7$ m, $\bar{\epsilon} = 2.75$ and $\bar{\rho}_s = 1.16$ g/cm^3, and that when $\lambda = 2.2$ m, $\bar{\epsilon} = 2.85$ and $\bar{\rho}_s = 1.21$ g/cm^3.

Thus, ground radar data and the results of space experiments are in good agreement. Judging from these experiments, the magnitude of the density of the material of the moon's upper cover can be lower by a factor of 1.5 in some regions, and higher by a factor of 2.2 in others, than the mean density of the material of the moon's surface layer.

Radar experiments conducted by the automatic stations in the Luna and Surveyor series landed on the lunar surface provided $\sigma_{0\,N}$ and the

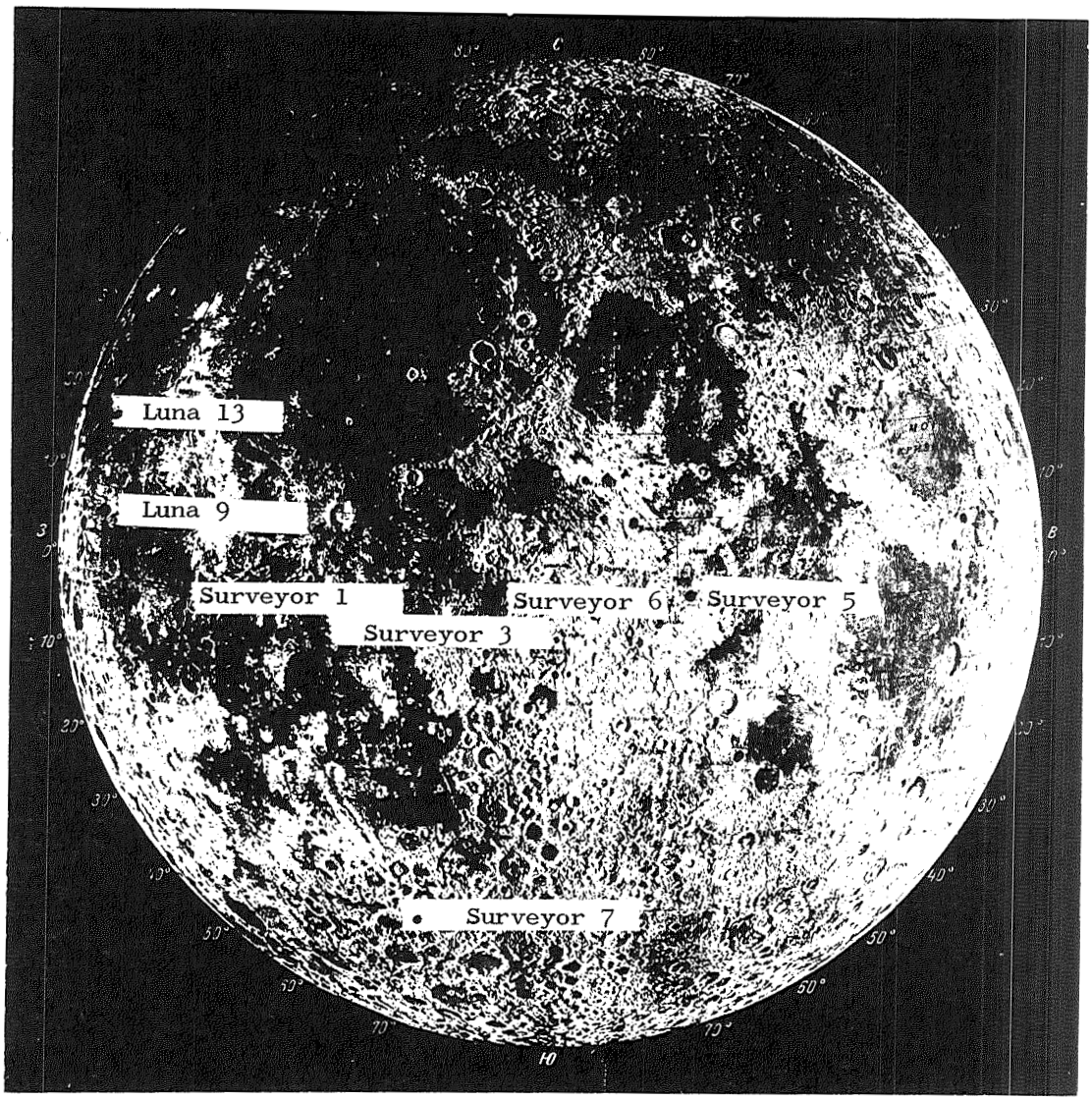

Figure 5.12. Sites of landings of automatic stations on the lunar surface.

TABLE 5.6

Spacecraft	Wave-length, cm	ϵ	a	Density of material, ρ_s, g/cm^{-3}	$\frac{\rho_s}{\bar{\rho}_s}$	Measurement region
Luna 11	170	2.7 - 3.0	0.57	1.14 - 1.28	0.98 - 1.11	Maria and continents
Luna 12						
Luna 14	170	2.8 - 3	0.57	1.18 - 1.28	1.02 - 1.11	Maria and continents
	17	2 - 6	0.57	0.72 - 2.55	0.62 - 2.2	Maximum variations in individual regions
Explorer 35	220	2.8	0.57	1.18	0.975	Continents
	220	3.2	0.57	1.39	1.18	Maria
	220	5.6 - 6.1	0.57	2.38 - 2.58	2.02 - 2.18	Region of the crater Flamsteed

backscattering patterns for local regions of the moon. In the case of the maria regions (the landing sites of Surveyor 3, Surveyor 5, and Surveyor 6), the backscattering patterns, $B_0(\theta)$, differ little from those for the moon, $B(\theta)$, obtained from ground radar data on the moon. The only significant difference was recorded for the mountainous region near the crater Tycho, where the nature of the scattering corresponded to a rougher surface than is the average for the moon.

The reflectivity, as was pointed out in #2 of Chapter II, depends on the surface albedo. But it is possible to determine the magnitude of $\rho_{s\,N}$ when measuring the reflectivity for normal incidence /161

$$\rho_{sN} \approx \frac{\sigma_{0N}}{2} \int_0^{\pi/2} B_{s0}(\theta) \operatorname{tg} \dot{\theta}\, d\theta. \qquad (5.43)$$

Here $B_{s0}(\theta)$ is the quasispecular component of the backscattering pattern for the local region of the surface, and it can be approximated by the law

$$B_{s0}(\theta) = (\cos^4 \theta + C_{s0} \sin^2 \theta)^{-3/2}. \qquad (5.44)$$

$B_{s0}(\theta)$ can be obtained from the backscattering pattern for this region in the same way that the quasispecular components of the moon's backscattering patterns were calculated. These calculations showed that the coefficient C_{s0} equals 23 for the Surveyor 3, Surveyor 5, and Surveyor 6 landing sites, and 15 for the Surveyor 7 landing site. If it is taken that the backscattering patterns at the Luna 9, Luna 13, and Surveyor 1 landing sites coincide with the moon's backscattering patterns on the corresponding wavelengths, the coefficient C_{s0} will equal 35 for the Luna 9 and Luna 13 landing sites, and 23 for the Surveyor 1 landing site. Figure 5.12 shows the landing sites.

Table 5.7 lists the results of the calculations made for the landing sites for the Luna and Surveyor series, and includes the accuracy with which $\sigma_{0\,N}$ was determined, ±3 dB. The values of permittivity and density of the material were calculated from the $\rho_{s\,N}$ value, using Eqs. (5.1) and (5.28) [140].

TABLE 5.7

Spacecraft	$\sigma_{0\,N}$	C	C_{s0}	$\rho_{s\,N}$	ϵ	ρ_s, g/cm^3	$\rho_{s\,mean}$, g/cm^3	Π_{mean}
Luna 9	0.5	-	35	0.023-0.094	1.85-3.6	0.75-1.8	1.1	0.666
Luna 13	1.0	-	35	0.048-0.19	2.4 -6.5	1.1 -3.1	1.8	0.453
Surveyor 1	0.25	-	23	0.02 -0.08	1.8 -3.25	0.7 -1.6	1.0	0.67
Surveyor 3	0.2	10	23	0.015-0.062	1.7 -2.75	0.64-1.34	0.88	0.733
Surveyor 5	0.16	10	23	0.012-0.05	1.85-2.5	0.6 -1.2	0.8	0.757
Surveyor 6	0.2	10	23	0.015-0.062	1.7 -2.75	0.64-1.34	0.88	0.733
Surveyor 7	0.4	5	15	0.04 -0.16	2.25-5.3	1.0 -2.62	1.6	0.515

Measurement of the physical properties of the moon rocks gathered by the Apollo 11 astronauts revealed that their maximum density is $\rho_{s_{max}} = 3.3$ g/cm^3, and this coincides with the value of this parameter found from experiments performed by Surveyor 7. So, by taking the density of the basic rocks as $\rho_{s0} = 3.3$ g/cm^3, and the porosity as equal to 0, we can find the mean porosity, Π, of the material of the moon's upper cover at the landing sites of the automatic stations in the Luna and Surveyor series from the formula /162

$$\Pi_m = \left(1 - \frac{\rho_s}{\rho_{s_0}}\right). \qquad (5.45)$$

The results, listed in Table 5.7, show that the mean porosity of the material of the moon's uppermost cover is ~ 75 percent. These data coincide with the results of determining the porosity of the material of the moon's upper cover from Surveyor 3. It should be pointed out that the direct measurements of ρ_s by Luna 13 coincide with the radar data obtained by the automatic stations in the Luna and Surveyor series, whereas the indirect measurements of ρ_s by Surveyor 3 and Surveyor 7, and the values obtained in the laboratory for lunar soil, are higher by a factor of 1.3 - 1.6 than the ρ_s values found by radar measurements from the automatic stations in the Luna and Surveyor series. The reasons for this discrepancy could be errors in measuring the characteristics of the scattering of radio waves by the lunar surface, the effect of surface averaging during the radar experiments, possible deformation of the soil when making direct density measurements, and a host of other factors.

CHAPTER VI

THE FUTURE OF RADAR INVESTIGATIONS OF THE MOON

Radar methods of investigating planets still are young, but have provided a great deal of information on the properties of the surface layer of planets, and on the atmospheres that surround the planets, since the first radar observations of the moon were made in 1956. This information, along with the data obtained using radioastronomy, optical, and other methods, has enhanced considerably our knowledge of the moon, and of the planets in the solar system. Radar investigations have yielded a particularly great deal of information about the moon. Determined in the course of conducting radar ground investigations and radar experiments from space vehicles, were the characteristics of reradiation, averaged for the lunar disk, and investigations of the characteristics of reradiation from individual lunar regions was begun as well.

Processing the data obtained from radar investigations of the near side of the moon provided some of the physical characteristics of the surface, and of the lunar surface layer, such as the effective permittivity, the density of the material of the upper cover of the moon, and surface depression angles. All these magnitudes were determined for the whole of the lunar disk over quite a broad band of radio waves, from 8 mm to 20 m, so it was possible to estimate the average change in the density of the material of the moon's upper cover with change in depth of the surface layer for the near side of the moon.

Despite the quite broad sweep of information obtained in recent years on the average properties of the upper cover of the near side of the moon, information on the properties of a great many local regions of the lunar surface still is very meager. Yet the landing of automatic and manned stations on the lunar surface, their movement on that surface, and the conduct of a whole series of direct investigations of different regions of the moon, make knowledge of the characteristics of the moon's upper cover, averaged for the lunar disk, and knowledge of the mechanical and electromagnetic properties of the material in quite small local regions of the lunar surface, a necessity.

This makes the task of measuring the electromagnetic properties of the material in local regions of the near side of the moon with a high degree of resolution, and of using these data to compile radar charts of the near side of the moon, one of the primary tasks of the very near future. These measurements can be made by using ground radar and the frequency-time selection method, and the measurements obtained from artificial moon satellites and automatic stations landed on the lunar surface. The goal of these measurements is to study the distribution of permittivity, density, and slopes on the surface of the near side of the moon, as well as to compile charts of the "reflectivity" of different sections of the lunar surface. Polarization radar measurement from the ground, and particularly from circumlunar space, have very good prospects for the future here. /164

It should be pointed out that investigation of the properties of local regions of the moon by the different remote measurement methods does not lose its currency, even after landings have been made on the lunar surface by expeditions that can investigate directly what are very limited regions of the moon. Knowledge of the characteristics of the surface, and of the surface layer, in individual regions of the moon, including regions in which man has landed, obtained by remote measurement methods, and knowledge of these same characteristics obtained by man in regions in which he has landed, once compared, will enable us to correlate the results of the direct and remote measurements, and in this way correct the results of the remote measurements of the properties of the material of the surface layer in regions of the moon not yet investigated by man. (This appears to be the method used by the spacecraft in the Apollo series.)

Methods for making remote measurements of individual regions of the surface, developed in the course of investigating the moon, will be highly important for future research on the planets in the solar system.

The far side of the moon is a blank in our knowledge of the electromagnetic characteristics of the surface layer. Investigation of its properties by radar methods from spacecraft can yield information on its echo characteristics, as well as on the physical characteristics of its surface layer. The result will be additional data for investigating the nature and history of

the moon. These measurements should be conducted over as wide a band of radio waves as possible, so as to obtain data on change in the properties of the material of the upper cover of the far side of the moon with depth.

Radar measurements of the moon from earth in the decameter band have shown that the reflection factor, the permittivity, and the density increase with increase in the wavelength.

Investigation of the properties of the material lying below the plowed upper layer is significant for an understanding of the evolution of the moon, and for studying its internal structure. This task can be performed by making polarization measurements using radioastronomy methods over quite a broad band of wavelengths, as well as by radar measurements made from artificial moon satellites in the meter and decameter bands. Simultaneous measurements on several wavelengths will provide an estimate of the thickness of the plowed layer, and of the change in the thickness of this layer in different regions of the moon. These data will be of great scientific value because they will make it possible to determine such physical characteristics as the permittivity and the density of the material of the basic moon rocks, and this will make possible an assessment of their composition without resorting to the extraction of material from depths of several tens of meters under conditions that, on the moon, are quite complicated. /165

The absence of a significant atmosphere on the moon makes it possible to use waves in the millimeter and submillimeter bands to measure the moon's surface properties, and doing so will provide data on the physical properties of the material of the moon's uppermost cover, that with a thickness of just a few centimeters. It is desirable to make these measurements from artificial moon satellites because they can obtain data for much more extensive areas of the lunar surface than can be obtained by experiments such as these conducted from stations that have been landed on the moon.

It is desirable to make radar and radioastronomy investigations simultaneously when investigating the moon because they complement each other and provide correlated data on the properties of the material of the planet's upper cover. Combined experiments of this type can be performed from the ground,

or from spacecraft in circumlunar space. Experiments conducted from oriented artificial moon satellites can yield particularly interesting results. Rigid orientation of these satellites on the local vertical will make it possible to conduct investigations of the properties of the moon's upper cover with very high surface resolution. But in order to obtain more complete data on the properties of the surface, and of the surface layer, in as many regions of the moon as possible, the radar and radioastronomy measurements with high resolution must be supplemented by stereo pair measurements, and measurements in the infrared with high resolution.

The future building of such artificial moon satellites with adequately long lives will enable us to obtain a great volume of extremely valuable scientific data on the properties of the material of different regions of the moon, and this will make it possible to become more closely acquainted with our natural satellite. /166

The conduct of systematic investigations from artificial moon satellites will serve as an additional source of data for man, even after the beginning of direct investigation of the moon by astronauts, because these latter have limited capabilities and can investigate only a small part of the surface in areas in which manned spacecraft land. It is understood that these investigations cannot possibly study the properties of the lunar material as a whole, or determine the difference in properties in different regions of the lunar surface. Complex investigations, conducted from the ground, from artificial moon satellites with mobile automatic moon stations of the Lunokhod 1 type, and directly by astronauts in different regions of the lunar surface, will provide this capability.

APPENDICES

SELECTED DATA ON SPACECRAFT LAUNCHED INTO CIRCUMLUNAR SPACE AND LANDED ON ITS SURFACE /167

AUTOMATIC MOON STATIONS [35, 85]

Automatic Station	Date of Launch	Landing Site		Landing Region	Notes
		Latitude, °	Longitude, °		
Luna 2	Dec 9, 1959	+30	0	Sinus Lunicus	The first automatic station to reach the surface of the moon.
Ranger 7	Jul 28, 1964	-10.7	-20.7	Mare Cognitum	First close-range photographs of the moon.
Ranger 8	Feb 2, 1965	+2.6	+24.8	Mare Tranquillitatis	
Ranger 9	Mar 21, 1965	-12.9	-2.4	Crater Alphonsus	
Luna 9	Jan 31, 1966	+7.13	-60.37	Sinus Priluneniya (Oceanus Procellarum)	First soft landing on the moon. First panoramic photographs of the lunar surface.
Luna 13	Dec 21, 1966	+18.87	-62.05	Oceanus Procellarum	First direct measurements of lunar soil properties.
Surveyor 1	May 30, 1966	-2.49	-43.32	Oceanus Procellarum	
Surveyor 3	Apr 17, 1967	-3.06	-23.32	Oceanus Procellarum	
Surveyor 5	Sep 8, 1967	+1.42	+23.20	Crater Sabine D (Mare Tranquillitatis)	
Surveyor 6	Nov 7, 1967	+0.46	-1.37	Sinus Medii	
Surveyor 7	Jan 7, 1968	-40.97	-11.44	Crater Tycho region	

ARTIFICIAL MOON SATELLITES AND AUTOMATIC STATIONS FLYING NEAR THE MOON [35] /168

Automatic Station	Date of Launch	Orbital Parameters				Note
		Inclination, °	Height of Apocenter, km	Height of Pericenter, km	Revolution Period, min	
Luna 3	Oct 4, 1959	75 (to the earth's equator)	~ 480,000	~ 40,000	22,3000	First photographs of the far side of the moon. First artificial sun satellite.
Zond 3	Jul 18, 1965					
Luna 10	Mar 31, 1966	71.9	1,017	350	178	First artificial moon satellite.
Luna 11	Aug 24, 1966	27	1,200	160	~ 180	
Luna 12	Oct 22, 1966		1,740	100	205	
Luna 14	Apr 7, 1968	42	870	160	220	
Lunar Orbiter 1	Oct 8, 1966	12.16	1,867	192	217.4	
Lunar Orbiter 2	Nov 6, 1966	11.88	1,849	50	208.4	
Lunar Orbiter 3	Feb 4, 1967	21	~ 1,800	55	209	
Lunar Orbiter 4	May 4, 1967	85	6,110	2,700	720	
Lunar Orbiter 5	Aug 5, 1967	85	6,050	196		
Explorer 35	Jul 19, 1967	169	9,340	2,570	690	
Zond 5	Sep 17, 1968					First instruments to have investigated circumlunar space and been brought back to the earth.
Zond 6	Nov 10, 1968					First photographs of the moon brought back to the earth.

REFERENCES

1. Akimov, L. A., Tsvetkova, V. S., Doklad na Simpoziume po fizike Luny i planet [Report on the Symposium on the Physics of the Moon and Planets]. Kiev. 1968. /169

2. Aleksandrov, Yu. N., Rzhiga, O. N., Astron. zh. 45, No. 3, 616, 1968.

3. Allen, C. W., Astrofizicheskiye velichiny [Astrophysical Magnitudes]. M., IL, 1960.

4. Al'pert, Ya. L., Ginzburg, V. L., Feynberg, Ye. L., Rasprostraneniye radiovoln [Propagation of Radio Waves]. M., Gostekhizdat, 1953.

5. Ambartsumyan, V. A., et al., Kurs astrofiziki i zvezdnoy astronomii [Course in Astrophysics and Celestial Astronomy]. M-L. ONTI, 1936.

6. Antokol'skiy, M. L., Dokl. AN SSSR, 62, 203, 1948.

7. Astronomicheskiy yezhegodnik 1968 g [Astronomical Yearbook 1968]. M., "Nauka" Press, 1967.

8. Atlas obratnoy storony Luny, ch. II [Atlas of the Far Side of the Moon, Part II]. M., "Nauka" Press, 1967.

9. Barabashov, N. P., Publ. Khar'kovskoy observatorii, 1, 35, 1927.

10. Barabashov, N. P., et al., Astron. zh., 36, 496, 1959.

11. Bolduin, R., Chto my znayem o Lune [What We Know About the Moon], M., "Mir"Press, 1967.

12. Bondar', L. N., Zelinskaya, M. R., et al., Izv. vuzov, Radiofizika (in printing).

13. Brand, J., Hodge, P., Astrofizika solnechnoy sistemy [Astrophysics of the Solar System]. M., "Mir" Press, 1967.

14. Brekhovskikh, L. M., Dokl. AN SSSR, 79, 585, 1951.

15. Brekhovskikh, L. M., Dokl. AN SSSR, 81, 1023, 1951.

16. Brekhovskikh, L. M., ZhETF, 1952, 23, No. 3, 275.

17. Vinogradov, A. P., Surkov, Yu. A., et al., Kosmicheskiye issledovaniya, 4, No. 6, 871, 1966.

18. Vinogradov, A. P., Surkov, Yu. A., et al., Kosmicheskiye issledovaniya, 5, No. 6, 874, 1967.

19. Gavrilov, I. V., Astron. zh., 45, No. 2, 399, 1968.

Editor's Note: M = Moscow; M-L = Moscow-Leningrad.

20. Gavrilov, I. V., Doklad na Simpoziume po fizike Luny i planet [Report on the Symposium on the Physics of the Moon and Planets], Kiev, 1968.

21. Getmantsev, G. G., Kalashnikov, N. I., et al., Kosmicheskiye issledovaniya, 3, No. 4, 618, 1965.

22. Gol'nev, V. Ya., Soboleva, N. S., Izv GAO AN SSSR, 23, No. 172, 83, 1964.

23. Gurshteyn, A. A., Priroda, No. 6, 3, 1967.

24. Dolginov, Sh. Sh., et al., Dokl. An SSSR, 170, No. 574, 1967.

25. Dulevich, V. Ye., Korostelev, A. A., et al., Teoreticheskiye osnovy radiolokatsii [Theoretical Principles of Radar]. "Sovetskoye Radio" Press, 1964.

26. Zonnenshtral', G. A., Fel'dman, Yu. I., Kosmicheskiye issledovaniya, 8, No. 4, 588, 1970.

27. Isakovich, M. A., ZhETF, 23, 3, 305, 1952.

28. Catrona, L. I., Hall, G. G., Zarubezhnaya radioelektronika, No. 2, 3, 1962.

29. Katsenbogen, M. S., Kharakteristiki obnaruzheniya [Detection Characteristics]. M., "Sovetskoye radio" Press, 1965.

30. Kislyakov, A. G., Losovskiy, B. Ya., Salomonovich, A. Ye., Izv. vuzov, Radiofizika, 6, 192, 1963.

31. Kobrin, M. M., Radiotekhnika i elektronika, 4, No. 5, 892, 1957.

32. Kozlovskaya, S. V., Byull. In-ta teor. astron, 9, No. 5, (108), 5217, 1964.

33. Kozyrev, N. A., Izv. Krymskoy astrofiz. observatorii, 16, 148, 1956.

34. Kopal, Z., Luna [The Moon]. M., IL, 1963.

35. Kosmonavtika. Malen'kaya entsiklopediya. [Cosmonautics. Small Encyclopedia]. M., "Sov. Entsiklopediya" Press, 1968.

36. Kuiper, G. P., Middlehurst, B. M. (Ed.), Planety i sputniki [Planets and Satellites]. M., IL, 1963.

37. Krotikov, V. D., Izv. vuzov, Radiofizika, 5, No. 6, 1057, 1962.

38. Krotikov, V. D., Troitskiy, V. A., Astron. zh., 39, No. 6, 1089, 1962.

39. Krupenio, N. N., Kosmicheskiye issledovaniya, 5, No. 5, 758, 1967. /170

40. Krupenio, N. N., Izv. komissii po fizike Luny i planet [News of the Commission on the Physics of the Moon and Planets] (in printing).

41. Krupenio, N. N., Kosmicheskiye issledovaniya, 6, No. 2, 252, 1968.

42. Krupenio, N. N., Kosmicheskiye issledovaniya, 6, No. 3, 475, 1968.

43. Krupenio, N. N., Kosmicheskiye issledovaniya, 6, No. 6, 951, 1968.

44. Krupenio, N. N., V sb. Problemy i perspektivy razvitiya apparatury dlya kosmicheskikh issledovaniy [In collection: Problems and Prospects for the Development of Equipment for Space Research]. M., "Nauka" Press (in printing).

45. Krupenio, N. N., Fel'dman, Yu. I., Doklad na 9 Vsesoyuznoy konferentsii po rasprostraneniyu radiovoln [Report to the 9th All-Union Conference on the Propagation of Radio Waves]. Khar'kov, 1969.

46. Kressner, G. N., Mikhaels, D. V., Vvedeniye v sistemy kosmicheskoy svyazi [Introduction to Space Communication Systems]. M., "Svyaz'" Press, 1967.

47. Levin, B. Yu., Ruskol, Ye. L., Voprosy kosmogonii, 8, 109, 1962.

48. Leykin, G. A., Shvidkovskaya, T. Ye., Doklad na Simpoziume po fizike Luny i planet [Report on the Symposium on the Physics of the Moon and Planets]. Kiev, 1968.

49. Losovskiy, B. Ya., Astron. vestnik, 2, No. 3, 129, 1968.

50. Losovskiy, B. Ya., Doklad na V Vsesoyuznoy konferentsii po radioastronomii [Report to the 5th All-Union Conference on Radioastronomy]. Khar'kov, 1965.

51. Luna. Sbornik statey. [The Moon. A Collection of Articles]. Ed. by Markov, A. V. M., Fizmatgiz, 1960.

52. Markov, A. V., Doklad na Simpoziume po fizike Luny i planet [Report on the Symposium on the Physics of the Moon and Planets]. Kiev, 1968.

53. Moroz, V. I., Fizika planet [Physics of the Planets]. M., "Nauka" Press, 1967.

54. Ness, N. F., Doklad na Simpoziume po fizike Luny i planet [Report on the Symposium on the Physics of the Moon and Planets]. Kiev, 1968.

55. Nikonova, Ye. K., Izv. Krymskoy astrofiz. observatorii, 4, 114, 1949.

56. Orlova, N. S., Astron. zh., 33, No. 1, 93, 1956.

57. Polnaya karta Luny [Complete Moon Chart]. M., "Nauka" Press, 1968.

58. Pskovskiy, Yu. P., Priroda, No. 4, 24, 1968.

59. Radioastronomiya. Parizhskiy simpozium 1958 goda. Sbornik pod red. Barsevalla, R. N. [Radioastronomy. Paris Symposium, 1958. Collection edited by Barsevall, R. N.]. M., IL, 1961.

60. Rasprostraneniye ul'trakorotkikh voln, perevod s angliyskogo pod red. Shillerova, B. A. [Propagation of Ultrashort Waves. Translated from English. Editor Shillerov, B. A.]. M., "Sov. Radio" Press, 1954.

61. Rodionova, Zh. F., Volchkova, L. I., Doklad na Simpoziume po fizike Luny i planet [Report on the Symposium on the Physics of the Moon and Planets]. Kiev, 1968.

62. Ruskol, Ye. L., Kosmicheskiye issledovaniya, 3, No. 3, 395, 1965.

63. Rysina, L. R., V sb. Astronomiya 1965 g (Solntse, Luna, planety) [In collection: Astronomy, 1965 (Sun, Moon, and Planets)]. M., VINITI Press, 1967.

64. Semenov, B. I., Izv. vuzov, Radiofizika, 5, No. 6, 1967, 1962.

65. Skolnik, M., Vvedeniye v tekhniku radiolokatsionnykh sistem [Introduction to the Engineering of Radar Systems]. M., "Mir" Press, 1965.

66. Soboleva, N. S., Astron. zh., 39, No. 6, 1124, 1962.

67. Sytinskaya, N. N., Uch. zap. LGU, No. 116, 138, 1950.

68. Sytinskaya, N. N., Sharono, V. V., Uch. zap. LGU, No. 153, 114, 1952.

69. Tikhonova, T. V., Troitskiy, V. S., Doklad na Simpoziume po fizike Luny i planet [Report on the Symposium on the Physics of the Moon and Planets]. Kiev, 1968.

70. Trexler, I., Zarubezhnaya radioelektronika, No. 12, 37, 1958.

71. Troitskiy, V. S., Izv. vuzov, Radiofizika, 10, No. 9-10, 1266, 1967.

72. Troitskiy, V. S., Astron. zh., 31, No. 6, 511, 1954.

73. Troitskiy, V. S., Doklad na Simpoziume po fizike Luny i planet [Report on the Symposium on the Physics of the Moon and Planets]. Kiev, 1968.

74. Turkevich, A. L., Doklad na Simpoziume po fizike Luny i planet [Report on the Symposium on the Physics of the Moon and Planets]. Kiev, 1968.

75. Fedorets, V. A., Publ. Khar'kovskoy obs., 2, 74, 1952.

76. Haymuller, R. S., Zarubezhnaya radioelektronika, No. 2, 8, 1962.

77. Hagfors, T., Doklad na Simpoziume po fizike Luny i planet [Report on the symposium on the Physics of the Moon and Planets]. Kiev, 1968.

78. Cherkasov, I. I., Kemurdzhian, A. L., et al., Kosmicheskiye issledovaniya, 5, No. 5, 746, 1967.

79. Sharonov, V. V., Priroda planet [The Nature of Planets]. M., Fizmatgiz, 1958.

80. Evans, J. V., Zarubezhnaya radioelektronika, No. 12, 25, 1958.

81. Yakovlev, O. I., Yefimov, A. I., Dokl. AN SSSR, 174, No. 3, 583, 1967.

82. Yakovlev, O. I., Yefimov, A. I., Matyugov, S. S., Kosmicheskiye issledovaniya, 6, No. 3, 432, 1968. /171

83. Yakovlev, O. I., Doklad na Simpoziume po fizike Luny i planet [Report on the Symposium on the Physics of the Moon and Planets]. Kiev, 1968.

84. Yakovlev, O. I., Matyugov, S. S., et al., Doklad na 9 Vsesoyuznoy konferentsii po rasprostraneniyu radiovoln [Report to the 9th All-Union Conference on the Propagation of Radio Waves]. Khar'kov, 1969.

85. Yaffe, L. D., Doklad na Simpoziume po fizike Luny i planet [Report on the Symposium on the Physics of the Moon and Planets]. Kiev, 1968.

86. Baars, I. W., et al., URSI Symposium, Japan, Tokyo, 1963.

87. Baars, I. W., et al., Astron. J., 70, N 2, 132, 1965.

88. Barabashew, N. P., Astron. Nachr., 217, 445, 1922.

89. Beckmann, P., Spizzichino, The Scattering of Electromagnetic Waves from Rough Surfaces. London - New York, Pergamon Press - MacMillan, 1963.

90. Beckmann, P., IEEE Trans. on Antennas and Propagation, AP-13, 384, 1965.

91. Beckmann, P., J. Geophys. Res., 70, 2345, 1965.

92. Beckmann, P., Proc. IEEE, 53, N 8, 1012, 1965.

93. Beckmann, P., Klemperer, W. K., Radio Science, 1965, 69D, No. 12, 1669.

94. Beckmann, P., J. Geophys. Res., 73, N 2, 649, 1968.

95. Brown, I. G., Evans, J. V., et al., Proc. Phys. Soc., 69B, N 9, 901, 1956.

96. Brown, W. E., J. Geophys. Res., 65, N 10, 3087, 1960.

97. Brown, W. E., J. Geophys. Res., 72, N 1, 791, 1967.

98. Campbell, M. I., Ulrich, J., Hapke, B. W., Trans. Amer. Geophys. Union, 48, N 1, 152, 1967.

99. Caver, J. H., Norton, B. H., Proc. Astron. Soc. Austral., 1, N 1, 11, 1967.

100. Daniels, F. B., J. Geophys. Res., 68, N 2, 449, 1963.

101. Daniels, F. B., J. Geophys. Res., 68, N 6, 1781, 1963.

102. Daniels, F. B., J. Geophys. Res., 68, N 9, 2864, 1963.

103. Davis, J. R., Rohlfs, D. C., et al., Radio Science, 69D, N 12, 1659, 1965.

104. Davies, R. D., Gardner, E. F., Astron. J. Physic, 19, N 6, 823, 1966.

105. Electronics, 1967, 40, N 2, 47, 1967.

106. Evans, J. V., Proc. Phys. Soc., B70, 1105, 1957.

107. Evans, J. V., Pettengill, G. H., J. Geophys. Res., 68, N 2, 423, 1963.

107a. Evans, J. V., MIT Lincoln Laboratory Technical Report, 272, ASTIA, N DDC 291102.

108. Evans, J. V., Hagfors, T., Icarus, 3, N 2, 151, 1964.

109. Evans, J. V., Radio Science, 69D, N 12, 1646, 1965.

110. Evans, J. V., Hagfors, T., J. Geophys. Res., 71, N 20, 4871, 1966.

111. Fricker, S. I., Ingalls, P. P., et al., J. Res NBS (Radio Prop.) 64D, N 5, 455, 1960.

112. Fung, A. K., J. Geoph. Res., 69, N 6, 1063, 1964.

113. Fung, A. K., Moore, R. K., J. Geophys. Res., 69, N6, 1075, 1964.

114. Fung, A. K., Proc. IEEE, 54, N 7, 2171, 1966.

115. Fung, A. K., Moore, R. K., J. Geophys. Res., 71, N 12, 2939, 1966.

116. Girand, A., Radio Science, 69D, N 12, 1677, 1965.

117. Goldstein, R. M., IEEE Trans. on Antenn. and Prop., AP-12, N 7, 865, 1964.

118. Grant, G. R., Japlee, B. S., Proc. IRE, 45, N 7, 976, 1957.

119. Grieg, D. D., Metzger, S., Waer, R., Proc. IRE, 36, N 5, 562, 1948.

120. Hagfors, T., J. Geophys. Res., 66, N 3, 777, 1961.

121. Hagfors, T., URSI meeting on planetary surfaces and atmospheres. Puerto Rico, Arecibo, 1965.

122. Hagfors, T., J. Geophys. Res., 69, N 18, 3779, 1964.

123. Hagfors, T., J. Geophys. Res., 71, N 2, 379, 1966.

124. Hagfors, T., Radio Science, 2, N 5, 445, 1967.

125. Hapke, B. W., J. Geophys. Res., 68, N 15, 4571, 1963.

126. Hapke, B. W., Astron. J., 71, N 5, 333, 1966.

127. Hapke, B. W., Trans. Amer. Geophys. Union, 47, N 1, 149, 1966.

128. Hargreaves, J. K., Proc. Phys. Soc., B73, 536, 1959.

129. Hayre, H. S., Moore, R. K., Radio Science, 65D, N 5, 427, 1961.

130. Heiles, C. E., Drake, F. D., Icarus, 2, N 4, 281, 1963.

131. Hughes, V. A., Proc. Phys. Soc., 78, N 9, 988, 1961. /172

132. Hughes, V. A., J. Geophys. Res., 67, N 2, 892, 1962.

133. Hughes, V. A., Proc. Phys. Soc., 89, N 10, 1117, 1962.

134. Interavia Air Letter, 6, N 6347, 1967.

135. Jaffe, L. D., Batterson, S. A., et al., J. Geophys. Res, 73, N 12, 3983, 1968.

135a. JPL-NASA Technical Report, 32-1265, 1968.

136. Japlee, B. S., Proc. IRE, 46, N 1, 293, 1957.

137. Karpenter, R. L., Astron. J., 69, N 1, 2, 1964.

138. Kerr, F. I., Shain, S. A., Proc. IRE, 39, N 3, 230, 1951.

139. Klemperer, W. K., J. Geophys. Res., 70, N 15, 3798, 1965.

140. Kroupenio, N. N., 13th Plenary Meeting of COSPAR, Leningrad, May 21-29, 1970.

141. Kuiper, G. P., ed. Photographic Lunar Atlas, Univ. of Chicago Press, 1960.

142. Kuiper, G. P., ed. Nature Lunar Surface, Baltimore, Johns Hopkins Press, 1966.

142a. Leadbrand, R. L., Dyce, R. B., et al., J. Geophys. Res., 65, N 10, 3071, 1960.

142b. Leadbrand, R. L., Dyce, R. B., et al., Pros. IRE, 148, N 5, 932, 1960.

143. Linn, V. L., Sohigian, M. D., Crocker, E. A., MIT. Lincoln Lab. Tech. Rept., 331, ASTIA, Now DDC 426207, 1963.

144. Linn, V. L, Sohigian, M. D., Crocker, E. A., J. Geophys. Res., 69, N 3, 781, 1964.

145. Lunar Astronautical Charts, Aeronautical Chart and Information Center. St. Louis, Mo., 1961-1968.

146. Marcum, J. I., Trans. IRE, IT-6, N 2, 374, 1960.

147. Meyer, Proc. IEEE, 54, N 4, 486, 1966.

148. Mofenson, I., Electronics, 19, N 4, 92, 1946.

149. Moran, I. M., Staelin, D. H., Astron. J., 71, N 8, 865, 1966.

150. Muhleman, D. O., Astron, J., 69, N 1, 34, 1964.

151. Muncey, R. W., Nature, 181, 1459, 1958.

152. Ness, N. F., et al., J. Geophys. Res., 72, N 23, 5074, 1967.

153. Norton, K. A., Omberg, A. C., Proc. IRE, 35, N1, 4, 1947.

154. Pettengill, G. H., Proc. IRE, 48, N 5, 933, 1960.

155. Pettengill, G. H., Henry, J. C., J. Geophys. Res., 67, N 12, 4881, 1962.

156. Pettengill, G. H., Thompson, T. W., Icarus, 8, N 3, 115, 1968.

157. Rea, D. G., Hethering, N., Mifflin, R., J. Geophys. Res., 69, N24, 5217, 1964.

158. Rea, D. G., Hethering, N., Mifflin, R., J. Geophys. Res., 70, N 6, 1565, 1965.

159. Report NASA, Grand No. NGR-33-010-024, 1967.

160. Saari, J. M., Shorthill, R. W., Icarus, 3, N 2, 161, 1964.

160a. Shorthill, R. W., Saari, J. M., Nature, 205, 964, 1965.

161. Shoemaker, E. M., Batterson, S. A., et al., Science, 158, 642, 1967.

162. Sidran, Trans. N. J. Acad. Sci., N 4, 468, 1967.

163. Salomonovich, A. E., Radio Science, 69D, N 12, 1616, 1965.

164. Stewart, A. R., Sci. Rev., 16, N 8, 54, 1966.

165. Sulzer, P. S., Proc. IRE, 1952, 40, N 3, 361.

166. Thompson, T. W., Radio Science, 69D, N 12, 1667, 1965.

167. Thompson, T. W., Dyce, R. B., J. Geophys. Res., 71, 4843, 1966.

168. Troitsky, V. S., Radio Science, 69D, N 12, 1585, 1965.

169. Turkevich, A. L., 11th Plenary Meeting of COSPAR, Tokyo, Japan, 1968.

170. Tyler, G. L., Eshleman, V. R., et al., Science, 157, 193, 1967.

170a. Tyler, G. L., J. Geophys. Res., 73, N 24, 7609, 1968.

171. Urey, H. C., Proc. Roy. Soc., a296, N 1446, 418, 1967.

172. Urey, H. C., New scientist, 36, N 576, 708, 1967.

173. Webb, H. D., Sky and Telescope, 5, N 4, 3, 1946.

Translated for the National Aeronautics and Space Administration under contract No. NASw-2038 by Translation Consultants, Ltd., 944 South Wakefield Street, Arlington, Virginia 22204.

NATIONAL AERONAUTICS AND SPACE ADMINISTRATION
WASHINGTON, D.C. 20546

OFFICIAL BUSINESS
PENALTY FOR PRIVATE USE $300

FIRST CLASS MAIL

POSTAGE AND FEES PAID
NATIONAL AERONAUTICS AND
SPACE ADMINISTRATION
451

U.S.MAIL

POSTMASTER: If Undeliverable (Section 158 Postal Manual) *Do Not Return*

"The aeronautical and space activities of the United States shall be conducted so as to contribute . . . to the expansion of human knowledge of phenomena in the atmosphere and space. The Administration shall provide for the widest practicable and appropriate dissemination of information concerning its activities and the results thereof."

—NATIONAL AERONAUTICS AND SPACE ACT OF 1958

NASA SCIENTIFIC AND TECHNICAL PUBLICATIONS

TECHNICAL REPORTS: Scientific and technical information considered important, complete, and a lasting contribution to existing knowledge.

TECHNICAL NOTES: Information less broad in scope but nevertheless of importance as a contribution to existing knowledge.

TECHNICAL MEMORANDUMS: Information receiving limited distribution because of preliminary data, security classification, or other reasons. Also includes conference proceedings with either limited or unlimited distribution.

CONTRACTOR REPORTS: Scientific and technical information generated under a NASA contract or grant and considered an important contribution to existing knowledge.

TECHNICAL TRANSLATIONS: Information published in a foreign language considered to merit NASA distribution in English.

SPECIAL PUBLICATIONS: Information derived from or of value to NASA activities. Publications include final reports of major projects, monographs, data compilations, handbooks, sourcebooks, and special bibliographies.

TECHNOLOGY UTILIZATION PUBLICATIONS: Information on technology used by NASA that may be of particular interest in commercial and other non-aerospace applications. Publications include Tech Briefs, Technology Utilization Reports and Technology Surveys.

Details on the availability of these publications may be obtained from:

SCIENTIFIC AND TECHNICAL INFORMATION OFFICE

NATIONAL AERONAUTICS AND SPACE ADMINISTRATION

Washington, D.C. 20546